Mechanical design and manufacturing of an insect-scale flapping-wing robot

Mechanical design and manufacturing of an insect-scale flapping-wing robot

A dissertation presented

by

Kevin Yuan Ma

to

The School of Engineering and Applied Sciences

in partial fulfillment of the requirements

for the degree of

Doctor of Philosophy

in the subject of

Engineering Sciences

Harvard University

Cambridge, Massachusetts

June 2015

Thesis advisor

Robert J. Wood

Author

Kevin Yuan Ma

Mechanical design and manufacturing of an insect-scale flapping-wing robot

Abstract

Despite the prevalence of insect flight as a form of locomotion in nature, manmade aerial systems have yet to match the aerial prowess of flying insects. Within a tiny body volume, flying insects embody the capabilities to flap seemingly insubstantial wings at very high frequencies and sustain beyond their own body weight in flight. A precise authority over their wing motions enables them to respond to obstacles and threats in flight with unrivaled speed and grace.

Motivated by a desire for comparably agile flying machines, research efforts in the last decade have generated crucial developments for realizing an artificial instantiation of insect flight. The need for tiny, high-efficiency mechanical components has produced unconventional solutions for propulsion, actuation, and manufacturing. Early vehicle designs proved to be flightworthy but were critically limited by the inability to produce control torques in flight. In this thesis, we synthesize all existing technologies for insect-scale manufacturing and actuation, and we introduce a new vehicle design, the "dual actuator bee," to address the need for flight control. Our work culminates in the first demonstration of controlled, hovering flight of an insect-scale, flapping-wing robot.

As the ultimate goal for this research effort is the creation of fully autonomous flying robots, these vehicles must sustain their own power sources and intelligence. To that end, we explore the challenges of scaling flapping-wing flight to attain greater lift forces. Using a scaling heuristic to determine key vehicle specifications, we develop and successfully demonstrate a hover-capable vehicle design that possesses the

requisite payload capacity for the full suite of components required for control autonomy. With this operational vehicle as a point of reference, we introduce an iterative sizing procedure for specifying a vehicle design with payload capacity capable of supporting power autonomy. In the development of these vehicles, the reliability of their construction has been a substantial challenge. We present strategies for systematically addressing issues of vehicle construction. Together, this suite of results demonstrates the feasibility of achieving artificial, insect-like flight.

Contents

Acknowledgments

First, I would like to thank Prof. Robert Wood for providing me with the inspiration, opportunity, resources, mentorship, and freedom to pursue this captivating project. I cannot think of a better way to have spent my early 20's than building robotic insects. Thank you for giving me the chance to prove myself.

I would also like to thank Prof. Ronald Fearing of UC Berkeley for believing in my potential so early in my career.

I thank the incredibly diverse and talented members and alumni of the Harvard Microrobotics Lab for their help, support, and friendship. Thanks for making it such a wonderful place to work/play. I thank the members of the Robobees Team for their camaraderie and support when I needed it the most. In particular, I must give a special thanks to Pakpong Chirarattananon for his exceptional work on flight control for the robotic bee. We would not have had such compelling results without his efforts. It was a privilege to have him as a colleague and friend.

I thank my parents and sister for their love and support throughout the years and for defining my sense of home. Finally, I thank my girlfriend Lina for her immeasurable contribution to my happiness during my last years in graduate school.

Chapter 1

Introduction

This work describes the suite of design and manufacturing innovations that led to the first successful controlled flight demonstrations of a new micro air vehicle (MAV). The vehicle was developed at Harvard University under the umbrella of the Robobees project, a multidisciplinary collaboration of engineers, computer scientists, and biologists to develop a coordinated swarm of robotic bees, called "Robobees." These Robobees would mimic the scale and aerial aptitude of real honeybees and are envisioned to cooperate as swarms in executing complex tasks. Potential applications include rapidly distributed environment sensing, search-and-rescue applications in hazardous environments, and crop pollination for agriculture.

The key element of the Robobee as a concept is a highly miniaturized, maneuverable, and autonomous MAV that can approach the robust, versatile behaviors of real flying insects. Conceptually, the MAV should capably fly, hover in place, and maneuver. At the macroscale, fixed wing aircraft and rotorcraft (helicopters) have well-understood aerodynamic and design principles. However, these air vehicle morphologies cannot be directly miniaturized to the scale of insects without detrimenting performance, stability, or practicality. At the scale of a few centimeters, aerodynamics enter a laminar flow regime where the fluid viscosity becomes much more significant (Reynolds numbers on the order of 1000) and invisid airflow assumptions that govern

much of macroscale air vehicle design principles do not apply. This motivates the search for other methods of powering flight.

Flying insects are neither strictly fixed-wing nor rotary-wing aircrafts. They instead use rapidly reciprocating airfoils (flapping wings) with high accelerations to generate lift. As the flow structures created by this form of flight are at best periodic and generally chaotic, steady airflow aerodynamic assumptions no longer apply and unsteady aerodynamic analyses must be introduced. This greatly complicates the aerodynamic theory of flapping wing flight. In the last half century, researchers have gradually resolved the aeromechanics of insect flapping-wing flight through a combination of *in vivo* and *in situ* experiments. A growing body of work is approaching a comprehensive understanding of flapping-wing flight mechanics and the unsteady aerodynamics that govern it [4, 15, 29, 38, 43]. A compelling test of this understanding is to apply it to the development of an artificial flapping-wing micro air vehicle (FWMAV) that can approach the performance of biological flyers.

1.1 Insect-scale flapping wing flight in brief

Flapping wing flight involves the complex, coordinated motions of wings. For the work presented in this dissertation, we focus on a two-winged flapping-wing system. This mimics the morphology of flies. Bees, which the Robobee vehicle is explicitly modeled on, have four wings but the fore and hind wings are mechanically coupled to operate similarly to two wings [18]. Each wing undergoes rotation about all three degrees of rotational freedom [57]. The main mode of rotation is wing flapping, which rotates the wing about its root along a nominally fixed stroke plane. It consists of nominally symmetric upstroke and downstroke motions. The wing also undergoes wing pitching, or rotation, about the major axis of the wing. This wing pitching oscillates about a mean pitch angle, out of phase with the flapping motion. The third

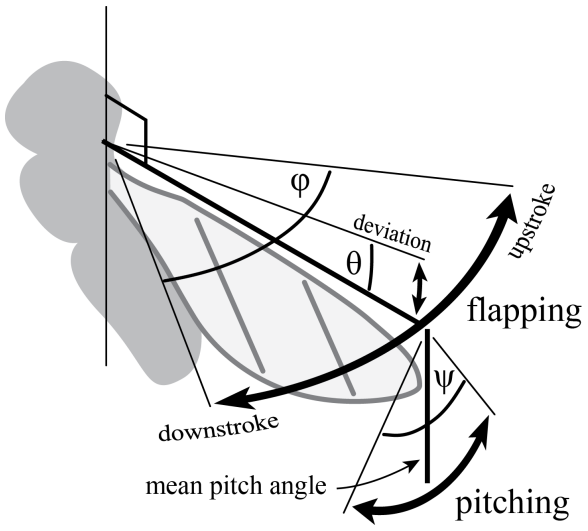

Figure 1.1: The three modes of rotation in flapping wing flight are labeled flapping, pitching, and stroke plane deviation. The flapping mode rotates the wing at its root about a vertical axis and is labeled by ϕ. It consists of an upstroke and downstroke, relative to the direction of nominal motion. The pitching mode rotates the wing about its spanwise axis, oscillating around a mean pitch angle, and is designated ψ. The deviation mode rotates the wing out of its stroke plane, or plane of flapping, and is designated θ.

mode of rotation is stroke plane deviation and consists of small motions of the wing tip that occur out of plane with the stroke plane. These wing rotation modes are illustrated in Figure 1.1. The wings are also compliant airfoils that twist and camber as they move; this has significant effects on the aerodynamics [23]. Together, these wing motions enables the wings alone to generate propulsive thrust forces and the full gamut of control torques for flight maneuvers.

The aerodynamics of flapping wing flight are unsteady and time dependent, and forces generated by a wing trajectory depend on the conditions of the previous cycle's trajectory. Inherent to their system dynamics because of their small scale, flapping wing flying animals and vehicles are dynamically unstable and require active control to remain stable in flight [44]. To generate control torques for stabilizing flight, flapping wing flyers can tweak their nominal wing trajectories on a per-cycle basis. Because

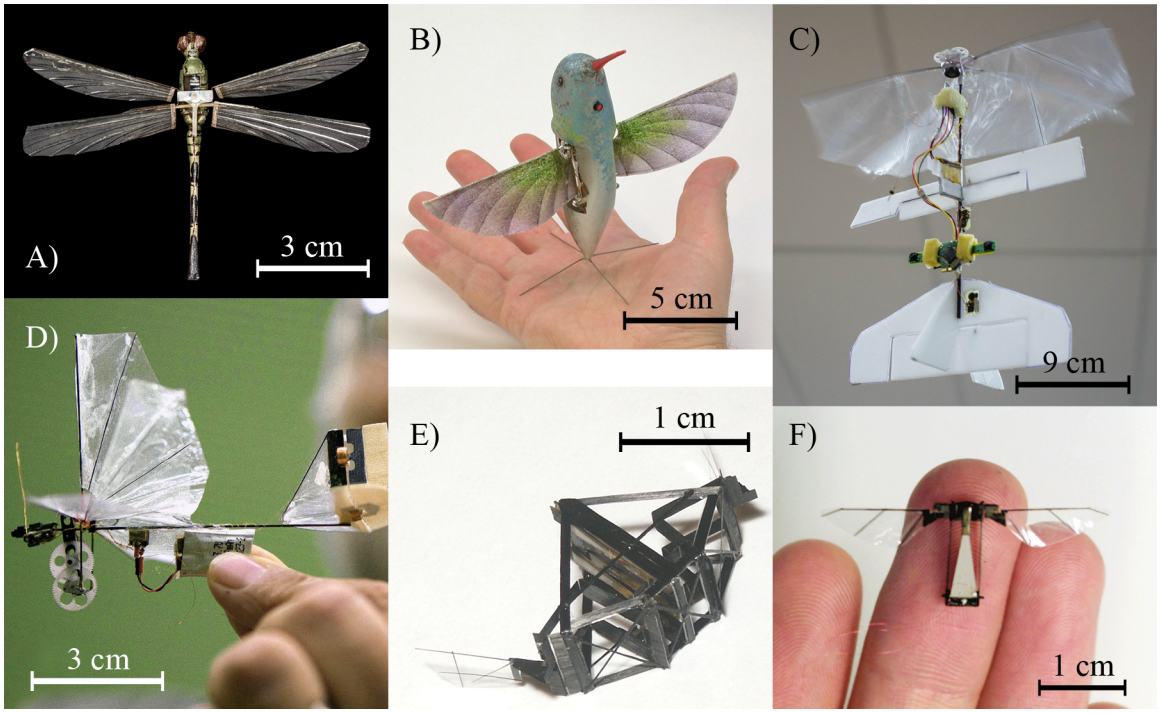

Figure 1.2: Examples of previous FWMAV efforts. A) The CIA Insectothopter [8]. B) Aeronvironment's Nanohummingbird [37]. C) DelFly II [13]. D) DelFly Micro [12]. E) UC Berkeley Micromechanical Flying Insect [25]. F) Harvard Microrobotic Fly [61].

of high flapping frequencies (upwards of 150Hz for bees and flies), small changes in wing trajectories can quickly accumulate to produce body moments [28]. The flight mechanics of flapping wing flight are further elaborated in Section 1.3. Flying insects drive their wing flapping motion with large power muscles in the thorax while smaller control muscles modulate deformations to the wing trajectory [18].

1.2 Prior work

Flapping-wing micro air vehicles at the scale of small birds and flying insects have been in development for at least a half century. One of the earliest examples is the CIA Insectothopter from the 1970's which was modeled after a dragonfly and powered

by gasoline [8]. This device reportedly had a wingspan of 9 cm, mass of 1 g, and a flight time of 60 seconds. However, it was severely limited by underdeveloped flight control and was never applied in the field. More recent FWMAVs at a similar scale include the Aeronvironment NanoHummingbird and Delft University's Delfly, both of which have well-developed mechanical systems and fully integrated power and control systems. The Nanohummingbird has a 16.5 cm wingspan and weighs 19 g [37]. The Delfly II has a 28 cm wingspan and weighs 16 g [13]. These examples are notable because they were able to achieve stable hovering behavior, which is considerably more difficult due to the lack of far stream velocity to augment lift generation. At the scale of small birds, these robotic vehicles have sufficient payload capacity to carry consumer-grade RC components and control electronics. A smaller Delfly micro was also developed that has a 10 cm wingspan and weigh 3 g but could not hover [12].

In published literature on FWMAVs, few attempts have been made to construct a vehicle with wingspan less than 10 cm to more closely approach the insect-scale. The UC Berkeley Micromechanical Flying Insect (MFI) project first endeavored to create an insect-scale FWMAV [25]. With a wingspan of 2.5 cm, the MFI had scale and performance requirements that could not be met with commercially-available, off-the-shelf components. The project would eventually contribute to the development of new actuation and fabrication technologies that are still in use with current FWMAVs.

1.2.1 Fabrication innovations

The fabrication of insect-scale machines is a significant obstacle facing their development. The mechanical components require feature sizes between micrometers and centimeters—too large for silicon-based microelectromechanical systems (MEMS) and too small for conventional machining and assembly methods. Decreased feature size brings an increased dominance of surface forces, causing revolute joints or sliding

surfaces to become inefficient or infeasible [53, 59]. Additionally, MEMS techniques, although sufficiently precise, are time-consuming, constrain material choice, and limit attainable geometries.

The Berkeley MFI project encountered these fabrication challenges which motivated the development of a new design and fabrication methodology for these small-scale, dynamic machines, called Smart Composite Microstructures (SCM), to address this void in mesoscale manufacturing [59] ("mesoscale" refers to the scale regime between micrometers and centimeters). In SCM, different material layers are precision micromachined, aligned, and laminated together in a monolithic, planar fashion. In these multi-material laminate composites, flexible material can be exposed through the rigid material layers to form flexure hinges in the planar structure. These planar-fabricated flexure hinge mechanisms are manually assembled via folding to create complex, dynamic 3D structures and mechanisms.

This planar design and manufacturing methodology was further refined into the PC-MEMS process, which allowed for unprecedented design complexity and functionality in planar-fabricated structures [50]. A library of materials has been established that are compatible with the PC-MEMS process, including a range of carbon fiber composites, glass fiber composites, metals, ceramics, adhesive films, and polymer films. These manufacturing innovations have been crucial to the development of new FWMAVs, including the ones presented in this work.

1.2.2 The Harvard Microrobotic Fly

The work described in this dissertation is an immediate successor to the work on the Harvard Microrobotic Fly (HMF)—a 3 cm wingspan, 60 mg FWMAV [61]—which itself was a successor to the UC Berkeley Microrobotic Flying Insect (MFI). The MFI project created a 25 mm wingspan and 100 mg MAV that was able to generate complex

flapping wing kinematics with a fully actuated wing drive system [3]. However, a demonstration of lift off was never achieved. The MFI project pioneered a crucial suite of innovations for creating insect-scale FWMAVs, and leveraging those innovations, the HMF demonstrated that manmade flight at the scale of insects is possible.

Among the innovations common to the MFI and HMF were piezoelectric ceramic bimorph actuators [60]. Considerations on the energy density of various actuation technologies eventually reduced the design space to induced-strain materials like piezoelectric ceramic. Conventional electromagnetic motors, common to other small-scale robotic devices, are inefficient at the mesoscale. As scale decreases, surface area-to-volume ratio increases and rotating mechanisms experience greater friction losses. With finite coil wire diameters, tiny electromagnetic motors approach the limits of current density. Additionally, the required manufacturing tolerances for small rotation joints become difficult to achieve. Developed specifically for mesoscale FWMAVs, the bimorph actuators featured a novel design to improve energy density over similar commercially off-the-shelf (COTS) actuators [60].

Leveraging these actuators and the fabrication techniques introduced in Section 1.2.1, the two-winged HMF was able to generate sufficient thrust to offset its own weight, while constrained to vertical guide wires. Key mechanical design features included coupling the two wing drives to a single actuator and utilizing passive rotation wing hinges to modulate wing pitching dynamics. These features greatly simplified the vehicle design relative to the MFI, which had four actuators driving two wings, and reduced vehicle mass substantially. The HMF had to sacrifice controllability with one actuator driving two wings symmetrically, and this resulted in a vehicle incapable of modulating body torques in flight. A mechanical redesign is necessary to attain this ability.

1.3 The need for controllability

The lack of controllability of the HMF motivates the investigation of a design that incorporates flight control mechanisms. Flight control in insect flight is an extremely rich topic, owing much to the fact that flying insects have the musculature for adjusting their wing motions on a cycle-by-cycle basis and rapid motor-sensory control loops for active regulation of flight forces [18]. As with any air vehicle, a flying insect's flight mechanics can be described by three rotation axes defined relative to the body frame: roll, pitch, and yaw. A variety of wing motions have been observed [4, 28, 43] for flight control, but the complete map of wing motions to generated body torques have not yet been fully characterized. Flying insects use their flapping wings as both thrust generators and control surfaces.

Various FWMAVs have achieved body torque modulation, restricted to only the use of two flapping wings and no additional control surfaces. The Aeronvironment Nanohummingbird uses a combination of wing compliance modulation and wing pitching modulation and is able to generate torques about all three body axes in a decoupled manner [37]. In a parallel development to the mechanical design presented in this work, Finio developed a modified design of the HMF which added two additional actuators into the structure of the wing drive to modulate the wing transmission ratio [27]. The design proved to be capable of controlled flight but exhibited significant torque coupling. Ultimately it was too cumbersome to construct and sustain as a FWMAV platform for further study. Another modified design of the HMF added two additional actuators and additional mechanisms to enable indirect wing pitching modulation. This design demonstrated body torque generation but could not be constructed reliably enough to demonstrate controlled flight [52]. The work presented here is a parallel development to these designs that also integrated controllability into a similarly sized FWMAV.

1.4 The need for manufacturability

It becomes clear that designing a FWMAV with torque generation capability requires additional mechanical complexity. This complexity must be supported by a sufficiently capable fabrication process; otherwise, the complexity hinders easy, repeatable construction and reliable performance. The SCM fabrication process proved to be capable of constructing a flightworthy FWMAV in the HMF. The HMF design was simple enough to produce with SCM, but the need for a controllable MAV motivated more complex mechanical design. The PC-MEMS methodology was a direct response to this need for greater fabrication precision and efficiency. But as will be discussed in Chapter 5, trade-offs currently exist with the still-maturing fabrication process. A conventional approach to fabrication and assembly, with the manual assembly of discrete components, still plays a role in the construction of our FWMAVs.

Ideally, the vehicles would be constructed efficiently and reliably, have identical performance, and essentially be interchangeable. But as long as manual assembly is required, assembly errors can compromise these goals. Systematic analysis of the vehicle assembly can drastically reduce the variability in vehicle construction and bring FWMAV designs closer to the reliability required for a sustainable research platform.

1.5 The need for scalability

For these insect-scale FWMAVs to be autonomous, they must have the necessary payload capacity to carry the electronics, sensors, and power source for control and power autonomy. These components are in active, parallel development under the Robobees project umbrella, as most COTS components cannot meet the demanding weight and power specifications of an insect scale FWMAV [31, 62, 35, 19]. The HMF

could lift twice its own mass, but estimates of the payload package are three times its payload capacity.

Studies on the scaling laws for FWMAVs remain preliminary; the bottleneck is mainly due to the lack of a comprehensive model for the flapping-wing aerodynamics and the limited number of working FWMAV prototypes as reference points. In comparison, the aeronautics industry benefits from a century of experience with working designs. In parallel with the developments on fabrication, actuation, and design feasibility, previous vehicle scaling studies have used well-considered approximations for the vehicle model [20, 58, 36]. The present work combines the latest modeling developments with known reference points from working FWMAV prototypes to provide new insights into vehicle scaling for insect-scale FWMAVs.

1.6 Thesis contributions

This dissertation seeks to make Robobees a practical reality for supporting immediate research efforts towards a fully autonomous insect-scale FWMAV and presents convincing evidence for the feasibility of flying insect robots. It brings together the latest developments in manufacturing for every mechanical component in the Robobee. It also compiles the latest developments in system modeling to prescribe a vehicle design that is sized to support wireless, autonomous operation. The contributions are as follows:

1. The practical instantiation of a vehicle design that is inherently controllable.

2. The practical instantiation of a vehicle design that is inherently manufacturable and reproducible.

3. A vehicle sizing procedure to achieve a relevant range of payload capacities.

4. Refined fabrication and assembly processes for repeatable manufacturing of high-precision, flexure-based machines at the scale of microns to millimeters.

Chapter 2

The dual actuator bee design

As a culmination of nearly a decade of developments, including innovations in custom actuators and micromanufacturing technologies, researchers were able to construct the Harvard Microrobotic Fly (HMF)—a 60 mg insect-scale vehicle that uses two flapping wings as its means to generate lift force [61]. However, due to the limitations of the manufacturing technology at that time, the device only featured a single actuator driving the flapping motion of two wings and was unable to generate body torques for aerial steering. Altitude control experiments were performed on the vehicle by constraining its motion to a single, vertical degree of freedom via guide wires [45]. These previous studies proved the feasibility of insect-scale FWMAVs; however, the lack of controlled body moments motivated the need for new designs.

Biologists have studied the free flight maneuvers of fruit flies in great detail and have observed a variety of wing kinematics correlated with aerial turning behavior. Studies have observed turns produced mainly by changes in wing stroke amplitude and adjustments of the stroke plane [28, 29]. Other studies have proposed wing pitch angle modulation as a key method for fruit flies to induce sharp turns [4]. At present, the relationships between wing kinematics and control forces and moments are not fully understood. However, there appears to be a rich variety of possible wing kinematics, even to generate torques about a single body axis, such as yaw [16]. This

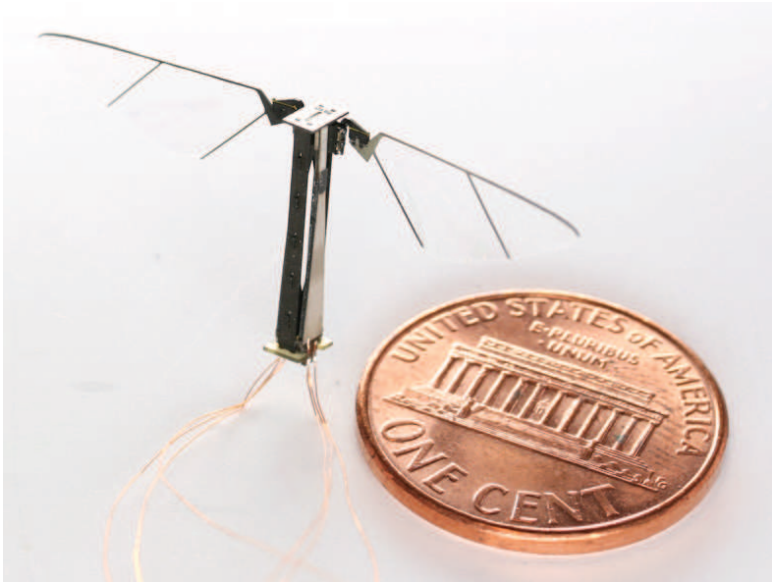

Figure 2.1: The dual actuator bee FWMAV design next to a US penny for scale. Landing gear struts are not attached.

flexibility may be advantageous for engineers designing a maneuverable vehicle.

From the perspective of vehicle engineering, each flapping wing can be viewed as a thrust force source with a thrust vector nominally pointing downward. With two wings on a FWMAV, differential adjustments between these two thrust vectors can induce body torques. Differential modulation can be accomplished in a number of ways. In an early attempt at a controllable vehicle design, the HMF design was augmented with control actuators—a smaller actuator integrated into each wing drive that can modulate the mechanical amplification ratio and thus the stroke amplitude [27]. This design configuration, with three actuators total—two control and one power—was inspired by the thoracic mechanics in insects of the order Diptera, which separate power and control muscles [18]. Controlled flight was demonstrated, though the vehicle design was difficult to construct and was not refined into a practical vehicle

platform for further testing.

Demonstrating a different method of differential thrust modulation, the vehicle design presented in this dissertation uses two power actuators with each actuator independently driving a single wing, illustrated in figures 2.1 and 2.2. The actuation scheme and control strategy exhibited in this "dual actuator bee" design has been explored theoretically by Doman et al. [17] (as well as demonstrated by Hines et al. for a larger scale flapper [33]). Doman demonstrated in simulation that two actuators could generate the required body torques and forces to provide sufficient control authority for six degree-of-freedom control—theoretically, the vehicle can be fully actuated. This two-actuator control scheme was designated the split-cycle, constant-period frequency modulation technique. The dual actuator bee design presented here is essentially the physical instantiation of that control scheme.

This chapter describes the design and fabrication of the dual actuator bee and provides basic models to predict the force and torque capabilities of the vehicle with this actuation scheme. The successful construction of this device was enabled by an early instantiation of the PC-MEMS laminate composite fabrication process [56, 50]. Experiments are conducted to measure the body forces and torques that can be generated by the vehicle for a variety of control input signals. It is shown that the dual actuator bee is capable of generating all three body torques and thrust in excess of body mass.

In addition, the dual actuator bee was integrated with an offboard flight controller setup and has demonstrated tethered but unconstrained stable hovering and basic controlled flight maneuvers. The result validates a sufficient suite of innovations for achieving artificial, insect-like flight.

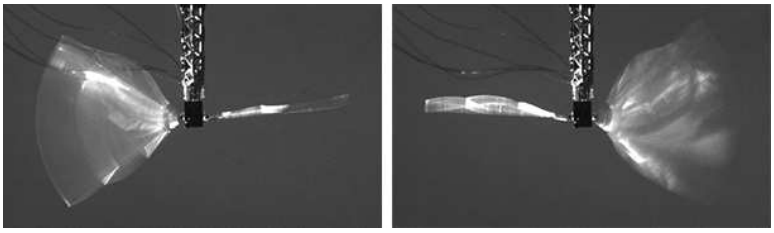

Figure 2.2: The two wings of the vehicle can be controlled independently. In the left image, only the left wing is actuated. In the right image, only the right wing is actuated.

2.1 Design

The original HMF design serves as a design basis for the dual actuator bee. It demonstrated that a vehicle with the specific combination of wings, actuators, mass, operating frequency, and transmission ratio, along with the construction methods and materials used, could generate sufficient thrust force to lift off. Both the HMF and the dual actuator bee use similar manufacturing technology for their mechanical components. The transmission mechanism is constructed from kinematic chains of rigid links and flexure joints as detailed in Chapter 5. The actuators are piezoelectric ceramic bimorph actuators. A relevant detail for the following discussion is that the actuators are oscillating, bending cantilever beams with output taken at the distal end.

The dual actuator bee design takes the HMF design and conceptually splits the vehicle in half—the actuator is split into two separate actuators of equal base width and the two wings are decoupled and independently driven by each actuator. The geometry of each dual actuator is such that the base width is half that of the HMF actuator (3.5 mm to 1.75 mm), but the actuator is optimized for energy density as detailed in [60] and retains an isosceles trapezoidal shape. Based on geometry of piezoelectric ceramic material alone, the total mass of the two, dual actuators is estimated to be 22% more than the single HMF actuator.

The single HMF actuator had sufficient power density to drive the load of two wings with appropriate wing trajectory and thrust generated. The design basis of the dual actuator design is that half of that single actuator should exhibit half of the force output to drive the load of a single wing, allowing a two-winged vehicle to achieve the same system performance. Approximating the flapping wing drives as linear, second-order systems, halving the actuator would result in halving the system stiffness k. A single wing would have half the inertia and damping of two wings. Transmission dynamic effects are assumed to be negligible. Resonant frequency is calculated as $\omega_n = \sqrt{k/m}$. Consequently, the resonant frequency of a single dual actuator wing drive should be similar to the two-wing drive. Assuming the mass of the other vehicle components can be made similar or less, the dual actuator bee should be able to attain a similar lift-to-weight ratio as the original HMF and have control authority over in-flight degrees of freedom.

The primary mechanical design challenge for the dual actuator bee is to robustly support two, kinematically decoupled wing drive mechanisms with an airframe that is stiff and low mass. A key design choice involved the orientation of the actuators with respect to the motion of the wings. The straightforward choice would be to place the two actuators side by side with actuator tip motion in the dorsalventral direction, similar to the HMF. Instead, we took the opportunity to capitalize on the symmetry of the vehicle and cancel out the effect of each actuator's oscillating inertia by orienting the actuators to face each other, shown in figure 2.3. The actuators' tip trajectories are now in the lateral direction. If the actuators are oscillating in phase and with similar amplitude, the body torques due to their inertia should cancel out, assuming the actuators are well-grounded to the same rigid member. Oscillating actuator inertia has never been formally noted as a nuisance in these vehicles, but such body oscillations have the potential to decrease the effective wing stroke amplitude.

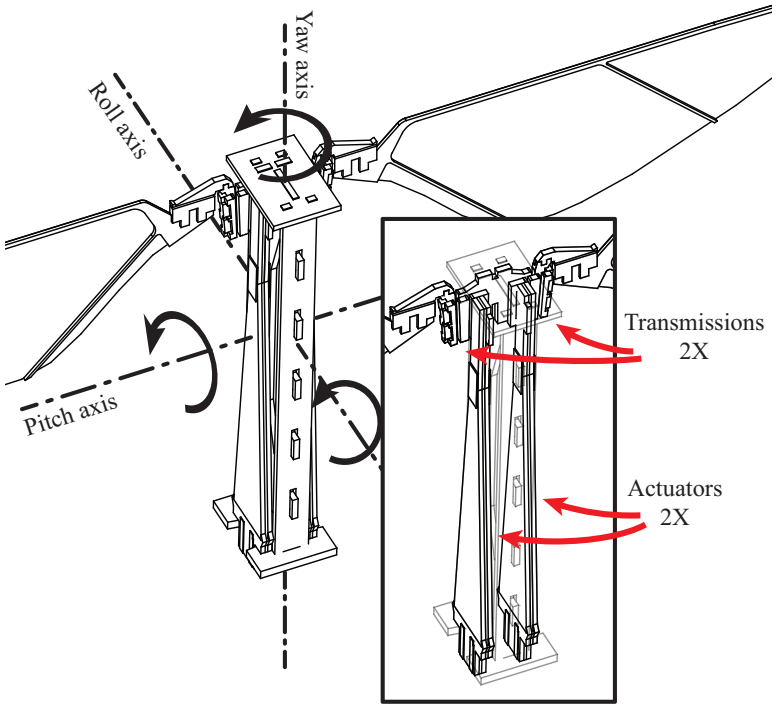

Figure 2.3: Convention used to define the three body rotation axes. The insert highlights the use of two actuators and two wing drives in the vehicle.

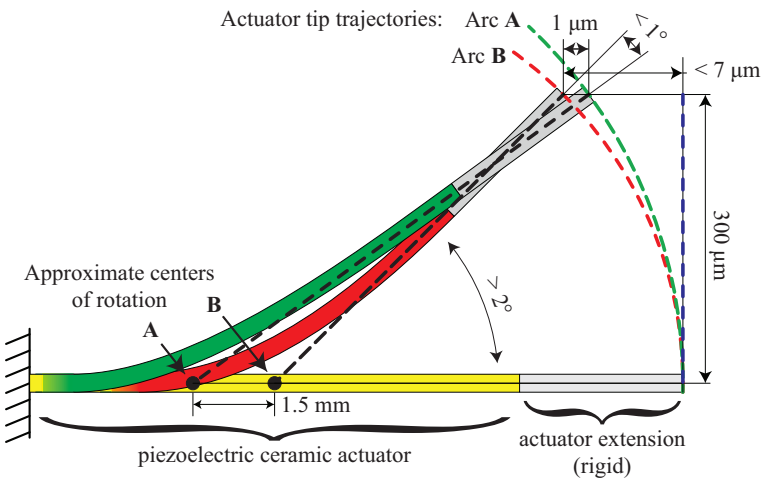

Figure 2.4: Piezoelectric ceramic actuator bending profile indicating tip displacements and angles. The actuators can be approximated as a rotary motion source with a fixed center of rotation. A mismatch between the expected and actual (best approximation) center of rotation up to 1.5 mm has a negligible effect (maximum 1 µm tip offset, $<$ 1 μm angular offset). (Beam deflection not to scale).

This configuration of actuators mitigates that possibility.

Another key insight in the mechanism design is to remove the slider crank from the transmission, reducing vehicle mass and volume. In the HMF, the slider crank converts the nominally rotary motion of the bimorph bending actuators to the linear motion that drives the planar four-bars of the transmission. That design was fixated on the actuator tip displacement, which is to first-order a purely prismatic motion, for small bending deflections. Rotary displacement is a second-order effect, as is the axial displacement of the tip. The actuator of the HMF exhibits a 600 μm peak-to-peak tip displacement. Large deflection beam bending theory predicts a 7μm axial displacement at the extremes of the tip trajectory.

In the dual actuator bee design, we do not fixate on the tip of the actuator but instead consider the actuator bending profile as a whole. Here, it is more appropriate to approximate the actuator as a purely rotary displacement source with a fixed center of rotation. We empirically determined that the approximate center of rotation of the

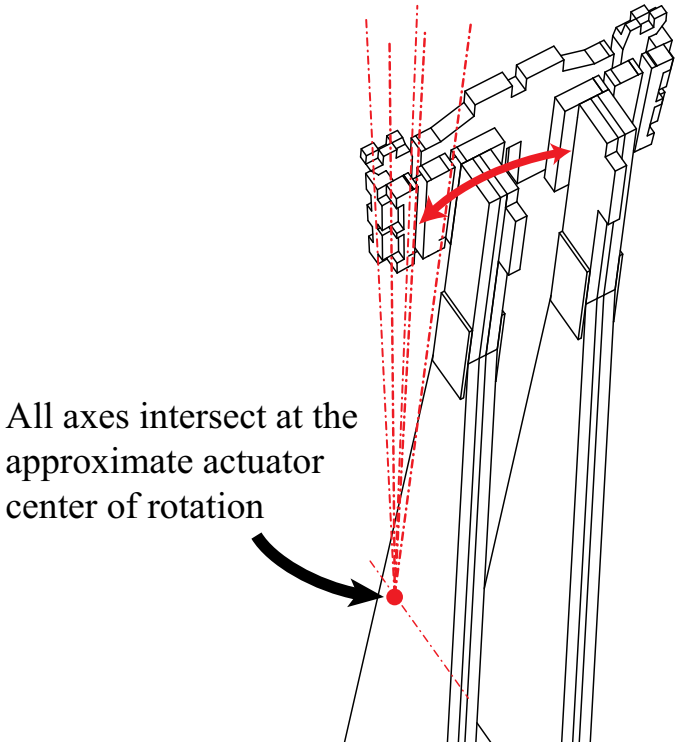

Figure 2.5: Spherical four-bar illustration. All transmission joint rotation axes intersect at an approximate, fixed center of rotation of the actuator. One four-bar for each actuator.

actuator output is 8 mm from the tip, with a variation of 1.5 mm between actuators. The precision of these measurements is not a major concern. Even if the mismatch between the expected and the actual center of rotation was 1.5mm at the extreme, the axial divergence of the actuator tip from the pure circular arc is on the order of 1 μm at maximum tip deflection, as illustrated in figure 2.4. This axial displacement can be tolerated and absorbed by the off-axis compliance of the flexure joints in the transmission.

Using the actuator as a rotary displacement source, we designed a transmission mechanism that consists of a spherical four-bar, with all joint rotation axes intersecting at a single point to coincide with the approximate center of rotation of the actuator, illustrated in figure 2.5. The transmission ratio is designed to match the

value in the original HMF. The actuator mates with the transmission along the edge of the last 3 mm of its length.

It is important to consider the requirements for energy efficiency when operating the vehicle; as highlighted in [61], operating at the resonant frequency of the system will enable maximum power efficiency. In the case of the dual actuator bee, there are two, potentially different resonant frequencies—one for each wing drive. It is in our best interest to have the two resonant frequencies coincide, both for energy efficiency and symmetry of mechanical operation. This can be affected by fabrication reliability.

2.2 Fabrication

Only with recent developments in the fabrication and assembly methods has this vehicle design been rendered practical to construct. Advances in composite laminate mechanical design and fabrication have given us confidence in reliably producing mechanical components. The actuator fabrication process has developed extensively since the HMF, and we can now produce actuators with more consistent performance. However, fabrication inconsistencies are easily introduced in the manual assembly of the components. Fabrication and assembly of mesoscale machines is presented in greater detail in Chapter 5. Here, we present our early attempts at achieving consistent fabrication results.

The dual actuator bee design is particularly sensitive to the symmetry of the two halves of the vehicle; small asymmetries can significantly affect basic operation. Once the mechanism has been assembled, the parameters of the input control signals are modulated to achieve perfectly symmetric operation and reliably flight behavior. However, those parameters can only be tuned to a certain extent established by the initial fabrication precision. Additionally, the control signals cannot influence the

natural frequency of the system; fabrication quality dictates the mechanical properties of the vehicle. It is therefore imperative to have both halves of the dual actuator bee fabricated precisely and symmetrically.

The fabrication of the transmission linkage benefits from an assembly scaffold—a concept introduced in the PC-MEMS process [50]. The essential idea is that auxiliary, sacrificial mechanisms can be fabricated simultaneously around the intended mechanism for the sole purpose of removing degrees of freedom and assisting in precision assembly. In a demonstration of the process's potential, an entire FWMAV vehicle was assembled by activation of a single degree of freedom. This assembly approach is elegant but time consuming to design. The dual actuator bee takes a hybrid approach by using assembly scaffolds to assist in folding up the transmission mechanism only and relegating the other fabrication steps to manual manipulation and assembly. Other techniques employed in the precision fabrication of the mechanical components include extensive use of tabs and slots for mechanical alignment and custom alignment fixtures for assembly accuracy, seen in figure 2.6.

The production of the piezoelectric ceramic bimorph actuators is now much more repeatable. Prior art involved manually stacking individual material layers and placing aligned stacks into an opaque, vacuum-bagged setup with little assurance of retaining component alignment during part conveyance [60]. The new process uses a heated weight press and pin alignment system, borrowing techniques from printed circuit board fabrication, to achieve very consistent results. The piezoelectric (PZT-5H, Piezo Systems) and alumina ceramic elements, used for the actuator extension, are cut out separately as pick-and-place components. These ceramics elements are laser machined from 5 mil thick plates of bulk material. Layers of 5 mil Garolite, fiberglass-reinforced epoxy laminate, are machined with features and clips to maintain the alighment of the smaller ceramic elements. This Garolite layer, along with

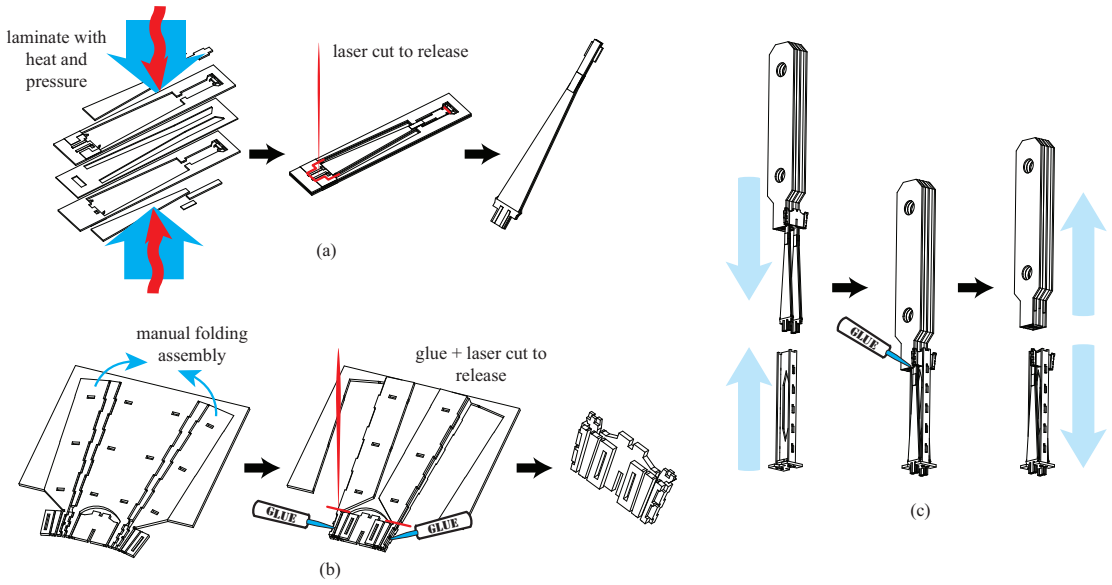

Figure 2.6: Fabrication innovations used in the dual actuator bee. (A) Piezoelectric actuator fabrication starts with mechanical alignment of components using alignment fixtures. Heat and pressure laminates the parts together. The epoxy resin in the carbon fiber middle layer serves as the adhesive. Laser cutting releases the actuator from the surrounding material. (B) Transmission fabrication involves an auxiliary, assembly scaffold to assist in precision folding. Manually fold, glue and laser cut to release. (C) Assembly of parts involves custom fixtures for precision alignment.

the other constituent layers, has identical alignment pin holes to maintain inter-layer alignment during the heat and pressure bonding process. The actuators are characterized for free displacement performance prior to laser cut and release from the composite laminate. These fabrication techniques developed for the dual actuator bee design are illustrated in figure 2.6A.

2.3 Modeling

Researchers have noted that two-winged insects, such as the fruit fly, rely on modulating their wings' angle of attack to perform flight maneuvers [4, 28]. While they utilize power muscles to maintain high-frequency wing flapping, they have a separate set of muscles used to modulate wing rotation about three axes [18]. In contrast, the dual actuator bee design has only two actuators and can only modulate wing flapping motion about a single axis. However, owing to the operation of the actuators, there are a variety of adjustments to the single degree of freedom, including flapping frequency, amplitude, bias of the mean stroke angle (wing bias), and asymmetry between up and down strokes in a single cycle ("split cycle"). In this manner, wing angle-of-attack is modulated indirectly, via passive rotation of the wing, due to dynamic interactions with the air. Passive rotation of the wings was a design choice carried over from the HMF and has been shown to be a viable solution for mimicking insect flight [57]. The basic model below illustrates how the dual actuator vehicle design can generate thrust and achieve roll, pitch, and yaw body torques.

First, a linearized model is used to predict the natural frequency of the system, which will influence the operating frequency of the FWMAV. The derivation of the linearized system model is detailed in Finio [26]. Gain G of the system is defined by the 2^{nd} order transfer function relating input voltage V to output wing displacement

Table 2.1: Physical parameters of the dual actuator bee

Parameter	Symbol	Value	Units
Actuator mass	m_a	25	mg
Wing inertia	J_ϕ	45.3	mg mm^2
Transmission ratio	T	3.333	rad/mm
Radius to center of pressure	r_{cp}	10.1	mm
Aerodynamic damping	b	2.03	μNs/m
Actuator stiffness	k_a	300	N/m
Transmission stiffness	k_t	5.09	μNm/rad
Equivalent mass	m_{eq}	528	mg
Equivalent damping	b_{eq}	0.228	Ns/m
Equivalent spring constant	k_{eq}	356	N/m

X, as a function of frequency ω.

$$G(\omega) = \left|\frac{X}{V}\right| = \left|\frac{A}{m_{eq}(j\omega)^2 + b_{eq}(j\omega) + k_{eq}}\right| \tag{2.1}$$

The equivalent mass, damping, and stiffness are lumped parameters, dependent on various physical parameters of the system which can be found in table 2.1. Equivalent mass m_{eq}, as seen by the actuator, is dependent on the transmission ratio T, actuator mass m_a, and wing inertia J_ϕ. Dampingb_{eq} is dependent on T, the wing's radius of the center of pressure r_{cp}, and aerodynamic damping b. Stiffness k_{eq} is dependent on T, actuator stiffness k_a, and transmission stiffness k_t. The constant factor A is the proportion between input voltage V and output actuator force, dependent on physical parameters of the actuator. Based on this model and the values in table 2.1, the damped natural frequency was calculated to be 104 Hz.

The input voltage signal controlling each piezoelectric actuator is a sinusoid characterized by amplitudeV_{amp}, offset V_{off}, and a variable κ that defines the split cycle asymmetry (figure 2.7). For the pair of actuators per vehicle, V_{avg} is the average of the two input signal amplitudes. Assuming the two signal amplitudes vary symmetrically about V_{avg} with variation V_{dif}, one actuator is driven with an amplitude

$V_{amp} = V_{avg} + V_{dif}$ and the other actuator is driven with amplitude $V_{amp} = V_{avg} - V_{dif}$. The input signals are varied along $V_{avg}, V_{dif}, V_{off}$, and κ, to generate thrust and three torques on the vehicle. Equation 2.2 describes how these parameters influence wing displacement angle ϕ, in radians:

$$\begin{aligned} &\phi = V_{off}G(0) \\ &+V_{amp}G(\omega) \cdot \begin{cases} cos(\frac{\omega t}{2\kappa}) & 0 < t < \kappa \cdot \frac{2\pi}{\omega} \\ cos(\frac{\omega t - 2\pi}{2(1-\kappa)}) & \kappa \cdot \frac{2\pi}{\omega} < t < \frac{2\pi}{\omega} \end{cases} \end{aligned} \tag{2.2}$$

All forces exerted on the vehicle are assumed to come from the lift and drag forces on the wings. These forces are proportional to the square of the wing velocity $\dot{\phi}^2$, as well as drag and lift coefficients C_D and C_L, dependent on the angle of attack α [57]. To linearize the complex relationship between α and $\dot{\phi}$, α is treated as constant throughout the wing cycle, and equal to the angle of attack of the HMF, $\alpha_0 = 45°$. Because the frequency of wing flapping is much higher than the frequency of the body dynamics, the lift and drag forces can be treated as time averaged over the stroke period $P = 1/f = 2\pi/\omega$ (equation 2.3).

$$F_L = \frac{1}{P}\int_0^P dF_L = \frac{1}{4}\rho\beta C_L \left(\omega G(\omega) V_{amp}\right)^2 \tag{2.3}$$

$\rho$is air density and β is a constant representing the specifics of the wing planform geometry.

Thrust F_{thrust} is the sum of both wings' mean lift force magnitudes (equation 2.4). Roll torque τ_{roll} is the difference in mean lift force magnitude between the two wings. Recall the lift force is a function of $V_{amp} = V_{avg} \pm V_{dif}$.

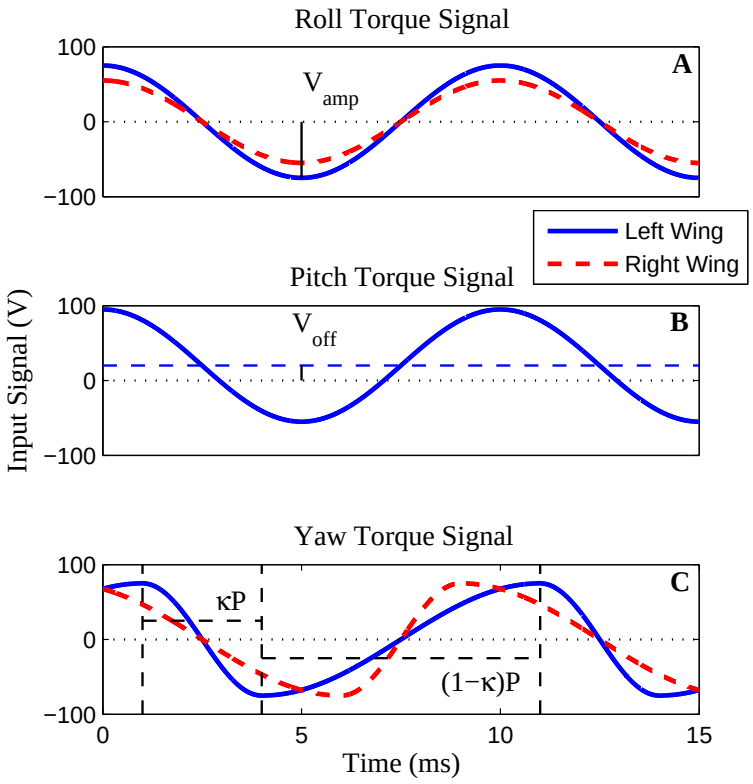

Figure 2.7: Examples of signals that would be used to generate body torques on the FWMAV. The signals shown would activate: (A) roll torque by varying V_{dif} ($V_{dif} = 10$), (B) pitch torque by varying V_{off} ($V_{off} = 20$), and (C) yaw torque by varying κ ($\kappa = 0.3$).

$$\begin{aligned} F_{thrust} &= F_{L,left} + F_{L,right} \\ &= \frac{1}{2}\rho\beta C_L \left(\omega G(\omega)\right)^2 \left(V_{avg}^2 + V_{dif}^2\right) \end{aligned} \tag{2.4}$$

$$\begin{aligned} \tau_{roll} &= r_{cp}\left(F_{L,left} - F_{L,right}\right) \\ &= r_{cp}\rho\beta C_L \left(\omega G(\omega)\right)^2 \left(V_{avg} V_{dif}\right) \end{aligned} \tag{2.5}$$

Pitch torque τ_{pitch} is caused by the combined lift force vector of both wings offset from the vehicle center of mass in the foreaft direction. This offset is caused by a bias in the wing's mean stroke angle ϕ_{mean} (toward the front or back of the vehicle), which is proportional to V_{off} of the input signal.

$$\begin{aligned} \tau_{pitch} &= r_{cp} sin(\phi_{mean}) \left(F_{L,left} + F_{L,right}\right) \\ &\approx r_{cp} V_{off} G(0) F_{thrust} \end{aligned} \tag{2.6}$$

for small ϕ_{mean}.

Yaw torque τ_{yaw} is achieved through a difference in the drag force between the wings' upstroke and downstroke. This is accomplished when the upstroke velocity is different than the downstroke velocity; larger drag forces occur during the quicker stroke. τ_{yaw} is dependent on κ, denoting the fraction of the cycle period that is occupied by the upstroke; $\kappa = 0.5$ indicates a pure sinusoid. The mean drag force of each wing is determined by integrating the drag force over the stroke period:

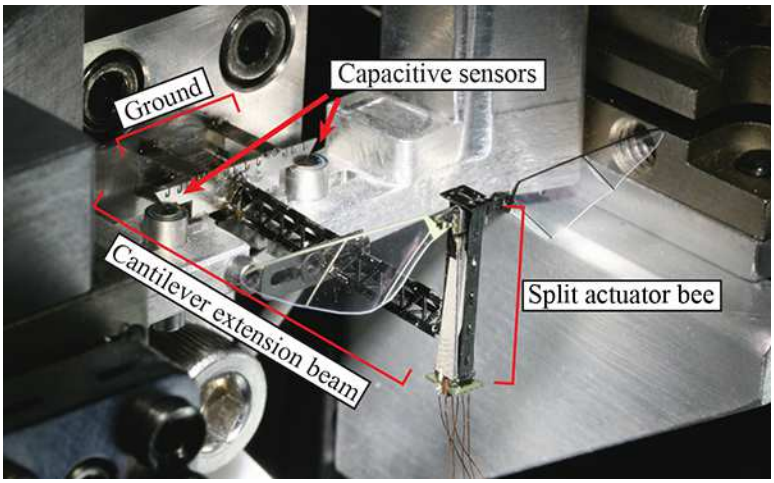

Figure 2.8: The dual actuator bee mounted on a custom dual-axis force-torque sensor. Measuring all three body torques requires remounting in different orientations. Here, the vehicle is mounted for roll torque measurements.

$$\begin{aligned} F_{D,left} &= -F_{D,right} \\ &= \frac{1}{P}\left[\int_0^{\kappa P} F_{D,upstroke} - \int_{\kappa P}^{P} F_{D,downstroke}\right] \end{aligned} \tag{2.7}$$

$$\begin{aligned} \tau_{yaw} &= r_{cp}\left(F_{D,left} - F_{D,right}\right) = 2r_{cp}F_{D,left} \\ &= \frac{1}{8} r_{cp}\rho\beta C_D \left(\omega G(\omega) V_{amp}\right)^2 \left(\frac{1-2\kappa}{\kappa-\kappa^2}\right) \end{aligned} \tag{2.8}$$

2.4 Early experimental results

The first completed dual actuator bee weighed 70 mg, comparable with the legacy 60 mg HMF[61]. The vehicle was mounted on a custom dual-axis force-torque sensor consisting of a stiff cantilever beam and two capacitive sensors, shown in figure 2.8. This sensor can measure a single axis of torque and a single force perpendicular to the torque axis. To measure torque generation in three directions, the vehicle had to be

remounted in different orientations. The resonant frequencies of the two wing drives on the vehicle were empirically determined to be approximately 95 Hz and 105 Hz. For each experiment, a 100 Hz signal (the average resonant frequency between the two wing drives) parameterized by $V_{avg}, V_{dif}, V_{off}$, and κ was input into the vehicle via a power tether for one second, and instantaneous force and torque were recorded at a sample rate of 10 kHz. The force and torque were averaged over the one second in order to obtain the measured force and torque.

To measure thrust and roll torque, the input signal's V_{avg} was discretely varied from 85V to 105V while the V_{dif} was discretely varied from -10V to 10V. When measuring pitch torque, V_{off} was varied from -20V to 20V, and when measuring yaw torque, κ was varied from 0.3 to 0.7.

Because fabrication variability can affect system properties, G was determined empirically by observing wing displacement at the operating frequency. This value was used in the models to predict thrust and torques.

To account for misalignments in mounting to the experimental setup and unavoidable fabrication asymmetries in the vehicle when collecting torque measurements, the measured torque was broken down into the activated torque τ_{act}, the offset of the vehicle's center of mass from the torque sensor's rotation axis r_{mis} times the thrust F_{thrust}, and a torque offset τ_0 due to differences in wing performance. r_{mis} and τ_0 were calculated via a linear fit of all data taken when the torques' dominant input variable (V_{dif}, V_{off}, κ) was inactive. The measured torque data was adjusted accordingly.

$$\tau_{measured} = \tau_{act} + r_{mis} F_{thrust} + \tau_0 \tag{2.9}$$

Figure 2.9 compares the measured thrust to the thrust expected by the model as a function of V_{avg}. Thrust shows a positive correlation with V_{avg}, with a maximum measured thrust of 1.36 mN, approximately twice the force necessary for the 70 mg

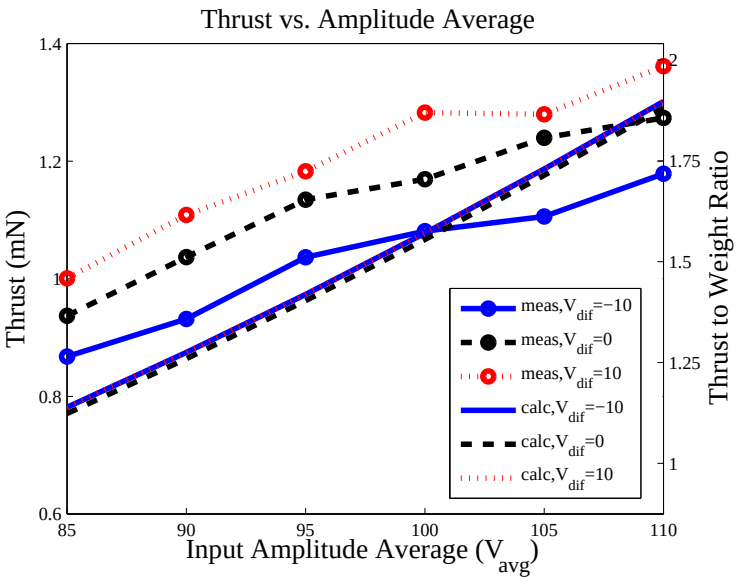

Figure 2.9: Measured and calculated thrust as a function of the average signal amplitude V_{avg}. The thrust was observed with input amplitude differences between the wings V_{dif} of -10V, 0V, and 10V.

vehicle to hover. Contrary to the model, the increase in measured thrust as V_{dif} varies is much more pronounced. This was due to a fabrication error in the test vehicle that resulted in one of the wings performing better than the other in terms of force generation. Thus, a V_{dif} that favored the better performing wing cause the net thrust of the vehicle to increase.

Figure 2.10 shows the three measured torques at three different values of V_{avg}. In each case, the measured torque is plotted with the model's predicted torque. Each torque exhibits a positive correlation with the corresponding signal variable. We see that for roll torque τ_{roll}, the model is underestimating the torque generated. It also appears that the τ_{roll} range has a marked decrease for the high V_{avg} value. The pitch torque τ_{pitch} appears to match well with the model, except at the extreme values of V_{off}. All of these discrepancies between the model and the experimental data for roll and pitch torques seem to indicate that there is a breakdown in the linearity of the system as the wing drives reach the limits of their motion. This could be attributed

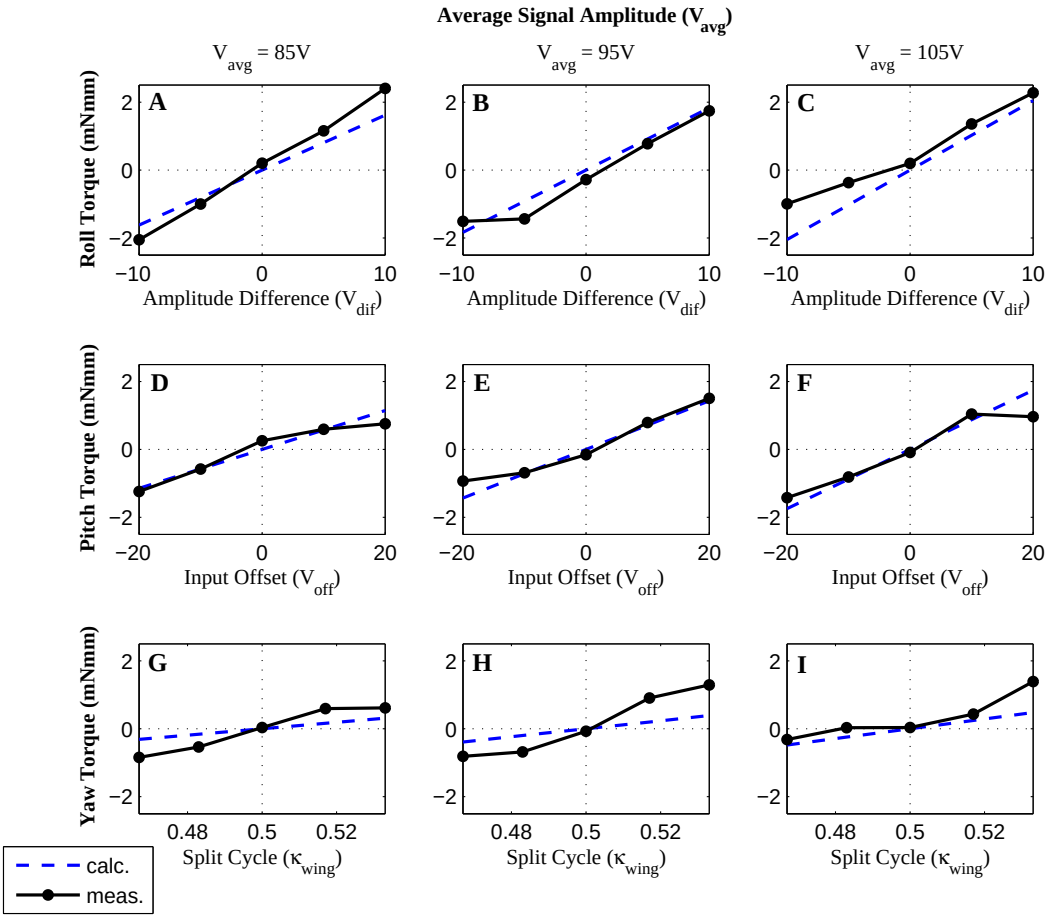

Figure 2.10: Measured and calculated torques as a function of their corresponding signal variable. Each torque was observed when V_{avg} was 85V, 95V, and 105V. (A-C) Roll torque τ_{roll} is shown as a function of V_{dif}. (D-F) Pitch torque τ_{pitch} is shown as a function of V_{off}. (G-I) Yaw torque τ_{yaw} is shown as a function of κ_{wing}.

to kinematic nonlinearity in the transmission four-bar or to the linearization error in the system model.

In the yaw torque τ_{yaw} case, the model is consistently underestimating the torque generated, indicating a lack of fidelity in the modeling. The experimental data also indicates a nonlinear relationship between the wing trajectory κ_{wing} and output τ_{yaw}—the increase in torque magnitude tapers off for extreme κ's. The asymmetry of the wing stroke, κ_{wing}, did not match the asymmetry of the input signal, defined by κ. The input κ value of 0.3 resulted in the equivalent wing output κ_{wing} value of 0.467. Similarly, a $\kappa = 0.7$, which mirrors the assymmetry of $\kappa = 0.3$, resulted in $\kappa_{wing} = 0.533$. The system appears to be resisting deviations away from a sine wave, a characteristic of resonant mechanical systems. It is possible that κ is too simple a parameterization to define split cycle flapping, and a different parameterization is required to output the desired wing trajectories.

Concerning the magnitude of the body torques generated, the vehicle is on par with flight performance of fruit flies. Fruit flies have been observed to make 90° turns in less than 50 ms about their major inertial axis[28]. In the dual actuator bee vehicle design, that corresponds to the roll axis. With a maximum measured roll torque of $3mN \cdot mm$ and an estimated maximum body inertia of $1.0322g \cdot mm^2$, the vehicle should be able to perform a 90° turn in 23 ms, by accelerating for 45° and decelerating for 45°. Body drag due to angular velocity is not taken into account, but the performance is of the same order of magnitude as fruit flies.

2.5 Controlled flight

After the initial validation of body torque generation ability, as presented in Section 2.4, more dual actuator bee prototypes were developed, and their fabrication and

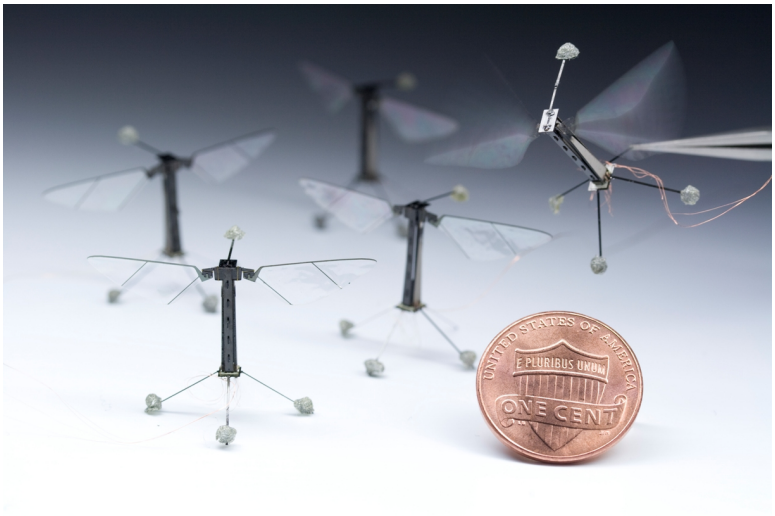

Figure 2.11: Five individual dual actuator bees are shown alongside a U.S. penny for scale, demonstrating the repeatability of the fabrication process.

assembly procedures were refined, as described in Chapter 5. The refinements to the design have allowed for multiple vehicle prototypes to be constructed and operational for numerous experiments. Figure 2.11 showcases the repeatability of the fabrication process.

Active modulation of thrust force and three body torques permits the robot to be controllable in unconstrained flight. The wing motions to generate body torques are described in Figure 2.12. To achieve stable flight, we must implement an active flight controller because, similar to flying insects, the dynamics of our insect-scale vehicle are fast and unstable [5]. Sensing and controller computation are performed off-board, and power and control signals are sent to the robot via a wire tether.

To sense the state of the robotic fly, we operate the robot in a virtual volume defined by an external array of motion-capture cameras; position and orientation are estimated by observing retroreflective tracking markers mounted on the robot, illustrated in Figure 2.13. Taking into account the sampling frequency of the motion-capture system (500 Hz), the latency of the computation, and the phase shift caused

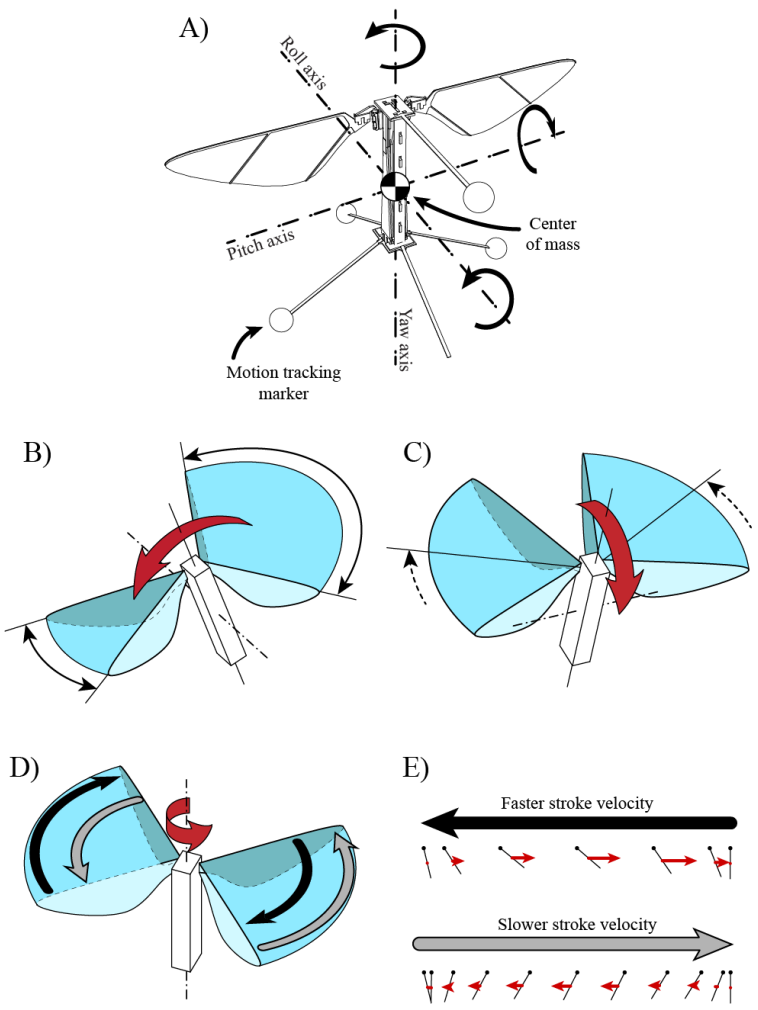

Figure 2.12: A) Body axes definitions of the dual actuator bee. The approximation center of mass location is identified. B) Roll torque is generated by flapping one wing with larger stroke amplitude than the other, inducing differential thrust forces. C) Pitch torque is generated by moving the mean stroke angle of both wings forward or backward to offset the thrust vector away from the center of mass. D) To generate yaw torques, the robot influences wing drag forces by cyclically modulating stroke velocity in a "split-cycle" scheme. A difference in stroke velocity between upstroke and downstroke results in a net drag force per stroke cycle—the higher velocity half-stroke (black arrow) produces greater drag force. By modulating magnitude and direction of this mean drag force on both wings, yaw torque is generated. The black and grey arrows correspond to arrows in E. E) The effect of stroke velocity on a wing's drag force. Black lines indicate the wings' position and pitch angle at temporally equidistant points within the stroke cycle. The red arrows indicate the instantaneous drag force on the wing.

by the electromechanical dynamics of the actuators, we estimated the total latency of the robotic fly's sensorimotor system to be approximately 12 ms. This proved to be sufficiently high-bandwidth for the fast rotational dynamics of our insect-sized vehicle and is comparable to the 10 ms latency measured in the neuromotor reflexes of fruit flies [49].

Greater details on the flight controller can be found in [5]. The flight controller design consists of three distinct modules controlling body attitude, lateral position, and altitude and is subject to the constraints of the mechanical system; the stroke planes of the wings, and thus the direction of their time-averaged thrust vectors, essentially remain fixed with respect to the robot's body axis. To stay aloft, the robot must maintain a nominally upright orientation via stabilizing body torques such that its net thrust vector compensates for gravity. To induce lateral forces, the robot must reorient the body so that the net thrust vector takes on a lateral component. The control law consists of a proportional term that accounts for the error from a reference orientation and a derivative term that opposes angular velocity—providing rotational damping. The lateral position controller module operates by calculating the necessary reference orientation for the body attitude controller module to produce the appropriate lateral force component.

The altitude controller does not rely on information about body attitude; it is based on a linearization of the robot's dynamics at hover and assumes the system is always at an upright orientation. This decoupling of the controller allows for reduced constraints on the more sensitive attitude and lateral position controllers. In practice, the robot effectively maintains altitude because the body attitude does not deviate significantly from the nominal upright orientation even when generating compensatory lateral forces.

In flight tests, the robotic fly demonstrated stable hovering about a fixed point,

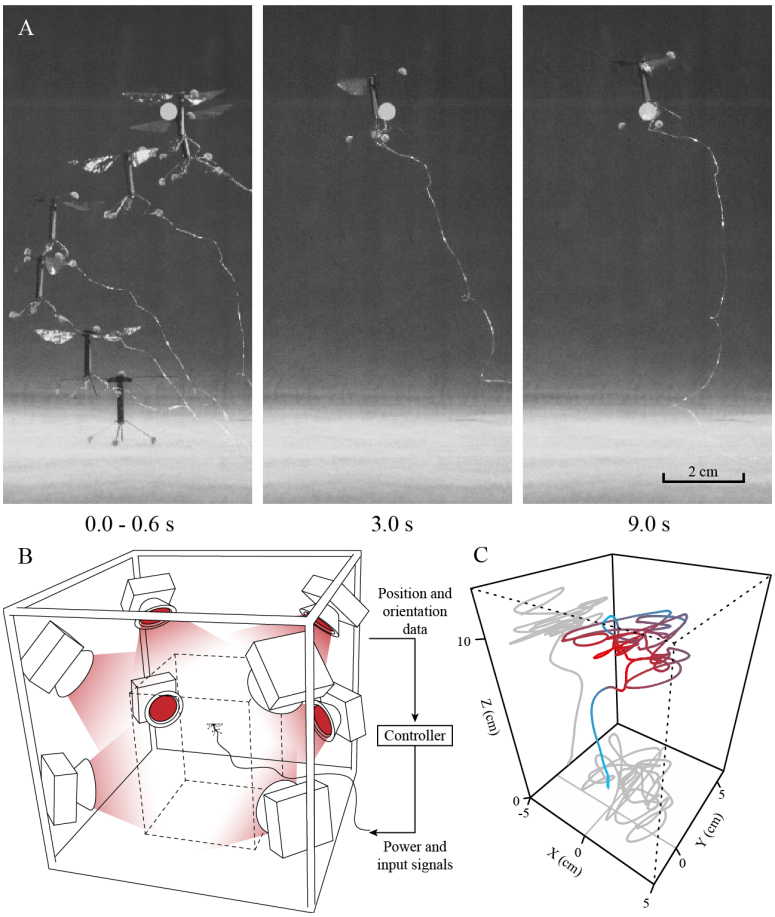

Figure 2.13: Controlled takeoff and hovering of the dual actuator bee. A) Select frames from a flight video shows the dual actuator bee ascending to the hovering setpoint (white dot) and maintaining the setpoint position for over 9 seconds. B) Infrared motion tracking cameras observe the position of retroreflective markers attached to the vehicle in order to estimate its position and orientation in space. State information is sent to a host computer which computes the required control signals to stabilize the flight trajectory and sends them to the vehicle via a wire tether. C) Three-dimensional reconstruction of a hovering flight trajectory. Hovering setpoint was 10 cm above ground. Line color gradient indicates distance from the target point, with red indicating closer proximity.

as depicted in Figure 2.13, with position errors on the order of one body length around the target position, sustaining flights for longer than 20 seconds without ever approaching a crash. It also demonstrated lateral flight maneuvers, alternating between two fixed points in space by a switch of the target lateral position.

2.6 Concluding remarks

The dual actuator bee design became the first insect-scale flying robot to achieve controlled, hovering flight. This was accomplished by a combination of flightworthy mechanical design, a robust actuation scheme for flight control, and well-considered fabrication and assembly methods. Its development was greatly informed by the Harvard Microrobotic Fly, which validated the vehicle morphology, construction methods and materials that could produce a flight-capable, insect-scale vehicle. The dual actuator bee demonstrates that a similarly-sized vehicle can be constructed and outfitted with more complex mechanical design. It retains flightworthiness while contributing the ability to generate body torques and thus enabling the vehicle to stabilize its flight. The effectiveness of this design for body torque control was demonstrated by the implementation of a closed-loop flight controller.

Experimental characterizations of the vehicle's force and torque capabilities were also carried out but should be considered preliminary. More refinement to the vehicle characterization setup is required. With the current sensor configuration, interfacing the vehicle to the sensor setup is difficult and prone to misalignment or damage to the vehicle. Reorienting the vehicle to measure torques about the three body axes is inconvenient and necessitates a 3-axis torque sensor for this scale, or a better method of detaching and reattaching the vehicle to the setup. Once an improved sensing setup is developed, the force and torque performance limits of the vehicle design should be

identified. This will provide useful information for more aggressive flight controllers and facilitate research efforts towards an optimized vehicle mechanical design.

Flight experiments highlighted the importance of fabrication precision and reliability as an enabling factor for this FWMAV morphology. Because the vehicle design features two decoupled wing drives, and because the dynamics are fast and unstable, vehicle mechanical symmetry is critical. Chapter 5 presents further refinements to the manufacturing of the dual actuator bee design and provides details on a systematic fabrication and assembly analysis. The manufacturing insights gleaned from the dual actuator bee development can greatly inform and contribute to the successful development of future insect-scale FWMAVs.

A combination of flightworthiness and manufacturability enables the dual actuator bee to be a versatile research testbed for insect-scale FWMAV research. The vehicle design has provided a crucial platform for the development of flight controllers and sensors and has flown with a variety of payloads including an ocelli light sensor [31], IMU [30, 32], proximity sensor, magnetic wall attachments [6], and electrostatic adhesives. It has flown in controlled wind gusts and even demonstrated swimming underwater. However, the dual actuator bee was not designed to carry large payloads. Eventually, the parallel developments on various electronics, sensors, and auxiliary components will converge on a suitable electronics package for control and power autonomy, one with a greater weight than the lifting capabilities of the dual actuator bee. A new vehicle with more payload capacity will be required in order to carry a full electronics and sensors suite and is the subject of the next chapter.

Chapter 3

Scaling up for control autonomy

The dual actuator bee design described in Chapter 2 has demonstrated the ability to generate both sufficient thrust to lift its own weight and body torques for flight stabilization. With the addition of a closed loop flight controller, the vehicle successfully demonstrated controlled hovering and basic flight maneuvers. The vehicle design has become a crucial research platform in developing flight controllers [7] and sensor suites for insect-scale, flapping-wing micro air vehicles. Sensors that have been implemented on the flying robot include an ocelli (light sensing array), gyroscope, and magnetometer [31, 30, 32].

However, the dual actuator bee has critical limitations as a research platform. A limited payload capacity prevents it from carrying the complete suite of requisite sensors, control and power electronics, and power source necessary for power and control autonomy. Instead, the operation of the vehicle requires a wire tether for power and control signal input. Flight control relies on offboard motion capture for sensory feedback of vehicle dynamics, instead of onboard sensors. And due to a coupling of thrust and torque production, when the vehicle is loaded near its payload capacity limits, control authority is severely reduced.

To create a fully autonomous insect-scale flying robot, a vehicle with more thrust force is required. In this chapter, we explore and demonstrate the feasibility of scaling

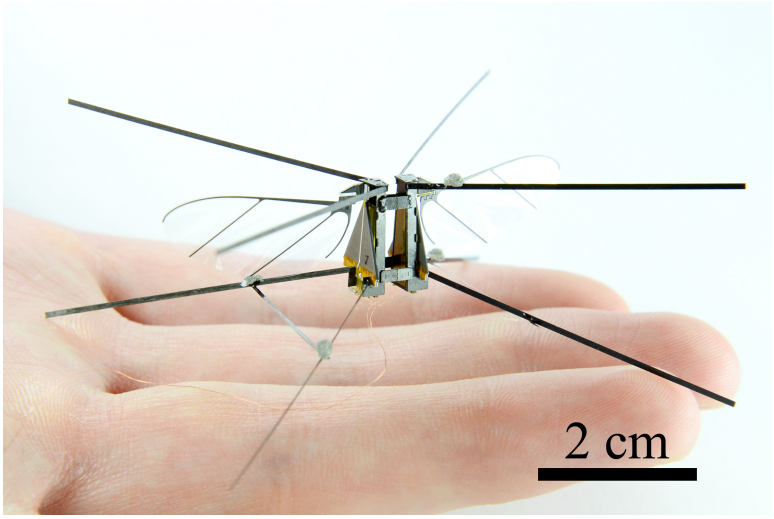

Figure 3.1: The prototype robotic flying insect shown here has a wingspan of 5.5 cm and a mass of 380 mg when fully loaded. It has spars extending off the airframe that act as a roll cage to protect the wings from crash damage. Motion tracking markers for control are also attached to these spars.

up the established vehicle design to increase its thrust force capability. The system design space for this novel class of flapping-wing micro air vehicle is high-dimensional and complex. To simplify the design problem, we use a scaling heuristic that relies on maintaining properties of the dual actuator bee. We target the specific payload requirements necessary for control autonomy and develop a mechanical design for the scaled vehicle that is well-suited for electronics integration, utilizing the latest fabrication methods. We construct a 265 mg flying vehicle, which we call "BigBee," and demonstrate a 115 mg payload capacity, sufficient for supporting control-autonomous flight with recently-developed, miniaturized electronic components. The new flight result demonstrates feasibility of scaling the established vehicle design and contributes an additional operational reference point for optimization studies towards a fully autonomous insect-scale flying robot.

3.1 System design

This chapter explores the design and fabrication challenges of scaling an established micro air vehicle design that employs flapping wings, mimicking real flying insects. The scaling laws for flapping-wing micro air vehicles have been explored in theory [20, 58] and have provided key relationships between certain vehicle design parameters. However, while they can capture scaling trends, the theoretical models have not been used to generate quantitative specifications for practical vehicle design. Due to lack of fidelity in the modeling, particularly the aerodynamics, accuracy relies on fitting to scale-specific experimental measurements and have questionable accuracy for generating design specifications at other scales [57]. There is little practical guidance for designing and constructing flapping wing air vehicles at the insect scale.

Full system-level optimization of flapping wing air vehicles is a complex, high-dimensional problem with significant interdependence between various design parameters. Considering the aerodynamics of flapping wing flight alone, thrust force production from a single flapping wing predominantly relies on two degrees of freedom—wing flapping and wing pitch rotation [28]. While the aerodynamics are time dependent and unsteady, cycle-averaged, quasi-steady approximations can be used [21]. Force production is dependent on flapping frequency, stroke amplitude, wing pitching amplitude, stroke-to-pitching phasing, and wing geometry—itself parameterized by wing length, wing aspect ratio, and moments of area ([57, 14, 22]). The scaling laws for flapping-wing aerodynamics and system dynamics, in addition to power efficiency considerations [35], need to be reconciled simultaneously in order to identify an optimal design for a high-performance air vehicle.

To accelerate development towards a more payload-capable vehicle, we present a design heuristic that essentially scales the dual actuator bee vehicle design. By holding constant many properties of an already flightworthy and operational vehicle, we

restrict the scaling analysis to a few key parameters, simplifying the design problem.

3.1.1 Design goals

The key design specification for this research effort is the payload capacity of the vehicle. We must estimate the target payload requirements of the vehicle. Table 3.1 lists the minimum known set of electronic components needed for autonomous flight control, as of this writing, and the mass of each component. Noticeably missing from Table 3.1 is an onboard battery for powering the robotic vehicle. For the sake of near-term research progress, our working goal is control autonomy—not power autonomy—and assume that electrical power will still be fed to the robot through a wire tether. A more directed effort to reduce battery mass and increase battery energy density is needed prior to adding its mass contribution to the robot's payload.

In addition to the electronics' static payload contribution, we look toward the component mass fractions of the dual actuator bee for further design direction. Relevant numbers for this discussion from the previous design are listed in Table 3.2. We hypothesize that a larger scale vehicle would have similar actuator mass fractions, extrapolating from observations on flying insects that found muscle mass fraction to be the best indicator of thrust-to-weight ratio [41]. The dual actuator bee has a payload capacity in controlled flight of about 35 mg [30], on top of a 80 mg unloaded body mass. Based on the 100 mg known total payload needed for control autonomy from Table 3.1, we size a vehicle with at least 3× the payload capacity of the dual actuator bee in order to carry it, or 105 mg. We scale the target body mass similarly by 3× to 240 mg, for a total loaded robot mass of 345 mg. Of the 240 mg body mass, 5/8 would be actuator mass, or 150 mg, and 3/8 would be mechanism and structure

Table 3.1: Electronic components necessary for control autonomy

Component	Mass (mg)	Additional physical requirements
"Brain" chip (System-on-Chip microprocessor) [62]	10	
Power electronics [35]	40	Place close to the vehicle base
Inertial measurement unit (IMU) (gyroscope+accelerometer) (Invensense MPU6500)	25	Place close as possible to vehicle center of mass
Optic flow sensor [19]	15	Place downward facing with unobstructed view
Flexible Kapton PCB and electronic integration overhead	10	
Total	100	

Table 3.2: Design parameters from the dual actuator bee in Chapter 2. Design goals and results for the scaled up BigBee vehicle design.

Vehicle parameter	Units	Dual actuator bee	Scale factor	BigBee goals	BigBee results
Flapping frequency	Hz	100	f_{scale} =0.6–0.85	60–85	70
Wing length	mm	15	R_{scale} =1.7	25.5	25.5
Total unloaded robot mass	mg	80	W_{scale} =3	240	265
Total loaded robot mass	mg	115	3	345	380
Measured payload capacity	mg	35	3	105	115
Measured maximum thrust force	mg	140	$\approx$3	414	450
Thrust-to-weight (loaded) ratio	N/A	1.2	hold constant		1.18
Actuator mass fraction	N/A	0.625	hold constant		0.74
Transmission ratio (T)	rad/mm	3.28	hold constant		3.28
Actuator unloaded displacement (δ)	mm	0.85	hold constant		0.85
Actuator base width	mm	1.75			8.606
Wing shape parameter ($\hat{r_2}$)	N/A	$<$0.55			0.55

mass, or 90 mg.

Additionally, the dual actuator bee design has a coupling between thrust force and body torque production. The piezoelectric bimorph cantilever actuators used to power the flapping wings practically operate within voltage bounds from 0–300V, constrained by the ceramic material's strain limits. Within those bounds, a sinusoidal driving signal of varying amplitude and offset can operate. Signal amplitude modulates wing stroke amplitude and thus thrust magnitude. Signal offset modulates the mean wing stroke angle and is used to generate pitch torque in the vehicle by moving the thrust vector fore-aft relative to the vehicle center of mass. If the thrust needed to lift the vehicle is very large, signal amplitudes will increase until maxing out the 300V range. Near this operating point, achievable signal offsets become very limited, which will limit the pitch torque production ability and consequently the flight stability and control authority of the vehicle. Therefore, the maximum thrust output of the vehicle should not be used to calculate the payload capacity; else, the fully loaded vehicle would be unable to produce body pitch torques.

The dual actuator bee had a thrust-to-weight ratio of 1.2 when loaded and hovering. Mimicking this, the required maximum thrust force from the BigBee is $1.2 \times 345 = 414$ mg, which is about $3\times$ the maximum measured thrust force from the dual actuator bee. The design goals for BigBee are listed in Table 3.2.

3.1.2 Scaling heuristic

The dual actuator bee design has two flapping wings, each wing independently driven with a separate piezoelectric linear actuator. A four-bar linkage acts as a transmission to amplify the actuator input and produce wing flapping motion. Two separately driven wings enable the vehicle to generate body torques, which is crucial for stabilizing and maneuvering in flight.

To expedite the scaling analysis, we hold constant all key design parameters except the wing length and the flapping frequency. We designate R_{scale} as the wing length scaling factor and f_{scale} as the flapping frequency scaling factor, scaled relative to the dual actuator bee parameters. To preserve the wing kinematics of the dual actuator bee design, we preserve its transmission ratio of $T = 3.28$ rad/mm and the actuators' unloaded input displacement amplitude to $\delta = 0.85$ mm. For the wing shape, we use the wing morphology from the experiments of [14], with a second wing shape moment $\hat{r_2} = 0.55$ (as defined by [22] as the second moment of area normalized by wing area) and an aspect ratio of 3. This wing shape was found to be an improvement in lift-to-drag ratio over that of the dual actuator bee. R_{scale} will scale the wing planform dimensions uniformly.

Aerodynamic forces stemming from flapping wings can be estimated with the blade element method, as described in [58], which assumes aerodynamic force is proportional to local dynamic pressure on the wing. Dividing the flapping wing into chordwise blade elements, the aerodynamic force (either lift or drag) on a single element can be described as:

$$F_{aero} = \frac{1}{2}\rho\left(\dot{\phi}r\right)^2 C_{aero}\left(\alpha\right) S \tag{3.1}$$

where ρ is the air density; C_{aero} is the aerodynamic force coefficient—a function of instantaneous wing angle of attack α and wing geometry; S is the area of the blade element; and $\left(\dot{\phi}r\right)$ solves for the local velocity of the wing element—it is the product of wing stroke angular velocity $\dot{\phi}$ and local radius r. Total instantaneous force on the wing is found by radial integration over the wing's length R. As we are holding wing kinematics and wing geometry constant, Eq.3.1 indicates that the aerodynamic force scale factor $F_{aero,scale}$ will scale with R_{scale} and f_{scale} as:

$$F_{aero,scale} \propto R_{scale}^4 \cdot f_{scale}^2 \tag{3.2}$$

As the actuators are driving the flapping wings, the required blocked force from the actuators F_b to produce a thrust force W was approximated by Eq.14 of [58], reproduced here:

$$F_b = W \frac{\widetilde{C_D}}{\frac{1}{2}\widetilde{C_L}} \cdot T\hat{r_{cp}}R \tag{3.3}$$

where $\widetilde{C_L}/\widetilde{C_D}$ is the lift-to-drag ratio, T is the transmission ratio, and $\hat{r_{cp}}$ is non-dimensional wing center of pressure radius. As we are fixing the wing kinematics and wing geometry in this analysis, these parameters are constants. Actuator stiffness k_{act} is the ratio of blocked force F_b to unloaded actuator displacement δ: $k_{act} = {}^{F_b}/_{\delta}$. Actuator displacement is fixed and thus k_{act} is proportional to F_b. Combining with Eq. 3.3, the scaling relationship between the actuator stiffness scale factor $k_{act,scale}$, thrust force scale factor W_{scale}, and R_{scale} is:

$$k_{act,scale} \propto W_{scale} \cdot R_{scale} \tag{3.4}$$

Wing inertia is related to the wing morphology. Assuming wing shape does not change, if the wing planform is parameterized by R_{scale} and the wing area dimensions scale uniformly with R_{scale}, then wing inertia I_{wing} should scale with R_{scale}^4. However, for this design exploration, not all wing dimensions are scaled uniformly. A wing consists of a thin structural frame overlaid with a wing membrane, and most of the wing's mass is attributed to the frame. Scaling the frame spar widths uniformly with the wing planform adds wing inertia without contributing significant stiffness. Thus, the wing spar widths are fixed as the wing planform area is scaled. Fixing the wing shape, we use CAD modeling to empirically determine how wing inertia scales with R_{scale}. We determined the scaling law through manual fitting of a power function and

found it to be:

$$I_{wing} \propto R_{scale}^{3.7} \tag{3.5}$$

To determine the wing length and flapping frequency of the scaled vehicle, we apply two constraints in the system modeling. First, the vehicle must generate the target thrust force. Second, the vehicle's flapping-wing system should be operating at its natural frequency. From the analyses performed in [26], we know that this form of flapping-wing mechanism driven with piezoelectric linear actuators can be approximated as a harmonic oscillator. Consequently, there is a distinct natural frequency at which wing stroke amplitudes, and therefore mechanical energy transfer, is greatest. Approximating the system as a harmonic oscillator provides an expression, shown in Eq.3.6, for the system's natural frequency ω_n. This relationship assumes that the actuators are the primary contributors of system stiffness k_{act} and that the wings are the primary contributors of system inertia I_{wing}.

$$\omega_n = \sqrt{\frac{k_{act}}{I_{wing}}} \tag{3.6}$$

Consequently, combining Eq.3.4 and Eq.3.5 with Eq.3.6 results in the following scaling relationship between the natural frequency scale factor $\omega_{n,scale}$, W_{scale}, and R_{scale}:

$$\omega_{n,scale} \propto W_{scale}^{0.5} \cdot R_{scale}^{-1.35} \tag{3.7}$$

To meet both of our design constraints, we equate f_{scale} with $\omega_{n,scale}$ and W_{scale} with $F_{aero,scale}$.

Figure 3.2 shows curves for Eq.3.2 and Eq.3.7 with $F_{aero,scale} = W_{scale} = 3\times$ the magnitude of the dual actuator bee, plotted over the f_{scale} vs. R_{scale} space. Any

operating point along the aerodynamic scaling curve from Eq.3.2 should theoretically produce the requisite thrust force, establishing a candidate target wing length and flapping frequency. The curve for the natural frequency scaling suggests that the system natural frequency as estimated in Eq.3.7 scales slower than the target flapping frequency.

We can interpret these curves as an upper and lower bound on our design space. Limited by wing inertia and wing structural limits, we cannot simply increase the flapping frequency of the dual actuator bee to attain greater thrust force. An alternative is to increase wing length (and thus wing inertia) and flap at a lower frequency. As illustrated in Figure 3.2, aerodynamic scaling dictates a wing length 1.3× longer to ensure a flapping frequency scaling of less than 1. Natural frequency scaling suggests a wing length 1.5× longer to ensure the same.

Weighing in our intuition on structural limits of our current wing fabrication methods, we choose a wing length scaling of 1.7× as a starting point for exploration into scaled vehicle fabrication. With 1.7× longer wings, a 0.6× lower flapping frequency is sufficient to generate the target thrust force; a 0.85× lower natural frequency is also predicted. We anticipate the actual operating frequency of the BigBee will fall in between these predictions. Table 3.2 lists the target design parameters for the BigBee.

3.2 Vehicle fabrication

We utilize our latest fabrication methods to construct the prescribed vehicle design. In determining our methods, we are reconciling the need for high-performance components with the efficiency of their production. To effectively support further system experimentation, we are interested in producing on the order of 10 vehicles. Ide-

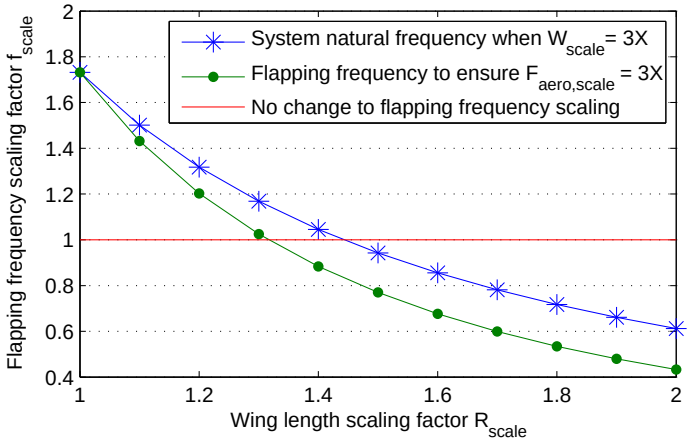

Figure 3.2: Scaling trends between flapping frequency and wing length. One is derived from aerodynamic modeling to ensure 3× the thrust force output (Eq.3.2), and the other is the predicted system natural frequency under 3× the aerodynamic loading (Eq.3.7).

ally, the vehicles should be identical in properties and performance. Prior experience suggests this is very difficult to achieve, but as methods continue to be refined, we gradually approach this ideal. More detail on this topic can be found in Chapter 5. The mechanical system can be divided into separate components, each with distinct manufacturing considerations.

3.2.1 Wings

The wings are fabricated in batches as thin polyester film laminated over a monolithic, laser-machined carbon fiber frame, a method identical to what was used for the dual actuator bee. They should be lightweight, stiff, resilient to aerodynamic loading, and efficient to reproduce. The wing shape is fixed as described in Section 3.1.2.

Because the BigBee will generate more thrust force, the wings will experience greater aerodynamic loading. As a simple approximation, if we are using the 1.7× longer wings to generate 3× more aerodynamic force, this translates to 5.1× greater bending moment at the wing base due to aerodynamic loading. In this initial effort, we

increased the wing frame's carbon fiber beam thickness by 50%, increasing the bending stiffness by 3.4×. Experiments indicate that the wings are stiff enough to withstand the aerodynamic loading without bending. However, without further characterization studies, we are not certain to what extent the new wings are sufficiently robust. To prevent wing damage during operation, we add a roll cage consisting of thin carbon fiber spars that prevent the wings from hitting the ground, as seen in Figure 3.1.

3.2.2 Actuators

The piezoelectric ceramic bimorph actuators used in BigBee are based on the design from [60]. Improvements to the manufacturing and performance of these actuators are presented in [34] and represent the state-of-the-art. A few additions were made to the actuators used in this vehicle design. We use non-conductive fiber glass "bridges" instead of conductive carbon fiber bridges to decrease the chance that damage to the electrically-insulating parylene coating will cause an electrical short. We also add discrete flex circuit components to the actuators, so that the electrical interface to them can extend below the base of the vehicle and make the electrical wiring task easier (see Figure 3.3).

We use the actuator model from [60] to determine the geometry of the new actuators. Because the transmission and actuator displacement properties are fixed, the increased wing loading (Section 3.2.1) directly translates to a 5.1× larger blocked force requirement for the actuators. Actuator blocked force is proportional to the nominal actuator width [60]. To meet the greater force requirements, the new actuators are larger: the piezoelectric ceramic layer is 8.332 mm in length and 8.606 mm in base width. Figure 3.3 illustrates the actuators' design and implementation in the vehicle.

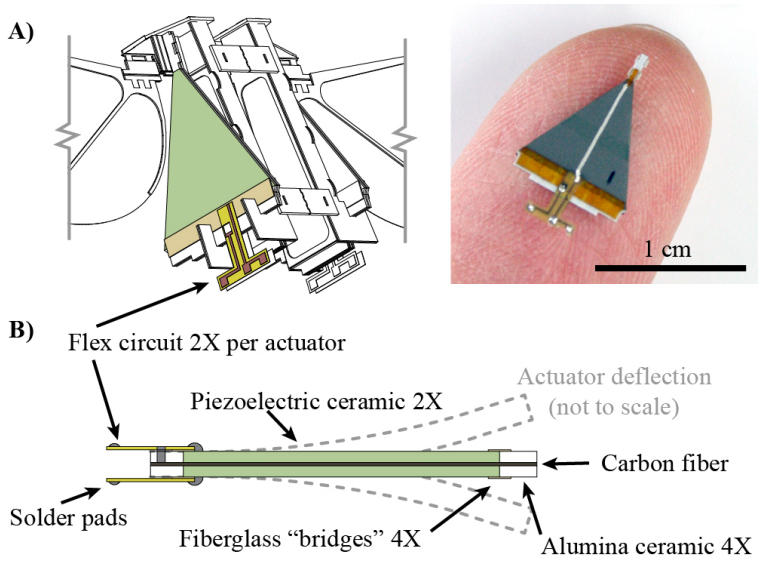

Figure 3.3: A) Wiring of the vehicle's piezoelectric bimorph actuators is performed manually. Discrete flex circuit elements are implemented on the actuators to extend the electrical contacts below the vehicle and facilitate manual electrical interfacing. B) The actuators are layered composite beams of piezoelectric ceramic (PZT-5H), alumina ceramic for the base and tip, and carbon fiber for the central elastic layer [34]. Fiberglass "bridges" reinforce the four ceramic material interfaces. Flex circuits with accessible solder pads are attached to electrically interface with the actuators. Actuator not shown to scale.

3.2.3 Transmission

The transmission is a four-bar linkage that converts the motion of the actuator tip to flapping wing motion. Kinematically, this requires a conversion of the rotational tip motion of the bimorph actuators to the rotational motion of the flapping wings. This was realized with a spherical four-bar mechanism in the dual actuator bee design [40]. However, construction of the dual actuator bee transmission required a delicate manual folding and assembly procedure that was vulnerable to human error. It was also not clear that a spherical four-bar was needed, given the very limited bimorph actuator tip rotation; the total rotational deflection of the actuator tips is $<5^\circ$ and the lengthwise tip displacement is negligible (<7 μm). Thus, motivated by the difficulty of the manual folding procedure, we now rely on the layered, pop-up manufacturing method from [50] to produce the four-bar mechanism; this outputs a fully assembled transmission as a 5 rigid-layer, laminated structure with no manual assembly steps. Figure 3.4B illustrates the operation and construction of the transmission linkage. We have empirically found that this planar four-bar mechanism can perform its motion-conversion role without noticeably detrimenting the system dynamics. The off-axis compliance of the flexure hinges in the mechanism is able to absorb the twist angle from the slight rotations of the actuator tips. As described in Section 3.1.2, the transmission ratio remains the same as that of the dual actuator bee.

Similar to the dual actuator bee, the wings are attached to the transmissions through an elastically-deforming, passive rotation hinge in series, which provides the unactuated wing pitch degree-of-freedom. Wing pitching motion is passively modulated by the interaction of aerodynamic forces with the wing's inertia and elastic hinge stiffness. The passive rotation hinge is shown in Figure 3.4A. They are fabricated separately from the transmissions and wings to allow for interchangeability of parts and to support experimentation of wing mechanics.

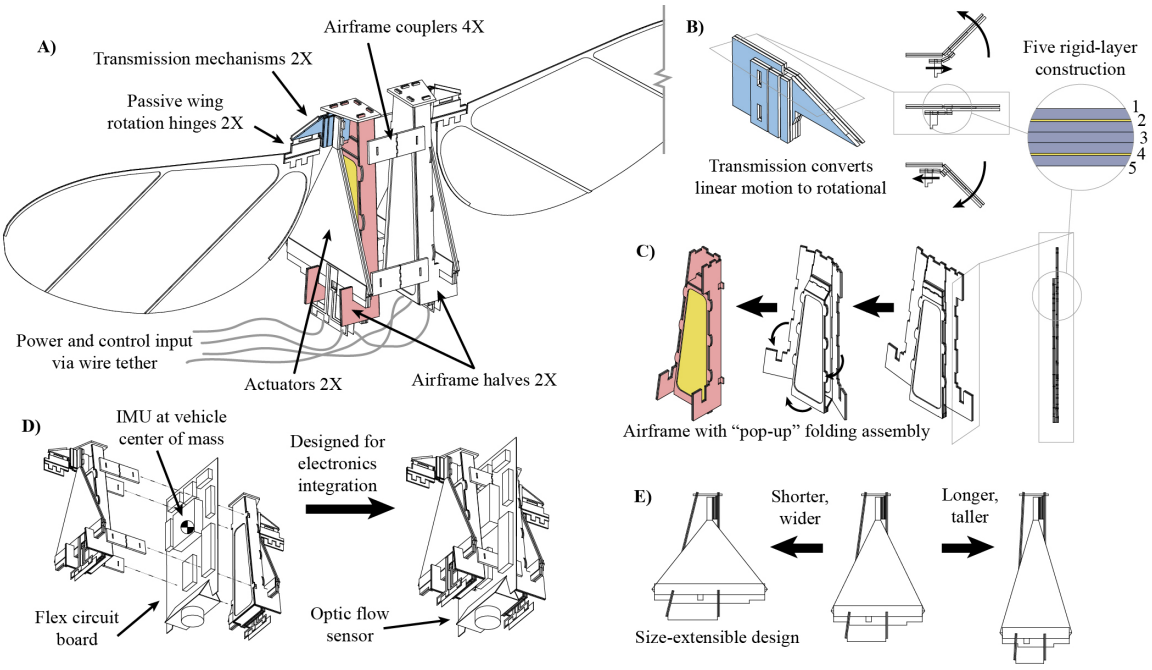

Figure 3.4: Construction details for the robotic flying insect. A) Assembly of components that make up the vehicle. B) The transmission converts the nominally linear actuator tip motion to a rotational flapping motion. It is constructed with laminated layers of rigid carbon fiber composite and flexible polyimide film and consists of five rigid layers. C) The airframe is a rectangular thin-walled tube structure, designed for efficient bending and torsional resistance. Similarly with the transmission, it consists of five rigid layers of carbon fiber composite and can be fabricated simultaneously with the transmission. The design is a pop-up structure for ease of assembly. Polyimide film membrane (colored yellow) stretches across the broad faces—a semi-monocoque airframe. D) Extensibility for electronic integration. The electronic components will populate a flex circuit board that resides in the central plane of the vehicle, establishing a straightforward method for packaging the components and achieving a balanced mass distribution in the vehicle. The IMU can be designed to coincide with the vehicle's center of mass. E) Extensibility for scaling optimizations. The airframe dimensions can be easily modified to accomodate any actuator size around this scale regime.

3.2.4 Airframe

The airframe is the vehicle's mechanical ground structure. It must rigidly ground the actuators and transmissions and resist bend- and twist-loading with minimal deformation, while also remaining lightweight. To address these design constraints, we use a hollow beam construction to increase structural efficiency. The materials used are carbon fiber and Kapton polyimide film. This composite structure is constructed using the pop-up manufacturing method [50] and can also be produced as a 5 rigid-layer laminate, simultaneously with the transmissions.

As the BigBee is explicitly designed for electronics integration, the airframe is designed as two halves with the hull space in between to house the electronics payload. Each half consists of an airframe, actuator, transmission, and wing, and the two halves are mirror images of each other. These two halves are rigidly coupled together with additional coupler beams.

The design must be extensible for electronics integration, based on known placement needs for certain electronic components. Some electronic components require specific orientations and placement on the vehicle structure, as described in Table 3.1. In particular, the IMU benefits from being placed at the vehicle's center of mass to reduce translational vibration [30]. To account for a range of possible component placements, simplify the component packaging problem, and reduce structural mass, we envision placing all electronic components on a single, planar flex circuit. This flex circuit resides in the midplane of the vehicle. Knowing the vehicle structure's center of mass and the mass distribution of the populated flex circuit, we can design the flex circuit such that the IMU coincides with the center mass of the fully assembled vehicle. Figure 3.4D illustrates this concept.

The airframe secures the actuator base at two points. This simple mounting scheme and the design of the airframe can be easily adjusted to support a range of

actuator sizes (see Figure 3.4E).

3.3 Results

We were able to perform a controlled hovering flight with a 115 mg dummy payload onboard. We use the experimental setup presented in Chapter 2, which relies on an array of external motion tracking cameras (Vicon, Oxford, UK) to observe the vehicle's position and attitude in flight. This real time tracking is used with a closed-loop flight controller implemented on an offboard desktop computer and adjusted for the new vehicle's properties, to calculate appropriate control inputs for specified flight behavior. Power and control signals are fed to the vehicle through a wire tether. This wire tether has been shown to have a negligible effect on the flight dynamics of the vehicle [31].

The BigBee was able to lift off and maintain a stationary hover about a setpoint with minimal deviations in position and attitude, thus achieving the design goal of 105 mg payload capacity. The natural frequency of the flapping mechanism was experimentally determined to be 70 Hz—within the predicted range from Section 3.1.2. Using a custom-built capacitive force sensor, we measured a maximum thrust force of 450 mg. The properties of the completed vehicle are summarized in Table 3.2. An image of the hovering flight is shown in Figure 3.5.

3.4 Conclusion

The controlled flight demonstration confirms that the BigBee can be control autonomous, based on the mass estimates of the required electronic components. Our measured maximum thrust force exceeds what is required to lift and control the vehicle. We consider these results to be preliminary. More characterization of the vehicle

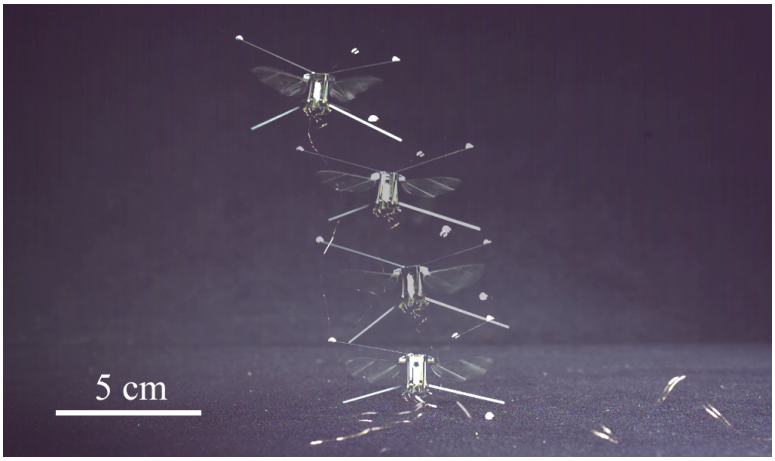

Figure 3.5: Stationary hovering flight of the 265 mg robot with a 115 mg payload—380 mg total. The robot hovered 10 cm above the ground for 4 seconds. Strobed positions of the flight ascent are shown.

design is required, including stress testing for the true maximum thrust force.

Our current vehicle fabrication methods are adequately repeatable though assembly errors and variability are still introduced. This is inconvenient, as the flight controller gains need to be specifically tuned for individual vehicles. Alignment fixtures and additional pop-up, auto-aligning design features may enable more repeatable assembly. This topic is further investigated in Chapter 5. Mechanisms for mechanical trimming could be implemented in the vehicle design itself. Further improvements to the mechanical design include refined wing design and more systematic airframe structural design.

In Table 3.2, we see that the total unloaded robot mass and actuator mass fraction was greater than the scaling target. This may indicate that our actuators are oversized for the target payload capacity and could account for the greater-than-predicted thrust forces. The larger thrust force is also likely attributed to the change in wing shape from the dual actuator bee. More experiments can be performed to isolate the effects of these factors.

Modeling uncertainty likely exists in the system dynamics relation in Eq.3.6. The

wing inertia relation in Eq.3.5 does not account for added mass contribution from the acceleration of surrounding air. This is a significant inertial component [21] but not straightforward to introduce into the scaling heuristic. Our heuristic also ignores aerodynamic damping because of the difficulty in assigning a fixed damping coefficient for constantly accelerating flapping-wings. The system dynamics study in [26] highlighted the use of the damped resonant frequency for better predicting system behavior. Chapter 4 will present efforts to remove some of these modeling uncertainties.

Nevertheless, experiments have verified that the aerodynamic modeling based on the quasi-steady blade element method can robustly capture scaling trends [57, 14]. This analysis is further simplified by maintaining previously-verified wing kinematics. Thus, the scaling heuristic relies on the aerodynamic analysis for vehicle scaling while the natural frequency analysis provides an indication of how the system behavior would change at larger scales. A full system optimization of the vehicle system would include more detailed modeling and scaling trends derived from first-principles in order to prescribe an optimized vehicle design.

At conception, this vehicle was intended for electronics integration, and this has significantly influenced the structural design. The payload capacity as-is provides utility for the realization of control autonomy in insect-scale flying robots. We have demonstrated how the established dual actuator bee vehicle design can be successfully scaled and fabricated using our current methods. A more-developed modeling and optimization effort can further refine the design and will leave the integration of an onboard power source as the last major research hurdle toward control and power autonomous operation of robotic flying insects.

Chapter 4

Vehicle sizing for power autonomy

Our initial effort to scale the dual actuator bee design and attain greater payload capacity has resulted in a flightworthy vehicle with enough thrust force to support control autonomy. This vehicle—referred to as the BigBee—utilized a simple scaling heuristic for FWMAVs and is shown in Figure 4.1. BigBee demonstrated controllable flight when fully loaded with a dummy payload and provides crucial information as a working vehicle design in facilitating vehicle sizing and design optimization. Here, we present a vehicle sizing procedure that relies on specifications from BigBee to improve our initial estimates of the vehicle parameters and refine our modeling predictions. We prescribe the design of an insect-scale FWMAV that will enable control and power autonomy.

4.1 An iterative approach to vehicle sizing

In scaling FWMAVs, we look to aircraft design processes for inspiration. Aircraft design processes rely on the use of data and specifications derived from previous vehicle designs [48]. Many decades of developments and best practices, along with many classes of aircraft, exist for design reference. In comparison, data from existing insect-scale FWMAVs is sparse. Despite this, previous studies exist on system modeling and design optimization of insect-scale FWMAVs. Karpelson presented a

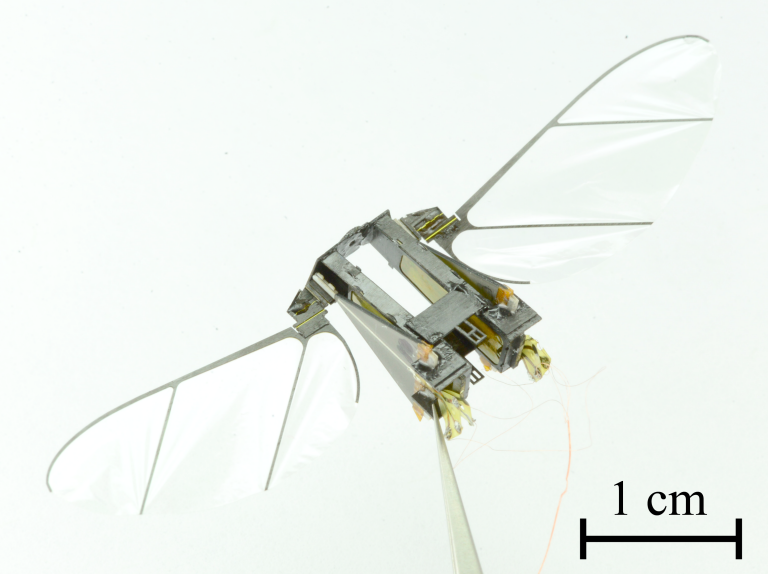

Figure 4.1: The BigBee vehicle design has sufficient payload capacity to support electronics integration for control autonomy. However, the design needs to be optimized to enable power autonomy.

system-level analysis that leveraged early models of vehicle components, with a focus on flight energetics and power autonomy [36]. The study included the integration of mechanical and electrical subsystems and illustrated the feasibility of creating a power autonomous vehicle. Whitney presented a conceptual design analysis for sizing FWMAVs and derived scaling relationships between key vehicle parameters, based solely on approximate models for the aerodynamics and system dynamics [58]. The study highlighted the key parameters that affect flight performance, investigating flight endurance, speed, and range. These studies avoid a practical vehicle design prescription; only conceptual design feasibility is presented.

The system modeling and vehicle sizing procedure presented here incorporates the latest design and manufacturing developments. In particular, the PC-MEMS fabrication methodology enables unprecedented precision in the fabrication of the vehicle's mechanical components [50]. Actuators can be produced more reliably and with improved performance. This has enabled more accurate models of the actuation

mechanics [34]. The culmination of these developments has resulted in repeatable, practical flight demonstrations of insect-scale FWMAVs, as described in Chapters 2 and 3. Access to existing, working vehicles distinguishes this vehicle sizing study from previous efforts; by integrating established, functional design specifications, this study is closer to prescribing a practical vehicle design than any previous effort. Once a working design is constructed and characterized, its specifications can be used to improve modeling accuracy, and the sizing procedure iteratively approaches a vehicle design that best meets the performance requirements.

This experimental approach is taken instead of developing a detailed, full vehicle system model because of the many uncertainties in the system modeling; in particular, the aerodynamics of flapping-wing flight are still not well-understood and difficult to model precisely. The usual aerodynamic treatment for flapping-wing flight involves the blade-element method for aerodynamic force calculation, used in propeller blade design analysis [20]. The blade-element method, which calculates aerodynamic forces by integrating local pressure conditions over the whole wing, ignores spanwise flow components and any time-dependent effects. The accuracy of this approximation relies significantly on aerodynamic force coefficients, which are heavily dependent on wing design and scale. Frequently, this is determined by fitting the aerodynamic model to experiments [15]. Wing design for flapping wing flight is an active area of research, encompassing wing structural properties and wing shape. Biological studies have observed the wings of insects and their multitude of shapes, sizes, and properties [42, 9, 10, 11]. However, functional relationships between the various wing design parameters and aerodynamic force production have not been fully characterized. Aerodynamic force is also closely related to the wing kinematics. Among other modeling uncertainties discussed below, the accuracy of the aerodynamic force model for flapping-wings significantly affects the system dynamics model and is essential to

the vehicle sizing procedure.

4.2 Payload estimate

Our vehicle sizing procedure is explicitly directed toward achieving power autonomy. As the starting point, we will determine the maximum required thrust force from the vehicle in order to achieve the desired flight performance. This initial estimate for the thrust force will be maintained for the entire procedure.

The sizing procedure relies significantly on the vehicle design and operating characteristics of BigBee. BigBee was designed to provide control autonomy and approaches the scale of a power autonomous vehicle. We will use BigBee's mass characteristics as an initial estimate for the component masses in the final vehicle design. The actuator and battery are likely to dominate the overall vehicle mass. BigBee provides a initial estimate of the actuator mass, listed in Table 4.1. Our initial estimate of battery mass will simply equate actuator mass, as previous modeling results have prescribed a battery mass similar to the actuator mass for maximizing flight endurance [58]. Our estimated values are then 265 mg for the unloaded vehicle mass (derived from BigBee properties), 100 mg for the electronics payload (see Chapter 3), and approximately 200 mg for the battery mass. We will overestimate the total vehicle mass to account for modeling uncertainty, giving a final target mass of 600 mg. Thus, the thrust target for the power-autonomous vehicle is 600 mg, or 5.89 mN.

4.3 Aerodynamic modeling

The aerodynamic force model for flapping-wing flight depends on wing kinematics and wing design. Past wing designs have been shown to provide sufficient aerodynamic performance [61, 14]. We fix the wing shape in the following analysis to match that

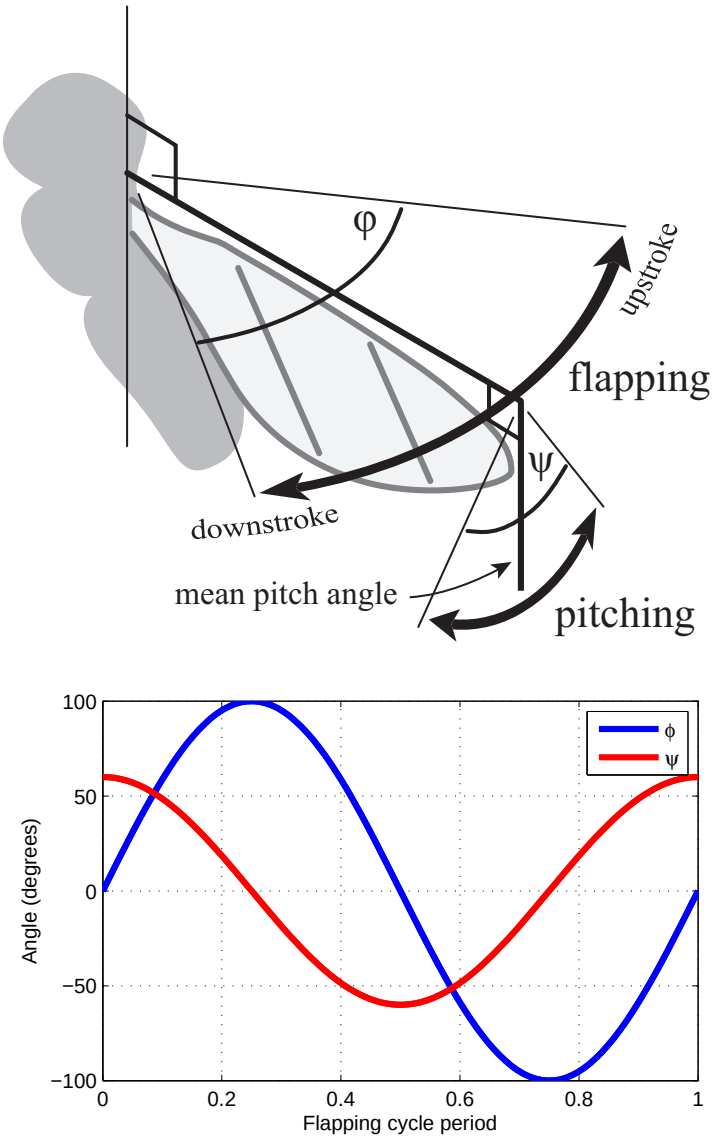

Figure 4.2: Key flapping-wing kinematic angles are labeled. Flapping stroke angle is ϕ and wing pitch angle is ψ. Also shown are the ideal, sinusoidal wing kinematics, with the 90° phase offset between ϕ and ψ, used in this analysis.

of the BigBee. This fixes the wing's aspect ratio, leading edge and trailing edge shape profiles, as well as the radial moments of area. We parameterize the wing size solely with the wing length variable R, which will uniformly scale the wing profile area.

Proper wing kinematics are critical to effective force generation. Controlling the wing kinematics is complicated by the use of an underactuated wing drive with passive rotation hinges. The aerodynamic force generation is sensitive to the phasing between flapping and pitching motion and to the time evolution of the wing angle of attack over the stroke cycle. Tuning the stiffness of the passive rotation hinge will simultaneously alter both the flapping amplitude and pitching dynamics. The hinge must be compliant enough to reach the desired maximum hinge pitch angle, but stiff enough to maintain proper phasing between pitching and flapping trajectories. Proper phasing is critical to achieving high thrust force [14].

To simplify the modeling, we use ideal wing kinematics that reflect the kinematics observed in BigBee. From results of BigBee, this entails a 100° wing stroke amplitude ϕ_{max}, peak-to-peak, and a 60° wing pitch angle ψ_{max} at the mid-stroke position where maximum wing velocity occurs during the stroke cycle. We assume the flapping and pitching dynamics are sinusoidal with a 90° phase offset. Figure 4.2 illustrates these wing kinematics.

With the known wing kinematics and wing design, we can estimate the aerodynamic forces generated by the wing using the blade-element method. This is a quasi-steady analysis that has been shown to capture the scaling relations between wing design and operating parameters and the resultant aerodynamic forces [57]. We make use of characterization results of the BigBee to inform our aerodynamic model, as the BigBee flapping wing system is the approximate scale of a power autonomous vehicle design. The model is fitted to force measurement data from BigBee with a fitting coefficient. Equation 4.1 describes the form of the aerodynamic model used in

the force calculations:

$$F_{aero} = \frac{\gamma * 1/2 \rho \dot{\phi}^2 * C_{aero} * S_A(R)}{T_{flap}} \tag{4.1}$$

where F_{aero} is the time-averaged aerodynamic force calculated over the flapping period T_{flap}, ρ is the density of air, $\dot{\phi}$ is flapping angular velocity, C_{aero} is the aerodynamic force coefficient (lift or drag) based on previous studies of flapping wing aerodynamics [15], and S_A is the wing profile area term than encompasses the specific details of the wing design and is a function of wing length R. γ is the fitting parameter used to fit the model to the BigBee experimental force measurements.

With a maximum thrust target, a fixed wing design, prescribed wing kinematics, and experimentally obtained aerodynamic force coefficients from a comparably-sized vehicle, we can calculate the aerodynamic forces over the space of two key wing system parameters: wing length R and flapping frequency f. The analysis range for these parameters are chosen based on intuition about construction feasibility around the BigBee operating point. Figure 4.3 illustrates this analysis step. From this analysis, we obtain a set of possible vehicle wing length and flapping frequency (R, f) pairs that can generate the target thrust force. We restrict our sizing analysis to this set of parameter pairs.

We can also observe how the Reynolds number of the vehicle scales with the parameter space, using the following equation:

$$Re = \frac{\bar{u} \cdot \bar{c}}{\nu} \tag{4.2}$$

where $\bar{u}$ is the mean translational velocity of the wing tip, $\bar{c}$ is the mean chord length of the wing, and ν is the kinematic viscosity of air. The mean translational velocity is $\bar{u} = 2\Phi f R$ where Φ is the wing stroke amplitude, fixed at 100° in this analysis,

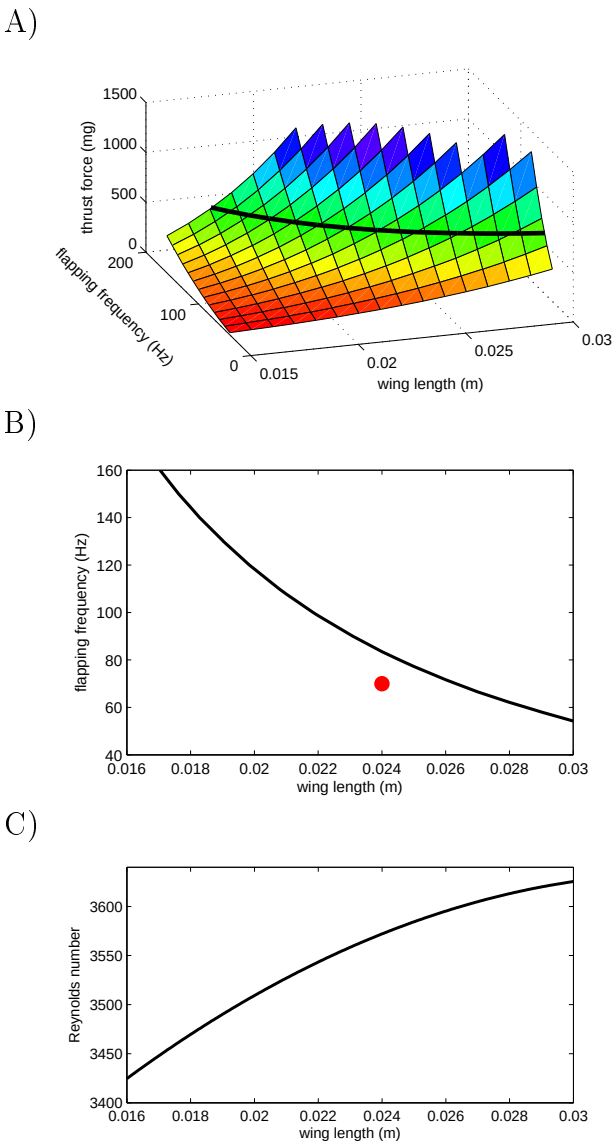

Figure 4.3: A) Thrust force generated by the flapping wing drives, calculated over the space of wing lengths and flapping frequencies in a vehicle design range around the BigBee operating point. The black curve that corresponds to 600 mg—the thrust target—defines a series of possible wing length-flapping frequency pairs (R, f) for the vehicle design. B) Wing length and flapping frequency (R, f) are coupled in this analysis. The red dot indicates the design point of BigBee. C) Reynolds number increases with wing length as an inverse-quadratic function.

and the mean chord length for the BigBee wing shape is $\bar{c} = \frac{1}{3}R$. In Figure 4.3C, we note that despite the decreasing flapping frequency with wing length, the Reynolds number increases with wing length. Values are in the range of 3400 to 3600. The Reynolds number for BigBee was calculated to be 3000 and not shown in the plot range.

4.4 System model

We constrain our sizing analysis to the set of (R, f) pairs which define wing kinematics capable of generating the target thrust. The system will be designed to ensure that the wing kinematics can be achieved, while maximizing the system's power efficiency. In particular, the piezoelectric actuators must be appropriately sized. Actuator sizing contains tradeoffs that affect the system dynamics. Large actuators will increase force output but also increase system stiffness. The actuators can be optimized for energy density independent of the whole vehicle, but optimizing for vehicle electrical-to-mechanical power efficiency requires incorporating the wing drives and the electronic subsystems into the analysis. Seen from the actuator, the vehicle system can be modeled as a harmonic oscillator, with stiffness, damping, and inertia. Thus, we can use a one-dimensional, lumped parameter linear system model, similar to previous modeling studies [26, 58].

The transmission ratio is an important system variable that affects the mapping of forces from the wings to the actuator. In this analysis, we also iterate over a range of fabrication-feasible transmission ratios. For this analysis, the transmission can be modeled as a simple lever mechanism, with an effort arm length L_3 and output arm length R_{cop} which corresponds to the wing's aerodynamic center of pressure—a

function of wing length R. The transmission ratio is defined as:

$$T = \frac{R_{cop}}{L_3} \tag{4.3}$$

4.4.1 Damping

Damping in the system is dominated by the aerodynamic drag force on the wings. Aerodynamic drag force is calculated in the same manner as the lift force, with a change in coefficient. Damping also exists in the flexure hinges of the transmission, but it is negligible compared to the aerodynamic drag on the wings; its force contribution is estimated to be two orders of magnitude less than the aerodynamic drag.

Drag on a flapping wing with a passive rotation hinge is highly dependent on the hinge rotation dynamics. To the first order, wing drag is a function of the instantaneous angle of attack. To simplify the system model for linear system analyses, we linearize about the midstroke position when wing velocity, and thus drag force, is maximum. From our previous aerodynamic modeling, we have prescribed the angle of attack at this point to be 60°. This linearization about the midstroke point has been used in previous system modeling studies [26], though for a smaller prescribed angle of attack (45°). As Figure 4.4 illustrates, the linearized drag prediction consistently underestimates the modeled, nonlinear drag force. To compensate, we add a scaling factor such that the linearized drag force consistently equals or overestimates drag force throughout the stroke cycle. The equivalent, linear damping coefficient in the system is labeled b_{eq}.

4.4.2 Inertia

The inertia of the system is dominated by the wing inertia and the mass of entrained air. From estimates of the BigBee properties, wing inertia as seen by the actuator

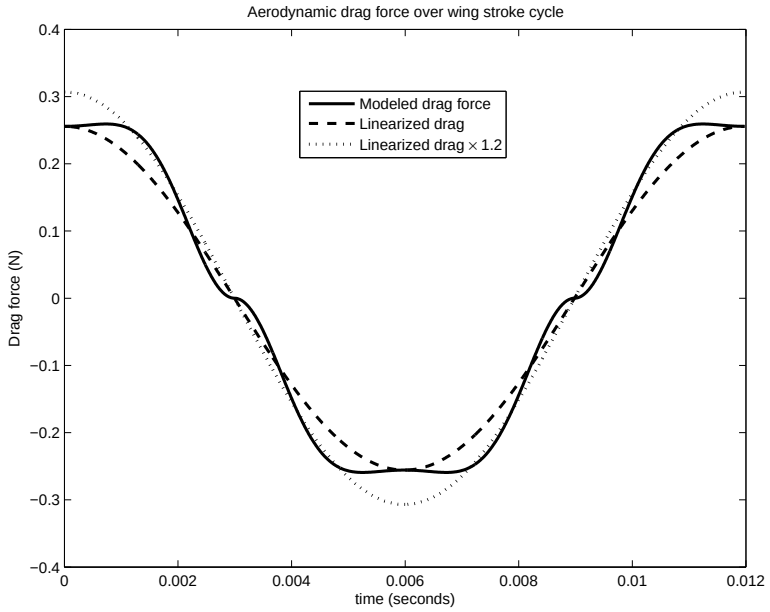

Figure 4.4: Comparing the modeled, nonlinear aerodynamic drag force to the linearized system's drag force, we see a persistent underestimate in the linearized drag force. To compensate, we add a 1.2× factor to ensure the linearized drag force equates or overestimates the nonlinear drag.

is two orders of magnitude greater than the actuator's inertia. The wing design and wing fabrication process both affect the wing's inertia. For a flat plate wing that scales uniformly in the plane, wing inertia scales to the fourth power of the wing length. However, practical fabrication considerations constrain the design to use a minimum spar width for manufacturability and structural strength. Because wing manufacturing for this vehicle scale was stabilized in the development of the BigBee, it is convenient to derive a more accurate scaling relationship for the wing inertia. We use CAD modeling to take into consideration the non-uniform scaling of the wing spars. Including recent changes to wing manufacturing, the wing inertia scales with wing length R to the power of 3.26. The exact expression for wing inertia is:

$$m_{wing} = 0.0163 \cdot R^{3.26} + 4.2052 \tag{4.4}$$

Added mass from accelerating the entrained air around the wing also contributes to the wing inertia component. An approximation for the added mass effect is given in [57]. Its contribution is 25% of the total system inertia as seen by the actuator. The expression for added mass used in this analysis is:

$$m_{am} = \frac{\pi}{4}\rho\bar{c}^2R^2\ddot{\phi}\hat{I}_{zz,am} \tag{4.5}$$

where $\bar{c}$ is the mean wing chord length, $\ddot{\phi}$ is the flapping angular acceleration, and $\hat{I}_{zz,am}$ is the non-dimensional wing inertia and a function of wing geometry. Added mass is a function of angular acceleration and changes over the wing stroke cycle. Its maximum occurs at the ends of the wing stroke when angular acceleration is greatest. We use this maximum value in our calculations of the linear system inertia. The equivalent, linear inertia coefficient of the system is then:

$$m_{eq} = m_{wing} + max\left(m_{am}\right) \tag{4.6}$$

4.4.3 Stiffness

The lumped system stiffness k_{eq} consists of the transmission and actuator stiffness contributions:

$$k_{eq} = k_{trans} + k_{act} \tag{4.7}$$

Transmission stiffness k_{trans} consists of the flexure hinge joint stiffnesses, in addition to stiffness resulting from off-axis deformations of the flexure hinges. Off-axis deformation of the flexure joints is caused by the inherent kinematic mismatch between the transmission—a planar linkage—and the out-of-plane rotational displacement of the actuators. This design choice eliminates an additional slider crank linkage and reduces mechanical complexity. However, it also introduces significant modeling dif-

ficulty due to the large deformations and coupling of the deformation modes. The stiffness resulting from off-axis deformations accounts for a substantial portion of the transmission stiffness; in the worst case, only 25% of the stiffness can be attributed to rotational bending stiffness calculated from simple beam theory. Thus, we experimentally measure this stiffness in a representative BigBee and use this nominally fixed value in our vehicle sizing analysis.

This approximation of the transmission stiffness is valid as long as the transmission design does not change. Varying the transmission ratio will likely have an effect on the stiffness, but without a mechanics model of the transmission, it is difficult to predict the relationship. More experiments need to be performed to determine the relationship between the transmission ratio and stiffness, for this particular transmission design.

The actuator stiffness k_{act} is a function of actuator geometry and can be expressed as the ratio of the actuator's blocked force F_b to free displacement δ: $k_{act} = F_b/\delta$. To determine the actuator stiffness, we can assume the system is operating at a frequency ω_M where the system's amplification factor M is greatest [47] (expression is shown in Equation 4.8). This can effectively be considered the resonant frequency of the system. If the prescribed wing kinematics are achieved at this frequency, the required force to drive the system is minimized, due to the cancellation of inertial and elastic forces, and the actuator can be minimally-sized. Coinciding the flapping frequency f with the resonant frequency $\omega_M = 2\pi f$, and with known system inertia m_{eq}, system damping b_{eq}, and transmission stiffness k_{trans}, we can determine the actuator stiffness k_{act}:

$$\zeta = \frac{b_{eq}}{2\sqrt{m_{eq}k_{eq}}}, \omega_n = \sqrt{\frac{k_{eq}}{m_{eq}}}$$
$$\omega_M = \omega_n\sqrt{1-2\zeta^2} \tag{4.8}$$

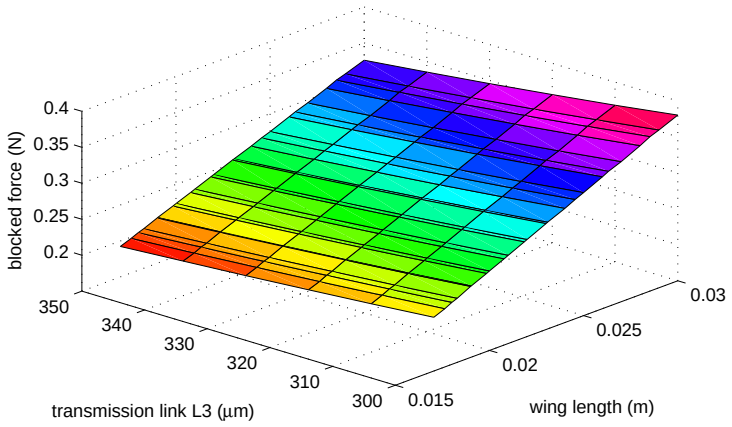

Figure 4.5: Blocked force calculated over the parameter space of wing length and transmission geometry.

where ζ is the damping ratio and ω_n is the natural frequency. Substituting Equation 4.7 into 4.8 and solving for k_{act}, we obtain:

$$k_{act} = m_{eq}\left(w_M^2 + \frac{b_{eq}^2}{2m_{eq}^2}\right) - k_{trans} \tag{4.9}$$

4.5 Actuator sizing

With the approximate system model linearized about the position of maximum stroke velocity, as described in Section 4.4.1, we can sum the inertial, damping, and spring force components to determine the force magnitude required from the actuator. We can calculate the blocked force required from the actuator, over the set of (R, f) pairs and over a range of transmission geometries L_3, by using Equation 4.10, which describes the amplitude of a harmonic input forcing function to a harmonic oscillator [47]:

$$F_b = \sqrt{\left(A\left(k_{eq} - m_{eq}\cdot\omega^2\right)\right)^2 + \left(A\cdot b_{eq}\cdot\omega\right)^2} \tag{4.10}$$

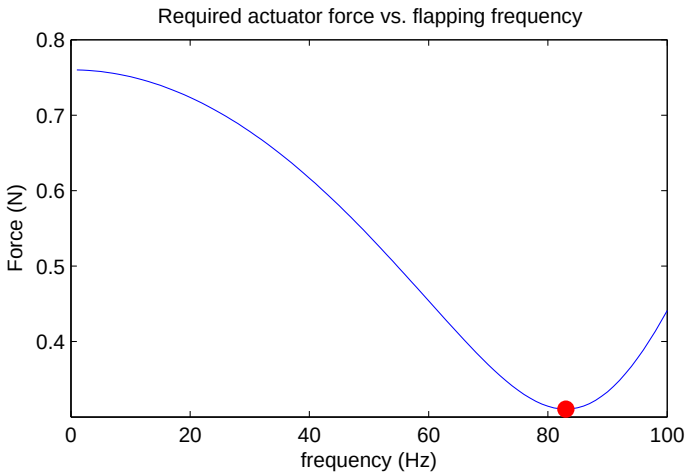

Figure 4.6: For a particular design point ($R = 24$ mm, $f = 83$ Hz), the force required from the actuator to maintain the prescribed wing kinematics increases as flapping frequency deviates from the resonant frequency ω_M, as calculated from Equation 4.10. The red dot indicates the resonant frequency ω_M of the system.

A is the displacement of the actuator necessary for the system to achieve the prescribed wing kinematics. k_{eq}, m_{eq}, and b_{eq} are the equivalent stiffness, inertia, and damping terms, respectively, as seen by the actuator output. Figure 4.5 shows the blocked force calculated over the prescribed parameter space. The system stiffness assumes the system is operating at the resonant frequency ω_M , at which point the actuator force can be minimized. Deviations from ω_M will require more force from the actuator to maintain the desired stroke amplitude. Figure 4.6 illustrates how the blocked force requirement increases as the flapping frequency deviates from ω_M .

We can also determine the free displacement of the actuator δ needed to ensure the actuator stiffness matches the system model estimate, using the relation $k_{act} = F_b/\delta$. This free displacement is compared to the actuator displacement A required to generate the prescribed wing kinematics. Actuator performance is constrained by the strain limit of the piezoelectric ceramic material. Experiments have indicated that the strain limit is reached slightly beyond the actuator's free displacement. However, as the strain limit is approached, the fatigue life of the actuator decreases. For now, we

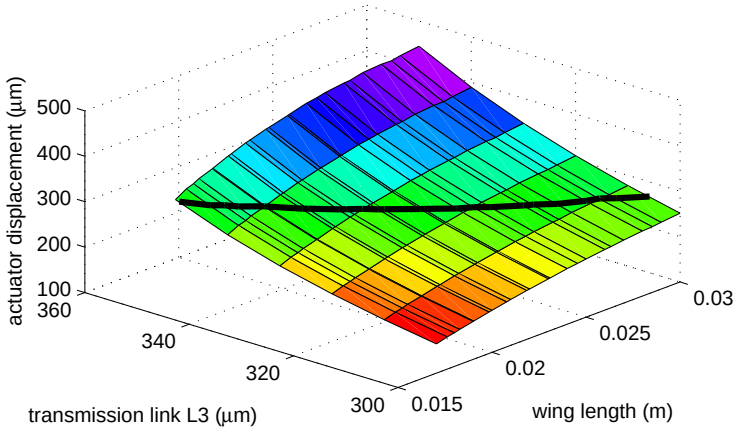

Figure 4.7: Free displacement δ of the actuator optimized for energy-density, calculated over the parameter space of wing length and transmission geometry. The solid black line indicates the constraint where δ matches A, the actuator displacement required to achieve the prescribed wing kinematics. It serves to indicate a constraint on the design space: δ values below this line indicate that the prescribed wing kinematics will deflect the actuator beyond its δ, possibly reducing actuator lifetime.

will remain conservative and assume the prescribed actuator displacement matches the actuator's free displacement, illustrated in Figure 4.7. This defines a constraint on the parameter space.

With the blocked force and the free displacement, we utilize a mechanics model and optimization routine to optimize the actuator geometry for maximum energy density, presented in [60]. Specific design constraints are present for this vehicle sizing analysis: The vehicle design does not make use of the actuator tip extensions for the purpose of improving energy density, and the operating voltage signal of the actuators is set to be 230V. As described in Chapter 3, the actuators are constrained by the piezoelectric ceramic's mechanical strain limits, which dictate a 300V electric field maximum. Driving with 230V signal amplitudes allows 35V voltage margins available for vehicle pitch torque control. With these modeling constraints, the blocked force and free displacement values fully define an actuator geometry, which in turn allows us to estimate the actuator mass, illustrated in Figure 4.8.

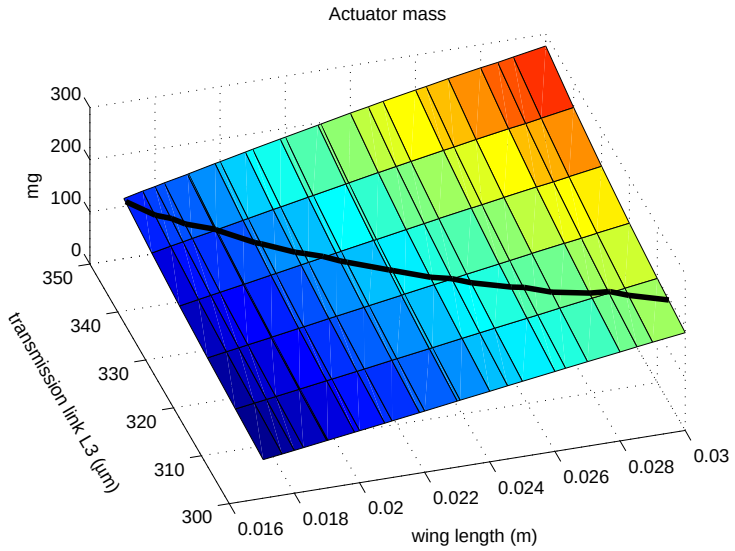

Figure 4.8: Estimated actuator mass over the parameter space. The solid black line indicates bound in the optimization space established by the actuator strain limit, as illustrated in Figure 4.7.

4.6 Power efficiency

The mechanical power requirement of the actuators, for a prescribed operating point, can be estimated as:

$$P_{mech} = \frac{1}{2} F_b \delta \omega \tag{4.11}$$

The electrical power requirements have also been modeled, from recent developments in custom power electronics [39]. The model encompasses the effects of the boost converter, wing driver circuit, actuator power, and energy recovery schemes and is a refinement of the earlier work on milligram-scale power electronics from [35]. The salient scaling relationship for the electrical power consumption can be described as:

$$P_{elec} = \frac{1}{2} C V^2 f \tag{4.12}$$

where C is the capacitance of one PZT plate, f is the operating frequency, and V is

the maximum voltage applied to the actuator.

As an initial estimate, we use the measured capacitance of the BigBee actuators, which is 13 nF for a 42 mm^2 actuator profile area. We linearly scale with area around this data point to obtain good estimates of the capacitance for near-sized actuators. Figure 4.9 illustrates the trends in P_{mech}, P_{elec}, and power efficiency P_{mech}/P_{elec} over the range of (R, f) pairs and transmission ratios. The plot indicates that power efficiency improves with smaller wings and higher flapping frequencies. Equation 4.12 indicates that electrical power consumption scales proportionally with frequency and capacitance. Our analysis indicates that for the set of (R, f) pairs which achieve the target thrust output, the actuator capacitance scales more rapidly than the flapping frequency and dominates the power consumption calculations. Thus, though smaller wings need to flap faster, increasing mechanical power consumption, smaller actuators have lower capacitance and lower overall electrical power consumption rates.

4.7 Flight endurance

With our power efficiency estimates, we can speculate on the flight time of the vehicle design if we have an approximate model for battery energy capacity as a function of mass and discharge rates. Potential battery technologies with high energy densities are in active development. Candidate technologies include micro fuel cells and novel-structured lithium-ion batteries [24, 51]. However, for near-term integration of a battery for power autonomy, we can use commercially-available lithium-ion batteries which are available in sizes small enough to be integrated on the vehicle. Battery supplier `Powerstream.com` carries rechargeable, ultra low-weight lithium-ion batteries, with the smallest weighing 330 mg at a capacity of 8 mAh. We can use this example data point to create an approximate battery capacity scaling model that fits near the

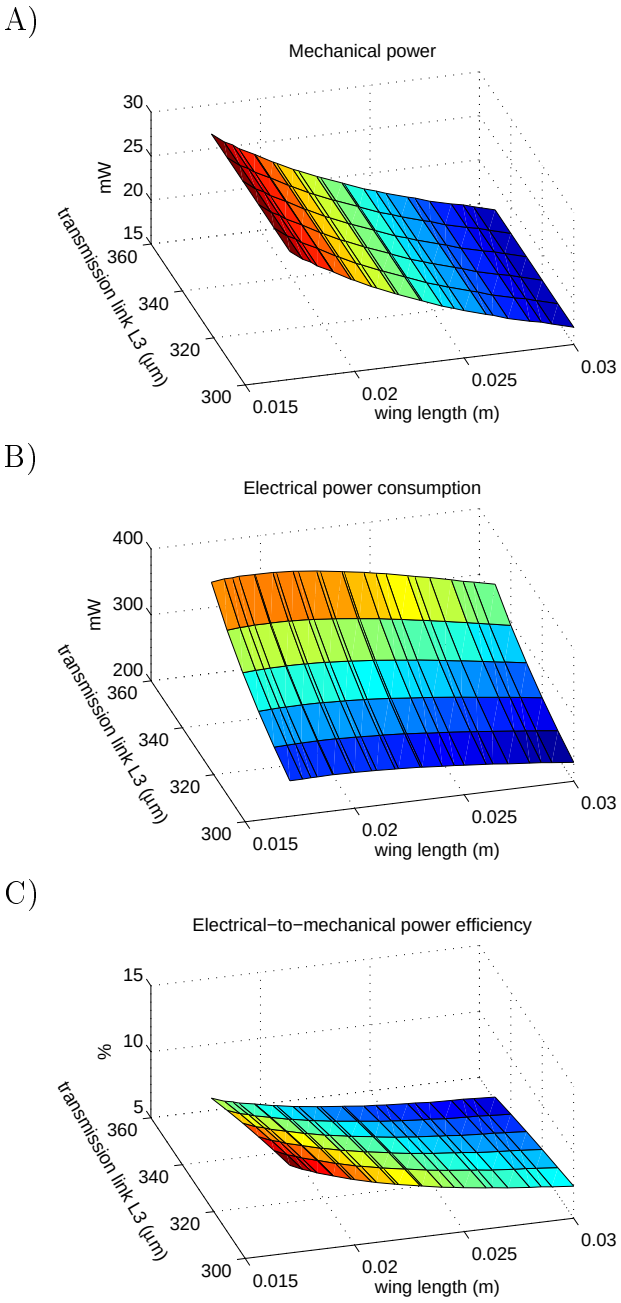

Figure 4.9: A) Mechanical and B) electrical power requirements over the parameter space. C) Electrical-to-mechanical efficiency of the vehicle.

final vehicle design scale. The model is complicated by the capacity derating property inherent to battery chemistries. At higher discharge rates, battery capacity decreases. Based on data points from supplier spec sheets, we approximate the derating trend as the inverse of the C-rate [46]:

$$E_{batt} = effective\ energy\ capacity = \frac{rated\ capacity}{C_{rate}} \tag{4.13}$$

For the specific battery chosen in the final, integrated vehicle, its derating trend must be experimentally verified to obtain a more accurate model.

We can calculate the payload capacity available for the battery by subtracting the actuator mass and structural mass from the target thrust value. With approximations for electrical power requirements, battery capacity, and battery mass m_b, we can calculate flight time t_f as:

$$t_f = \frac{E_{batt}}{\frac{P_{elec}}{V_{batt}}} \tag{4.14}$$

where V_{batt} is the rated voltage of the battery, nominally 3.7V.

The plots indicate a trend of greater power efficiency with smaller, faster flapping wings. Mechanical limits on the actuator provide bounds for the optimization. The actuator strain limits place an upper constraint on actuator deflection, as discussed in Section 4.5. Wing structural limits can provide another constraint, as described below. For our chosen simulation range, which was chosen based on proximity to the BigBee operating point, the estimated flight time is on the order of 10-20 seconds, as shown in Figure 4.10. We consider this to be a very rough estimate, which can be refined once we identify the specific battery technology for integration.

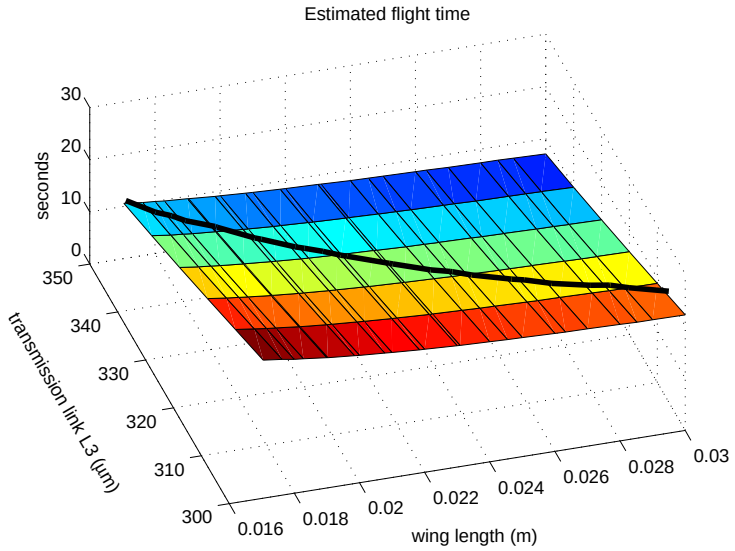

Figure 4.10: Estimated flight time over the parameter space. The solid black line indicates the bound in the optimization space established by the actuator strain limit, as illustrated in Figure 4.7.

4.8 The effect of mechanical limits on wings

The wings also have mechanical limits that constrain the vehicle design space. At a minimum, the wings must withstand the aerodynamic drag loading without mechanical failure. They must also have enough rigidity to maintain the flat plate approximation. The maximum bending moment occurs at the wing base and increases with increasing flapping frequency and wing area. Equation 4.15 is used to estimate the bending moment:

$$M(r) = \int_0^R \frac{1}{2}\rho C_N \dot{\phi}^2 r^2 S_A (r - r')dr' \tag{4.15}$$

$$C_N = C_D \cdot sin\alpha + C_L \cdot cos\alpha \tag{4.16}$$

where r is the radial distance from the wing root and C_N is the aerodynamic normal force coefficient on the wing, as a function of the lift C_L and drag C_D coefficients and angle-of-attack α. The r^3 scaling relation dominates the bending moment calculation

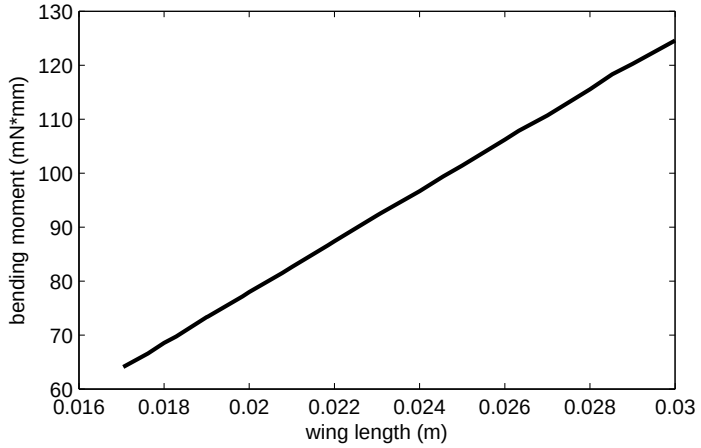

Figure 4.11: Bending moment at the wing root, as calculated from Equation 4.15, for the set of (R, f) pairs in the sizing analysis.

and penalizes larger wings. For the set of (R, f) pairs in this analysis, the bending moment at the wing root is illustrated in Figure 4.11.

Experiments have shown that the wing design and manufacturing methods used in the construction of BigBee have generated sufficiently rigid wings at its particular scale. If the manufacturing methods remains the same, as wings increase in size, the increasing bending moments during operation will gradually compromise the flat plate approximation of the wing.

4.9 Vehicle sizing design prescription and discussion

With a thrust target of 600 mg, the sizing procedure prescribes a vehicle with the specifications listed in Table 4.1. Battery mass is the difference between the thrust target and the sum of the actuator and payload masses and is assumed to consume all remaining payload capacity after electronics and structural payload masses. Note that the wing length value is distinct from that of Table 3.2 because it is measured from wing planform root, not flapping rotation axis. This vehicle design prescription

Table 4.1: Vehicle design prescription for power autonomy.

Vehicle parameter	BigBee value	Power autonomous vehicle value	Units
Wing length	24.1	24	mm
Flapping frequency	70	83.5	Hz
Actuator mass	196	135	mg
Static payload mass (electronics + structural)	170	170	mg
Thrust target	>450	600	mg
Battery mass	>84	295	mg
Vehicle mass without battery	366	305	mg
Actuator length	8.332	8.567	mm
Actuator (base) width	8.606	6.199	mm
Transmission link length L_3	300	300	μm

is presumed to be capable of power autonomy and feasible to construct in the near-term.

It is important to discuss our confidence in this sizing procedure and resulting design prescription. The scaling trends identified in the modeling, particularly for actuator mass (Figure 4.8) and power efficiency (Figure 4.9), indicate that smaller wings flapping faster are more desirable for ensuring greater payload capacity and flight time. Mechanical limits to the actuators constrain the sizing procedure from prescribing ever-smaller wings, indicated in Figure 4.7. This boundary is not a hard constraint and only indicative of decreasing actuator fatigue life. Additional experimental characterization of this failure mode is required to determine the extent beyond this boundary where actuator lifetime is intolerably compromised.

With the boundary cutting across the parameter space, additional constraints are required to identify an optimal design point. We can improve confidence for the design prescription by maintaining BigBee specifications, as the aerodynamic model was fitted to the BigBee wing geometry. We maintain the BigBee wing geometry at 24 mm in length. Large deviations from the BigBee wing geometry would likely

reduce the accuracy of the model, as the model is naive to changes in the unsteady aerodynamic factors and Reynolds number.

We also maintain the BigBee transmission geometry L_3, with a length of 300 μm. Throughout the sizing analysis, we studied the scaling trends with respect to transmission link length L_3. In practice however, this transmission geometry is difficult to precisely and reliably reproduce with current fabrication methods. Also, the transmission stiffness is not modeled and only empirically determined from the BigBee design, limiting its accuracy for much of the design space. Maintaining the transmission geometry L_3 moves the prescribed design off of the constraint boundary defined by actuator mechanical limits (Figure 4.7). If the initial construction of the prescribed design results in actuator failure or failure to achieve the prescribed wing kinematics, we would be compelled to modify the transmission design or the manufacturing methods such that precision adjustment of this transmission geometry is possible.

Our sizing procedure relies on a single operating frequency, derived from a linear systems analysis, where the actuator is specifically designed to drive the system in achieving the prescribed wing kinematics. The linearized system analysis of a similar vehicle morphology was demonstrated to adequately approximate the system's primary resonance to within 5% [26]. However, as illustrated in Figure 4.6, such an error would result in an underpowered actuator for the system loading. The overestimate in the equivalent damping coefficient from Section 4.4.1 may mitigate this risk. Nevertheless, the mechanical system is markedly nonlinear, particularly because of the passive rotation hinge dynamics which in turn affect the aerodynamic drag predictions. A nonlinear, full system model would depend in large part on integrating the full equations of motion for the passive rotation hinge, coupled with the variety of aerodynamic force components that govern the rotation dynamics. Efforts to develop

this model are underway and rely on large experimental data sets for model fitting.

4.10 Conclusion

The vehicle sizing procedure presented here mirrors aircraft design processes in its iterative approach. The BigBee specifications provide accurate estimates for various vehicle component properties, such as the airframe structural mass, transmission stiffness, actuator stiffness and capacitance, as well as wing design, in order to inform the system model. Prescribed wing kinematic specifications, informed by BigBee operation, were paramount in surmounting the uncertainties in the aerodynamic modeling of flapping wing flight. The sizing procedure centers on a defined target thrust that encapsulates the vehicle's performance goal of power autonomy. All other vehicle parameters, such as flapping frequency or wing span, are then incidental. Because the procedure relies on iterating to refine the vehicle and validate the modeling assumptions, more prototypes must be constructed. As of this writing, this effort is underway.

This vehicle design process does not yet integrate considerations on flight control performance. As our understanding and models of FWMAV vehicle design improve, we can transition from simply attaining lift-off and stationary hover to task-specific design optimization, accounting for other metrics such as flight endurance, speed, and maneuverability.

Chapter 5

Mesoscale manufacturing and assembly

At the scale of insects and insect-scale FWMAVs, the challenge of constructing dynamic, mechanical machines has motivated the development of new fabrication and assembly methods. The scale of interest extends from microns to centimeters, known as the "mesoscale." Within this scale regime, it is extremely inefficient and impractical for conventional fabrication and assembly methods to construct mesoscale mechanical structures. Conventional machining technologies such as milling, lathing, or drilling typically have dimensional tolerances on the order of tens microns, too coarse to consistently reproduce designed features of similar scale. Conventional assembly methods require manipulating, aligning, and assembling independently-fabricated components and usually joining them with discrete fasteners. Moving elements must incorporate pin joints, which usually consist of discrete pins aligned into holes. Again, the tolerances of conventional machining make it difficult to ensure low loss and precise, low-backlash joints without meticulous manual efforts to ensure perfect fit of parts. Assembly requires a skilled artisan or very specialized machinery, specifically designed for certain components. In general, conventional fabrication and assembly methods are unsustainable for research and development pace of mesoscale machines.

Micro-Electromechanical Systems (MEMS) fabrication processes are sufficiently

precise but also not ideal for mesoscale machine construction. MEMS processes machine components through etching action and are applicable to a limited library of materials. The compatibility of certain etching processes and materials must be carefully considered and accounted for. Machining feature sizes are excellent, but the processes are time-consuming, typically rely on toxic chemicals and processes, and are not economical for machining geometries beyond millimeters.

In considering solutions to fabrication at the mesoscale for FWMAVs, the properties of flexure hinges are advantageous. A flexure hinge is an elastically-deforming strip of material with localized deformations that can be approximated as occuring along a single axis of rotation. Flexure hinges in general have low backlash and practically no friction losses or need for lubrication. They can be created simply by removing material in a localized region to increase stress concentration and thus localize deformation when under stress. A sheet of material can have multiple flexure hinges simultaneously fabricated. This is similar to creating folds in a sheet of paper by scoring or perforating lines. From a flat sheet, three dimensional structures can be created by folding along flexure hinges, bringing material out of plane. Joints can be fixed or remain dynamic, though they cannot exhibit continuous rotation. Rigid members linked with flexure hinges create a kinematic chain and can be used to create dynamic mechanisms. The use of flexure hinges can be a sufficiently-precise and economical method for mesoscale-FWMAV construction.

5.1 Laminate-based manufacturing

The scale of the FWMAVs we are developing is uneconomical for MEMS processes as well as conventional fabrication and assembly techniques. Instead, we can utilize the planar fabrication of flexure hinges to construct our structures and mechanisms at this scale. In the case of a FWMAV, it is imperative that the structures and

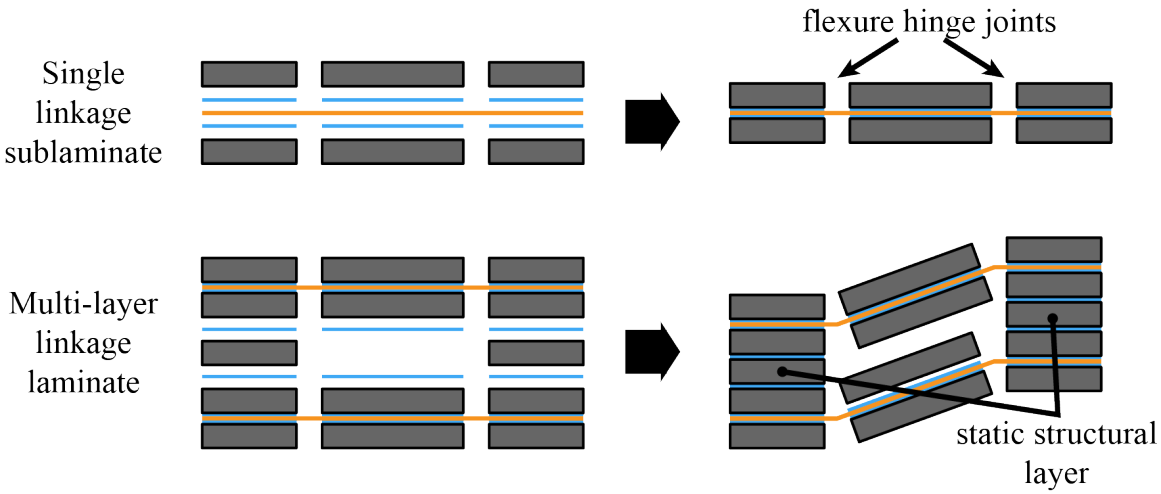

Figure 5.1: Illustration of the PC-MEMS fabrication process. A single linkage sublaminate consists of rigid material layers (grey) adhered to flexible polymer layers (orange) with adhesive (blue). The rigid layers and adhesive are patterned with features to expose the flexible layer in the laminated composite, creating flexure hinge joints. Multi-layer linkage laminates are also possible. Flexure joints locations can be coordinated with other linkage planes to form complex mechanisms. Static structural layers can also be introduced to form geometries by layering.

mechanisms be constructed from very lightweight and stiff materials. The properties of carbon fiber and glass fiber composites become very attractive for constituting the rigid members. At the same time, it is desirable for the mechanisms' dynamic flexure hinges to exhibit large range of motion while also repeatibly, elastically deforming with high fatigue life. Polymers films can meet these requirements. These considerations motivated the development of the Smart Composite Microstructures (SCM) fabrication process, which constructs dynamic flexure hinge mechanisms in planar composite laminates [59]. Layers of rigid material (predominantly carbon fiber composite laminates in FWMAVs) are laser micromachined with slits. Polymer film is sandwiched and laminated in between two rigid material layers. Wherever the slits in the rigid layers expose polymer film, a flexure hinge is created.

The SCM process played an important role in the development of the first flight-worthy FWMAV prototypes. The process was further developed into the PC-MEMS

fabrication methodology, so named because of its inspiration from printed circuit board (PCB) manufacturing techniques [56, 50]. The basic flexure hinge composite laminate of the SCM process can be propogated with more layers to create multi-layered linkage laminates, as illustrated in Figure 5.1. Adhering additional rigid material layers can further reinforce rigid members or build up static structural geometry. The use of additional, flexible material layers can create additional, parallel planes of flexures. Features on each linkage 'sublaminate' can be coordinated with linkage sublaminates above and below it, to construct exceedingly complex flexure hinge mechanisms. Multiple degrees of freedom in the mechanism can be coupled such that the displacement of multiple flexure hinges occur with a single assembly input. This facilitates assembly of complex mechanisms. An illustrative example of the complexity achievable with this design and assembly methodology is shown in Figure 5.2.

This PC-MEMS fabrication process is very amenable to the mechanism scale of interest and the construction materials appropriate for our FWMAVs. The thicknesses of commercially-available material sheets range from a few microns up to a millimeter. Micromachining technologies, such as lithographic chemical etching, laser machining, and stamping are well-developed to handle thin planes of material while accurately reproducing micron-to-millimeter scale feature sizes. Capable sheet adhesives, designed for the PCB industry, can bond a wide assortment of materials. The development of insect-scale mechanisms has benefitted from the development of these composite-laminate fabrication methods. In a demonstration that encapsulates the utility of the PC-MEMS process, an actuated FWMAV prototype with high mechanical complexity was successfully fabricated with the PC-MEMS process, presented in [50], and was designed to be assembled with a single degree of freedom. PC-MEMS has the potential to accelerate the mass-production of complex mechanical devices,

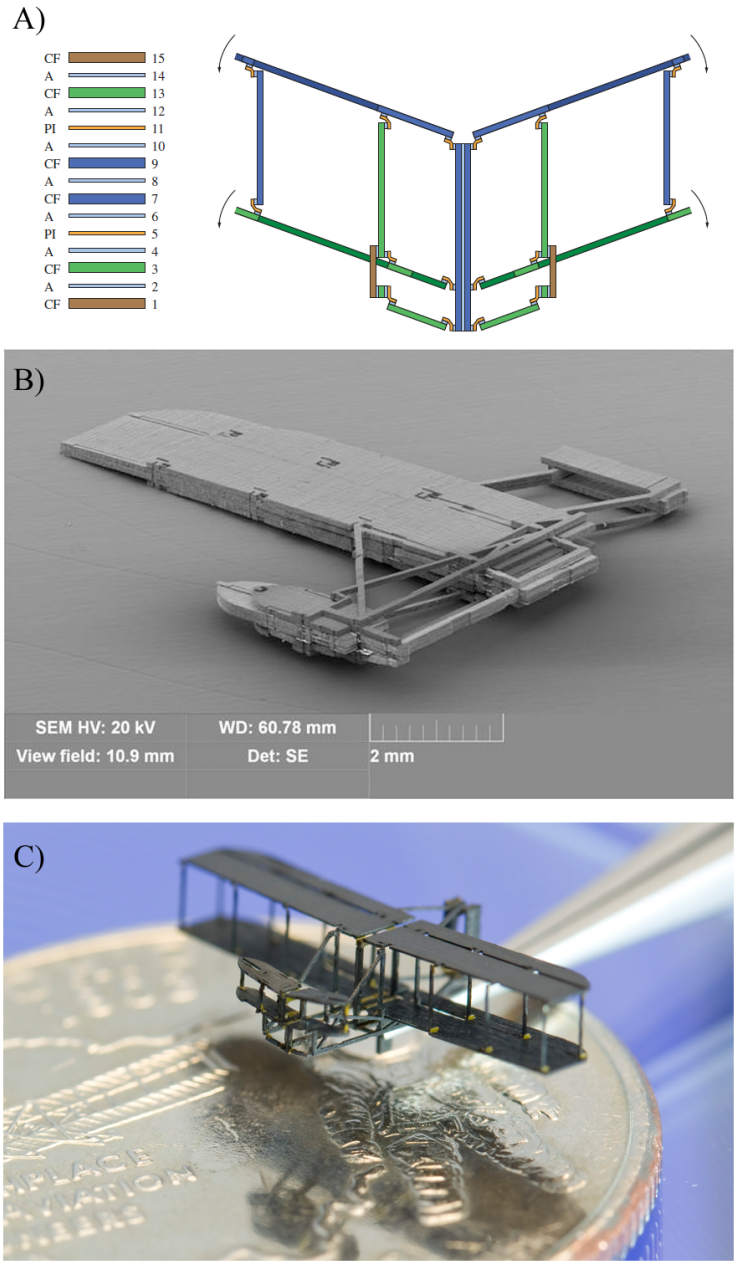

Figure 5.2: A 1:900 scale model of the 1903 Wright Flyer was constructed using the PC-MEMS process. A) Fifteen material layers are used, consisting of carbon fiber laminate (CF), Dupont FR1500 sheet adhesive (A), and polyimide film (PI). The laminated structure consists of a series of four-bar linkages, allowing the Wright Flyer to be assembled by unfolding the structure. B) SEM image of the unopened Wright Flyer laminate. C) A fully assembled Wright Flyer is shown with a US quarter for scale. The final structure has a 14 mm wing span, with 18 vertical struts each with a 100 μm diameter.

with minimal specialized assembly tools, equipment, or other overhead.

5.1.1 Trade-offs

At this early stage in development of the PC-MEMS fabrication methodology, there are trade-offs when compared to conventional construction at the mesoscale. The PC-MEMS process removes post-fabrication assembly overhead, as described above, but adds design and fabrication overhead. Mechanism design with the PC-MEMS methodology is unintuitive and tedious without an algorithmic understanding of the design processes, which could be mediated by computer-assisted design tools [2]. The design complexity can compound quickly with additional linkage sublaminates that need to coordinate with the kinematics and material usage of other sublaminates to avoid mechanical interference in the final structure. Design features are also needed to ensure manufacturability of the laminate structure. Design tools are in development and are gradually reaching a mature state [1].

The PC-MEMS process also introduces challenges in the fabrication phase. Without a developed, semi-automated pipeline for the machining, processing, and handling of materials, such as in the PCB manufacturing industry, constructing a complex laminate with many layers requires significant manual labor on the part of a researcher. Machining (laser machining/etching is common) is mostly automated but handling and processing of the delicate machined components is tedious and prone to user handling error. Because the PC-MEMS process encourages monolithic construction, the introduction of a single error in a constituent layer can render the entire laminate assembly inoperable.

In contrast, conventional construction approaches are more error-tolerant. Conventional approaches are characterized by manual assembly of discretely fabricated components. Specific to the mesoscale, discrete components are machined directly

from the appropriate bulk material and then manually manipulated and assembled into structures with tweezers under microscopes. This is very much akin to mechanical watch-making. Part design is much more straightforward than the intricate PC-MEMS multi-layer design process. Because the assembly process is manual, errors can be corrected as they appear. Components with errors can be discarded independently of the rest of the assembly, redesigned, and reintroduced to the assembly.

The conventional fabrication and assembly process can also be beneficial to the device from a functional standpoint, relative to the PC-MEMS methodology. The design of a complex, self-assembling PC-MEMS device tends to introduce more material and mechanism mass into the system than would otherwise be needed to construct it via a conventional assembly approach. In a context where system mass reduction is critical, non-functional mass is highly undesirable. The PC-MEMS device needs to introduce mechanisms that make it compatible with features required for the self-assembly process. These features become superfluous to the device's operation once it is fully assembled.

The downsides to the conventional construction approach are that they can be tedious, imprecise, and difficult to scale for large numbers. The quality and performance of a mechanism depends greatly on the precision of the individual assembler constructing it.

As many mesoscale devices are still confined to a research laboratory setting, on the order of ten prototypes is desirable to support research efforts. The scale of these mesoscale devices is still feasible for manual hand manipulation and assembly. In the development of the Robobee as a research prototype and platform, we have found that a combination of the two fabrication approaches is most economical. PC-MEMS is applied to construct individual components where it is convenient and can result in improved fabrication precision. For other features, conventional construction is

sufficient to support research iteration pace. Thus, the trade-offs between PC-MEMS and conventional construction methods must be reconciled for specific cases.

5.2 The specific needs of the Robobee

The results of the dual actuator bee development, described in Chapter 2, reveal the need for precision assembly. Until the PC-MEMS design and fabrication pipeline has matured, conventional fabrication and manual assembly steps remain a part of the development process. Early attempts to achieve the required precision resulted in flightworthy devices but were inconsistent [40]. Among mesoscale FWMAV devices in development, the dual actuator design in particular requires precision assembly. The two wing drives of the vehicle are completely decoupled. Because the FWMAV is operating at high frequencies, its dynamics are very susceptable to small perturbations in the mechanical symmetry of the vehicle. Additionally, as we operate the wing drives at resonance, any mismatch in the mechanical assemblies will result in different dynamics for each wing. When the trajectory of one wing differs from the other, the vehicle dynamics respond drastically.

Imperfect assembly compromises the vehicle's controllability. A crucial component of the trajectory is the resting position of the wing drive, which defines the average position of the flapping wing and thus the thrust vector position. The specifics of the mechanical design make this resting position dictated entirely by the success of the assembly procedure. Unintended locked-in stress during the assembly is released by a deflection of the resting position away from ideal, shown in Figure 5.3C, and is very difficult to account for post-assembly. As described in Section 3.1.1, the actuators operate within voltage bounds from 0-300V, constrained by the ceramic material's strain limits. If the resting position of the wing drive is off from ideal, a

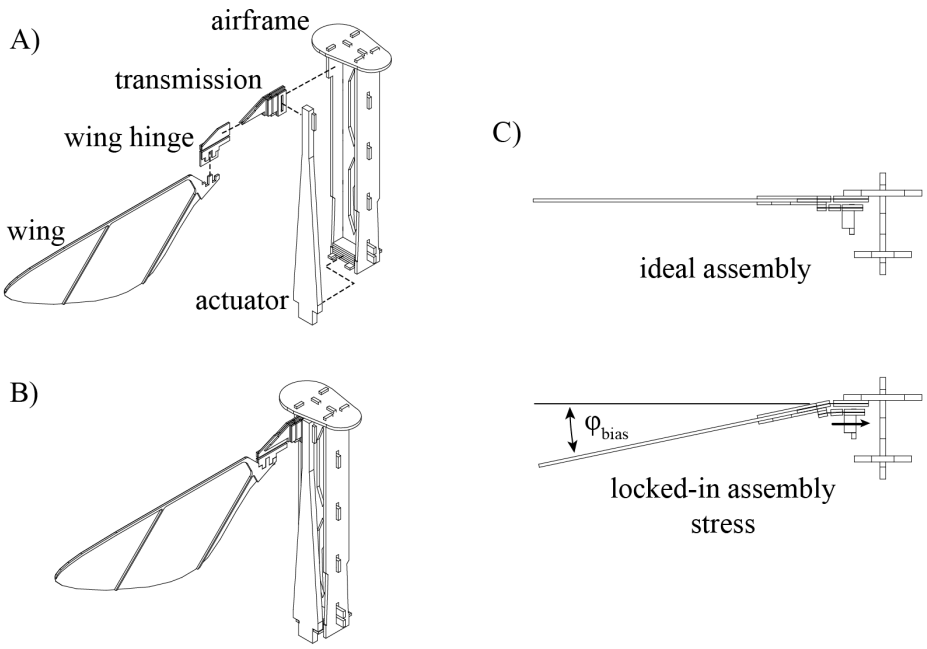

Figure 5.3: A) Exploded assembly of one side of the dual actuator bee, identifying the various parts. B) The fully assembled vehicle body. C) Top-vew of the assembly. If locked-in stress is present in the wing drive assembly, the resting position of the wing will be off-center, resulting in pitch torque bias in the vehicle. ϕ_{bias} is the wing bias angle.

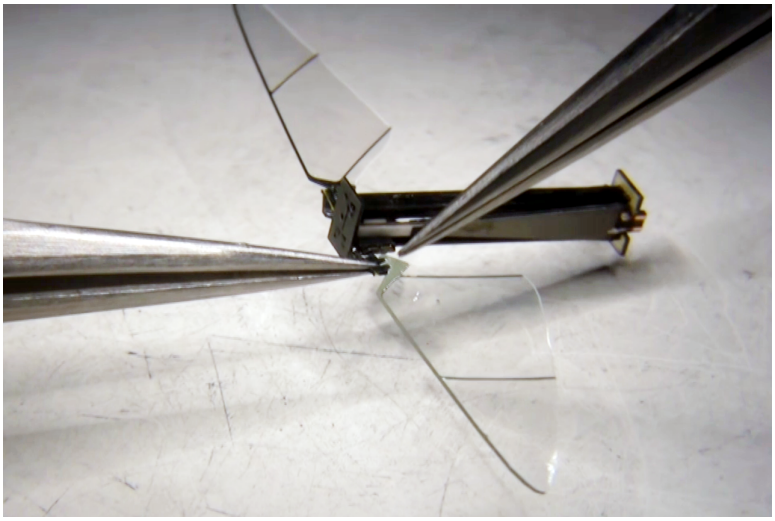

Figure 5.4: Manual manipulation and assembly of the Robobee using tweezers. Here, a wing is being attached to the body.

persistent driving signal offset can counteract it, but this will remove control authority by prematurely bringing the driving signal closer to the limits of the voltage range. If it is far from ideal, vehicle pitch control is compromised in one direction.

Our FWMAV developments have also revealed the benefits of modularity for research and development purposes. Ideally, the Robobees would be so simple to produce as to be easily replaced by another. In practice, the Robobees are difficult to construct, and each vehicle performs differently due to inconsistencies in manual assembly. Certain components are significantly more prone to failure than others, namely the wings and wing hinges. In addition, the wings and hinges can greatly influence the aerodynamic efficiency of the FWMAV and are in active development. It is convenient to preserve a meticulously constructed vehicle body and simply replace the wings and hinges as they fail or as better designs are discovered. Figure 5.4 illustrates this process. Though far more convenient than making an entire new Robobee, the replacement process is also a non-trivial assembly problem.

There are degrees of wear to the wings that may not necessitate complete removal

of a wing but are still significant enough to affect the FWMAVs flight performance. When small deformations are accrued in the wing membrane or the wing frame, they can lead to cyclical asymmetry in wing pitching dynamics that result in non-zero, time-averaged drag forces on a wing. This leads to persistent body moments that the vehicle may be unable to compensate for with available control inputs. However, a manual adjustment to the mechanical structure could alleviate the accrued wing asymmetry. This mechanical "tuning" ability can be designed into the vehicle. A different FWMAV design could alleviate this sensitivity to wing asymmetry, such as by active control of the wing rotation dynamics [52]. Alternatively, fabrication and assembly processes could be streamlined to the extent that Robobees are identical in performance and replaceable on a whole-vehicle basis.

5.3 Design-for-assembly analysis

Conventional fabrication and assembly approaches are economical for building small quantities of Robobee prototypes but face challenges in attaining the precision and repeatability of PC-MEMS automated assembly techniques. Ideally, we could generate vehicle fabrication and assembly procedures that can be unambiguously interpreted and allow for reliable vehicle construction and performance regardless of the researcher constructing it. For larger scale mechanical systems, such as cars and airplanes, Design for Assembly (DFA) analysis is an established design process for analysing and refining the assemblies of mass-produced devices with complex assemblies [55]. The goal of this analysis is to enable top-down assembly design from function to geometry. That is, based on the function of a multi-part device, coordinate the design of the components and the assembly such that they achieve the intended function reliably. A well designed assembly can compensate for variations in part manufacturing that

would otherwise accrue in the assembled device and reduce device yield. These same design principles can be applied to the mesoscale. The work on the Robobee has taken inspiration from a particular line of DFA research compiled by D.E. Whitney [54]. The DFA research field is expansive and covers a variety of topics relevant to mass-production. The most straightforward application of this analysis is for statically determinate assemblies. These are assemblies that do not contain internal stresses resulting from geometric conditions at any stage in their assembly. It is clear which parts determine the location of any particular part.

A relevant and immediately applicable aspect of this DFA analysis for use with mesoscale manufacturing is the datum flow chain (DFC) [54]. A datum flow chain is a diagram that represents the interconnections of various parts involved in an assembly and the assembly procedure, or sequence. It can be used to analyze the degree to which an assembly can reliably achieve its goal and provide guidance on diagnosing and solving problems if they exist. In a DFC, individual parts are represented by nodes, and their interconnections are represented by lines between nodes. An example DFC is illustrated for a simple, one-dimensional assembly in Figure 5.5. Four distinct lines are used to distinguish the interconnections, or joints:

A doubleline will indicate a "key characteristic" (KC). This is a critical geometric relation that the assembly must achieve in order for the device to function properly. The key characteristics are determined first in the design process for any assembly.

A single solid line with an arrow indicates a "mate." This is a joint that establishes, or "locates," full constraint of position and orientation between two parts. This relation is directional, in that the arrow points toward the part that is located by the other part. A node in the DFC diagram is designated a root or datum origin from which arrows emanate. These arrows cannot cycle back to the root node or the functional success of the assembly will be ambiguous. A closed loop of arrows would mean

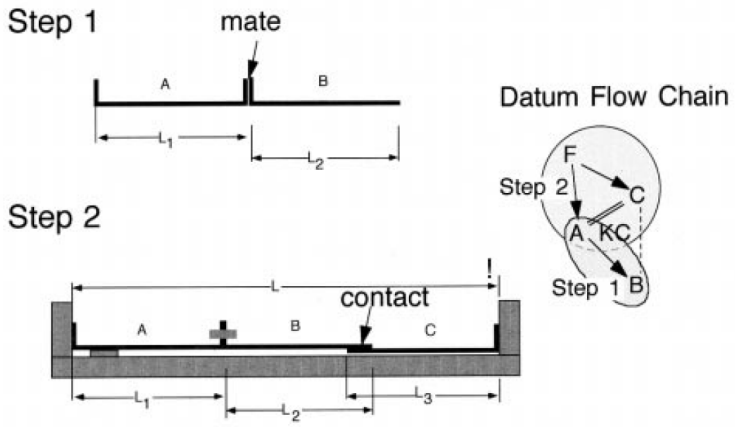

Figure 5.5: Example assembly and datum flow chain (DFC) diagram, from [55]. A one-dimensional assembly of three parts is considered. The key characteristic (KC) is the distance between parts A and C, identified by double lines in the DFC. Instead of simply attaching (or mating) parts A, B, and C sequentially, B and C are designed to have a contact joint. The first assembly step is to mate A and B. Then a fixture F is used to ensure A and C are the correct distance apart. The contact between B and C is then fixed. With this assembly design, manufacturing variations in A, B, or C are absorbed by the contact joint. Fixture F, if reused, allows the assembly process to consistently achieve the key characteristic.

a part locates itself. For statically determinate assemblies, a part cannot be mated to the datum chain until the datum part is fully constrained and located.

A dashed line indicates a "contact." This is a joint that does not constrain position or orientation between two parts. There is no directionality, as the parts do not locate each other until the contact becomes fixed and thus a mate. Contact joints are critical for absorbing the geometric variation that accrues in any assembly. As a rule for statically determinate assemblies, contacts cannot be fixed until the two participating parts have been fully located and constrained.

A dashed arrow line indicates a partial mate. This joint does establish constraint on a subset of the six possible degrees of freedom in a joint.

The datum flow chain thus contains information about how the various parts in an assembly join to form the final device. Temporary parts called "fixtures" can also

be introduced to the assembly when it is not possible for the assembly proper to repeatably locate each part. By focusing on the key characteristics and following the stated rules for fixing mates and contacts, a statically determinate assembly can be formed that will allow the device to reliably achieve its function. Other considerations in the design of an effective DFC include trying to decouple the key characteristics such that achieving one does not invalidate others. Lastly, situations can occur where a DFC is physically impossible or impractical to achieve, such as when certain fixtures or parts are inaccessible. In these situations, designer intuition will decide how to prioritize key characteristics or to transition to a less reliable but more practical DFC.

5.4 Design-for-assembly analysis applied to the Robobee

The Robobee vehicle body consists of three major components: the transmission, airframe, and actuator. These components are manufactured separately using different processes and have distinct manufacturing variability. The fabrication processes for all of these components are inherently planar and could be integrated into a single PC-MEMS assembly. While this could ease assembly and improve assembly yield rates, it adds considerable design and fabrication complexity and is not convenient for making design adjustments during this early phase of vehicle development.

The actuators are a laminated composite of piezoelectric ceramic, alumina ceramic, and resin-preimpregnated carbon fiber composite plates, as described in Chapter 2. The manufacturing process in its current form requires specific heat and pressure curing profiles for the resin that bonds the laminate, distinct from the processes for fabricating the other components. Significant manual processing and precharacterization occurs before the parts are ready for integration. As shown in the Figure 5.6, the variability in actuator free displacement is significant, as much as nearly 10%

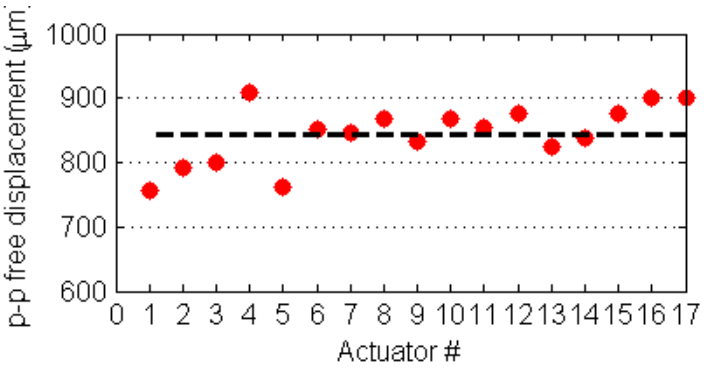

Figure 5.6: BigBee actuator fabrication data from 17 individual actuators, showing variations in peak-to-peak free displacement of up to 150 μm. Dashed line represents the mean free displacement of 840 um.

of the average free displacement. Selective assembly takes place to match actuators pairs with similar performance for integration.

The transmissions are fabricated via the PC-MEMS process and require no manual assembly steps. Three flexure hinge joints are fabricated simultaneously on parallel planes, as described in Figure 5.7. The part variation is not noticeable, highlighting a key benefit of the PC-MEMS.

The airframe is constructed via conventional part machining and assembly. Separate components are machined out of stock carbon fiber composite laminate and manually assembled together. Features are designed into the components to assist with the assembly process, as illustrated in Figure 5.8. The airframe's geometry was simple enough to construct reliably with manual assembly and did not warrant the introduction of the design complexity and fabrication overhead from PC-MEMS, although the structure is very amenable to the PC-MEMS process and consists of multiple planar elements. The transmission and airframe could be designed as a single PC-MEMS component, but this would remove a degree of freedom between the transmission and airframe. As will be described below, this is detrimental to achieving the ideal angle between the wing and body plane, the key characteristic of the

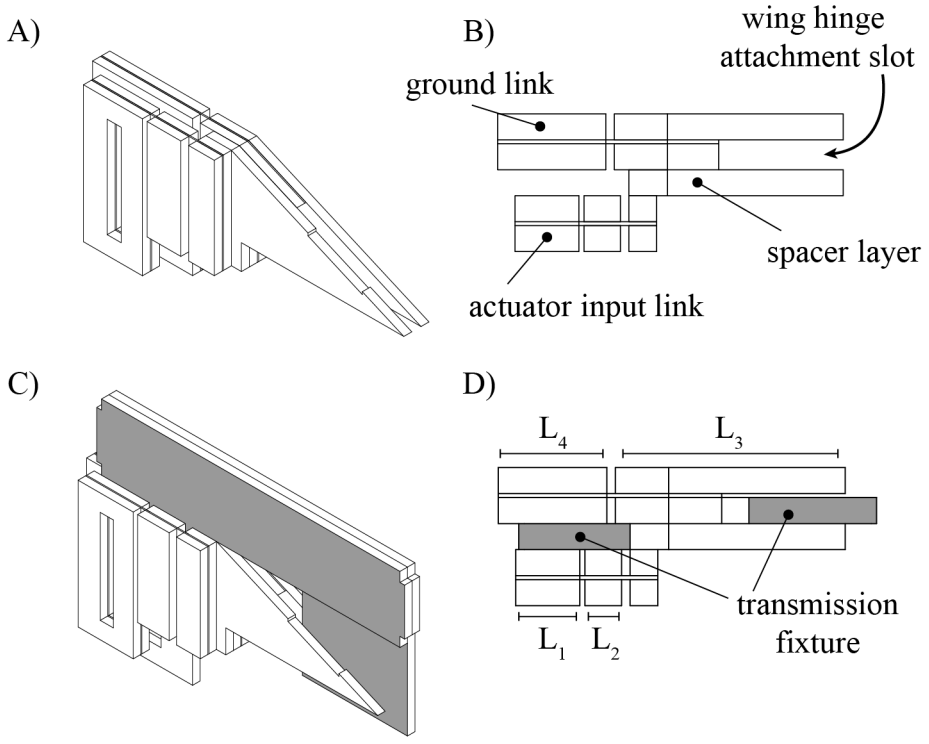

Figure 5.7: A) The transmission mechanism is instantiated with the PC-MEMS process. B) Two linkage sublaminates and one structural spacer layer forms the linkage, consisting of three flexure hinges. The thickness of the spacer layer dictates the L_3 link length. The modular attachment slot for the wing hinge is constructed from the layers as well. C and D) Assembly fixture (grey) for the transmission linkage component. A separately fabricated component is slotted into the transmission to immobilize the flexure hinges during the assembly process. Once the assembly is fixed, the fixture is removed. This fixture is labeled fixture F1 in Figure 5.9A. The links of the transmission are also labeled for reference in Figure 5.10A.

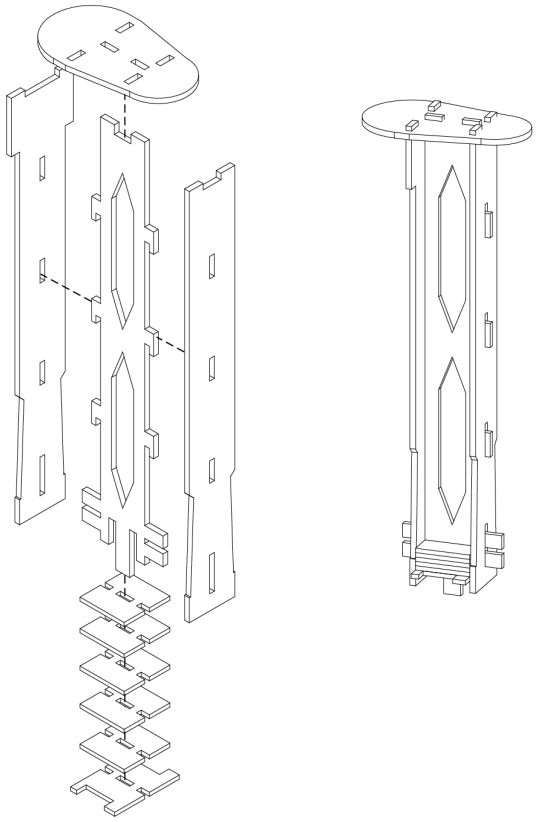

Figure 5.8: The airframe for the dual actuator bee is constructed from multiple, rigid carbon fiber laminate components, machined separately. It is assembled manually, with slots, tabs, and locking features to assist.

Robobee assembly.

As separate parts, the actuator, transmission, and airframe must be manually assembled and fixed with adhesive (commonly liquid cyanoacrylate glue). Liquid adhesive is used because discrete fasteners are inconvenient to work with at this scale. Assembly errors are easy to introduce, difficult to observe, and difficult compensate for because of the small scale. Tweezers and microscopes are necessary but have limited force- and visual feedback. The most prevalent and insidious assembly error is the locked-in stress from overconstraining the actuator as it is fixed to the airframe. The locked-in stress is released by deforming the most compliant joint in the kinematic chain. In this case, the compliant transmission hinges will deflect from their ideal

resting positions, as illustrated in Figure 5.3C. Without a reliable assembly design, many trials and iterations are needed to acquire the understanding and intuition for a specific assembly procedure.

DFA analysis can improve the assembly's reliability. In applying the DFA analysis to the Robobee, we must identify the key characteristics of the system. Our initial designs of the dual actuator bee focused on creating a visually symmetric system. The two wings were designed to be at the same level and strictly outstretched perpendicular to the body axis. The transmission would mate to the airframe rigidly to produce this characteristic. We considered this to be a straightforward and inevitable design constraint, considering the obvious need for symmetry in the system. But our subsequent system characterizations and flight tests, while successful, indicated that the resting wing angle was the most significant contributor to the successful operation of a vehicle. Few constructed prototypes with the early assembly design could perform reliably. It was clear that the resting angle was the critical key characteristic of the vehicle.

It was also discovered over the course of our flight experiments that the mechanical grounding of the actuators to the airframe was critical to vehicle operation. If the ground joint was compliant, it would absorb output energy from actuator that would otherwise be used to drive the wing. The actuator is attached to the airframe with epoxy adhesive. To achieve a rigid joint, the actuator base must be in close contact with the attachment surface to minimize the bond line. This is a second key characteristic for the dual actuator bee design.

Figure 5.10A represents all parts in the assembly as nodes in a DFC. Note that the wing resting angle key characteristic is KC1 and stretches between the airframe and transmission link L_3. Despite being fabricated as a single part, the transmission is represented as separate links, identified in Figure 5.7. This consideration is important

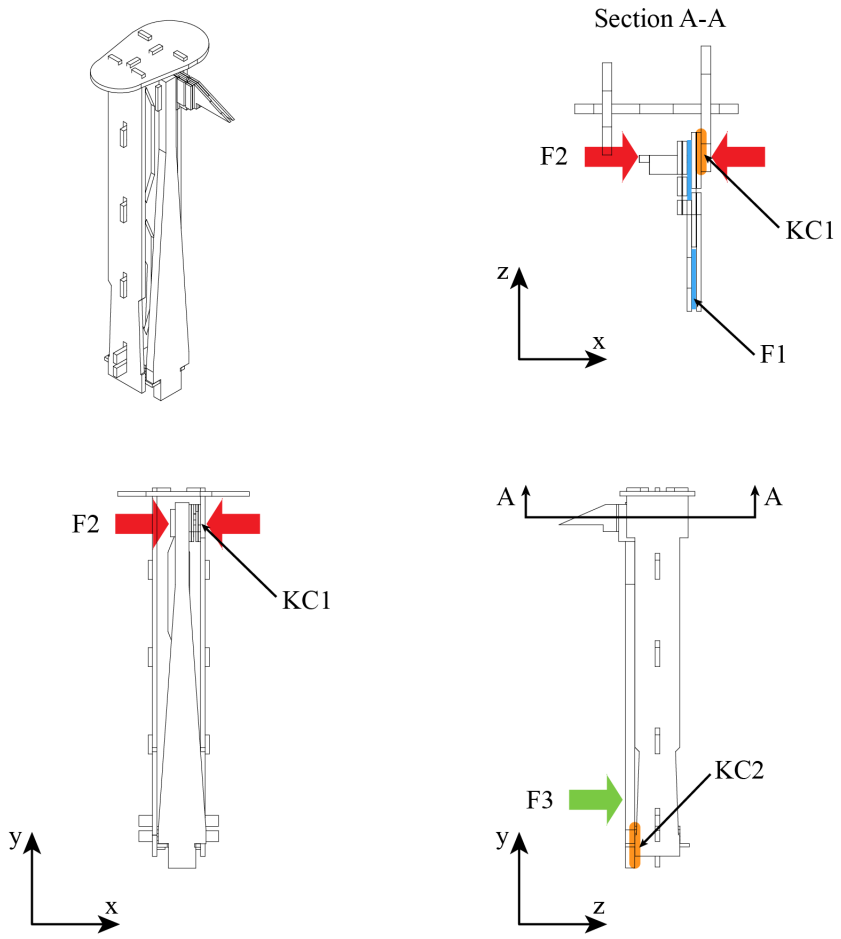

Figure 5.9: Multiview orthographic projections for one wing drive of the dual actuator bee, for reference with Figure 5.10. The key characteristics (KC) are indicated. KC1 is a slip plane between the transmission link L4 and the airframe. KC2 is the contact between the actuator base and the airframe. Assembly fixtures are also indicated. Fixture F1 (blue) is the transmission fixture from Figure 5.7. Fixture F2 (red) is a force pressing the transmission and airframe together. Fixture F3 (green) is a force pressing the actuator and airframe together. The actions of F2 and F3 must be restricted to very specific directions of constraint. Body coordinates are also shown.

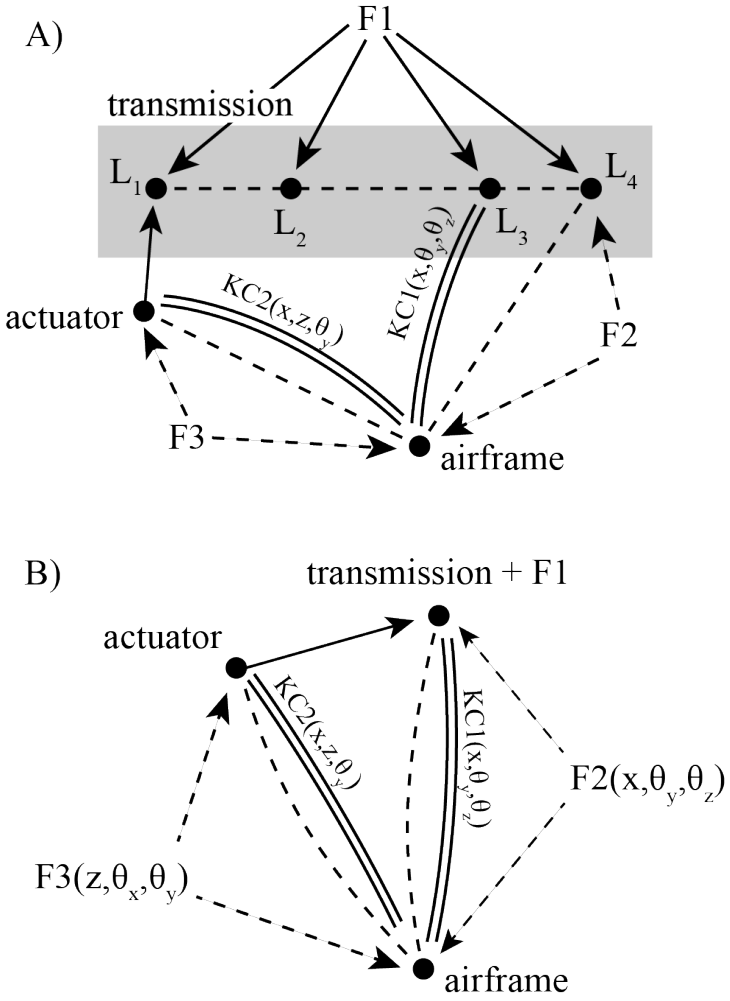

Figure 5.10: Datum flow chain (DFC) diagrams for the dual actuator bee assembly. A) The complete DFC for the dual actuator bee. Between each node, six degrees of freedom (dof) are present, relative to the body coordinates as indicated in Figure 5.9. $\theta_x, \theta_y, \theta_z$ are rotations about the indicated axes. The key characteristics KC1 and KC2 encompass a subset of possible dofs, indicated in the parentheses. Dashed lines represent contact joints. Dashed arrow lines represent partially constrained mates. Solid arrow lines represent fully constrained mates. The transmission links are defined in Figure 5.7. B) A modified DFC for the dual actuator bee. The transmission and fixture F1 are lumped into a single component. The dofs constrained by the fixtures F2 and F3 are explicitly shown.

for flexure hinge mechanisms. Strictly speaking, each link is not fully constrained to the neighboring links and forms partially constrained mates with each other. However, the relative motion between these links is undesirable during assembly. The immobilization of the flexure hinges during assembly is also a key characteristic for the DFA analysis, though not illustrated for simplicity. To restrict motion, a temporary fixture should be implemented and removed once the transmission is fixed, illustrated in Figure 5.7.

This consideration for immobilizing flexure hinges is generalizable to other assembly designs that need to integrate dynamic flexure hinge mechanisms into assemblies. Fixtures must be present and effective in restricting link motion until the assembly is complete. Otherwise, flexure hinge compliance during assembly can undermine the repeatability of the assembly process. The design and implementation of fixtures is challenging, particularly for small scale devices. Fixtures can be in close proximity with joints that need to be fixed with liquid adhesives. Parasitic seepage of adhesive onto fixtures will prevent their removal. Escape directions for the removal of the fixture must also be considered. The fixture should be substantial enough to maintain the key relations but avoid complicating the assembly handling, such as blocking access to critical assembly features.

The DFC diagram in Figure 5.10A contains many partial mates, and it is unclear whether the key characteristics are achieved. Because both key characteristics share the airframe, it is not straightforward to achieve both simultaneously. For example, if fixture F3 fully constrains the actuator to the airframe and fulfills the key characteristic KC2, the transmission contact joint to the airframe is also fully constrained, regardless of whether it achieved KC1. Instead of either fixtures F2 or F3 fully constraining assembly nodes, we must analyze the assembly for the individual dofs. The same assembly is described by the modified DFC diagram in Figure 5.10B.

For visual simplicity, the diagram lumps the various transmission links into a single node because fixture F1 fully constrains them. The DFC explicitly stipulates the dofs that each fixture constrains. By following the chain of mates for each dof, we see that except for θ_y, the dofs in each key characteristic are achieved by the assembly without overconstraint. The fixtures are designed to constrain a non-overlapping set of dofs.

The exception is θ_y which is constrained by both F2 and F3. The current version of the assembly design retains this potential issue because the current assembly and fixture design has given satisfactory results with an acceptable degree of assembly ease. In the future, if the final assembly repeatedly exhibits unacceptable locked-in stress, the designer can focus attention on addressing this dof.

With assembly design, a multitude of situations can arise. Implementing fixtures is a versatile initial strategy. By experimenting with the assembly, some fixtures may be deemed too inconvenient to construct or use. Situations can arise where key characteristics are coupled and cannot be simultaneously achieved. It may be necessary to compromise on certain key characteristics based on where variation is tolerable.

Mesoscale assembly has a distinct feature over macroscale assembly in that the fixtures are typically small and inexpensive. In comparison, fixtures for airplanes and cars are very expensive to create and maintain [54]. The main difficulty in implementing mesoscale assembly design is that a fair amount of intuition about the specific micromanipulation tasks is required to assess the "convenience" or practicality of certain assembly strategies.

5.4.1 BigBee considerations

The BigBee vehicle design uses larger actuators which output more force for the system. The maximum force output is 5.1 times larger than in the dual actuator

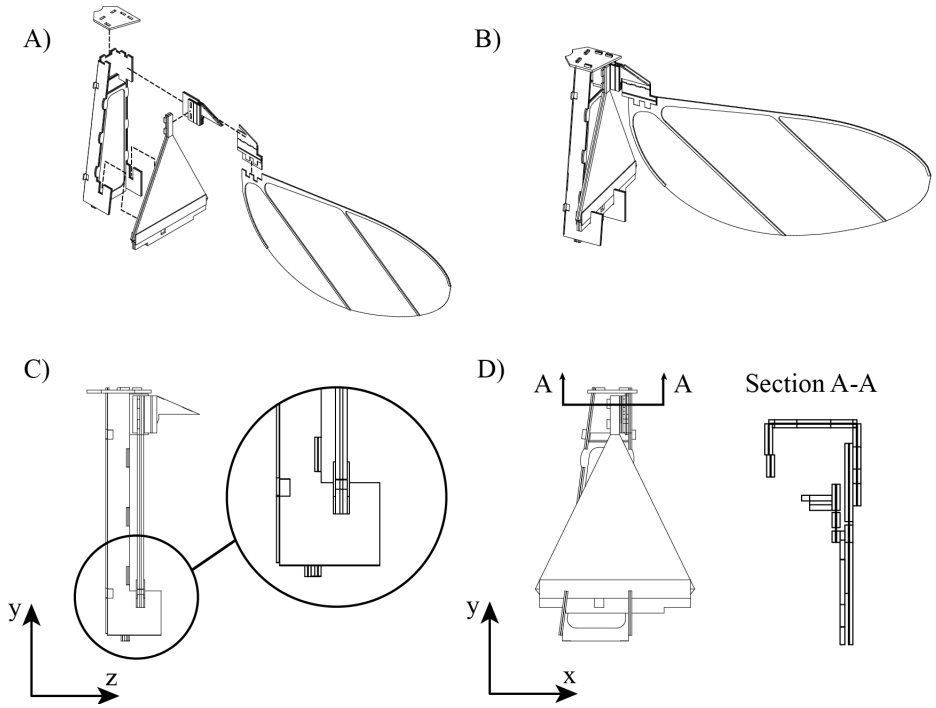

Figure 5.11: A) Exploded view of one BigBee half. The same vehicle components are present as in the dual actuator bee in Figure 5.3A. B) Fully assembled BigBee half. C) Side view. The actuator base is grounded to the airframe via clips that surround the actuator base at two points. D) Front view and section view. Construction of the BigBee is essentially the same as the dual actuator bee.

bee, as described in Chapter 3. A stronger mechanical ground must be established between the actuator base and the airframe. The mass of the structure must also be minimized. We modified the attachment scheme on the airframe by loosely wrapping around the actuator base at two points. This constrains the actuator base in two dofs, as illustrated in the DFC diagrams for the BigBee design (Figure5.12). Additional reinforcements to the airframe-actuator clips are added after the main assembly is fixed.

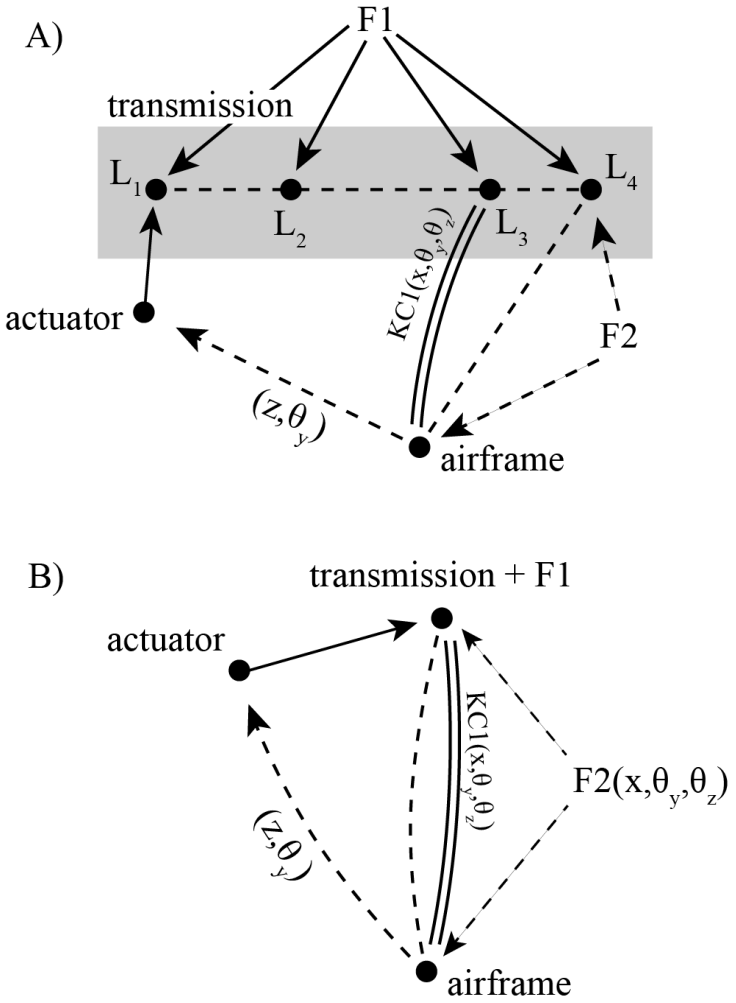

Figure 5.12: DFC diagrams for BigBee. A) The full DFC for BigBee. As shown in Figure 5.11, the actuator base is loosely captured by clips on the airframe. This restricts its motions in 2 dofs: z and θ_y. The assembly no longer requires the second KC2 or F3 from the dual actuator bee assembly (Figure 5.10) to ensure good grounding of the actuator base. KC1 and F2 remain the same. B) Simplified DFC diagram lumping the transmission and F1 into one node.

5.5 Post-assembly vehicle modifications

The adhesive used in our mesoscale assemblies is typically cyanoacrylate adhesive. It is versatile and can be softened at elevated temperatures. These nonpermanent bonds can allow for replacement of accessible components, such as the wings, wing hinges, or one half of the BigBee. In practice, this task is difficult and requires substantial manual skill to perform. But the option to preserve or modify the functionality of a vehicle by replacing components is a useful one for supporting research efforts.

In Section 5.2, we mentioned the need for mechanical vehicle tuning when the flight controller is unable to compensate for persistent torques in the assembled vehicle. We have explored two methods for introducing tunable degrees of freedom into the vehicle designs, for vehicle yaw and pitch tuning. Persistent yaw torque bias can be attributed to wing or wing hinge damage, which cause the cyclic wing pitching dynamics to become asymmetric. To counter this, we can bias the wing hinge resting pitch angle such that the cyclic pitching dynamics are closer to symmetry. We adjust this post-assembly by introducing a secondary flexure hinge parallel to the wing hinge. This flexure hinge can be fixed at the necessary pitch bias angle with glue. If needed, the glue can be softened and rehardened to allow for adjustment of the resting pitch angle. Figure 5.13 illustrates this concept.

Pitch torque bias is the result of the vehicle's net thrust vector not aligning with the vehicle's center of mass. We can offset mass on the vehicle to move the center of mass, though this is not an elegant solution and is difficult to perform consistently without dedicated mechanical features. We can also move the thrust vector relative to the center of mass by changing the resting angle of the wings, though this is difficult. With the BigBee design, the two separate halves of the robot can be rotated relative to each other. We implemented a sliding contact joint between the two vehicle halves that restricts motion to a single rotational degree of freedom, as illustrated in Figure

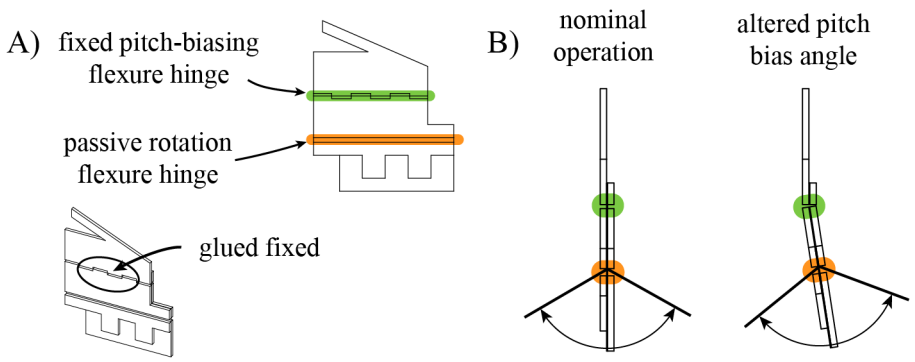

Figure 5.13: Detail on the BigBee wing hinge from Figure 5.11. A) A second parallel flexure hinge (green) can be added to allow for tuning of the resting pitch angle (orange). B) Side view illustrating the effect of biasing the fixed flexure hinge.

5.14. Once that contact is fixed, other rigid members are attached to reinforce the assembly. These are examples of mechanical designs for post-assembly vehicle tuning. Other designs are possible; they must consider the trade-off between the convenience of post-assembly tuning and the added mass of additional mechanical features.

5.6 Concluding remarks

Mesoscale manufacturing of mechanical structures and mechanisms has been accelerated by the innovation of multi-layer, composite flexure-hinge fabrication techniques. This is best instantiated in the PC-MEMS methodology, which has been applied to create unprecedented mechanical complexity at the mesoscale. But the lack of a mature design and fabrication pipeline hinders its application for research laboratory use. The manual assembly, which relies on the skilled use of tweezers and other specialized tools, remains a substantial component of the manufacturing process. Construction consistency is difficult because of limited force feedback and visual feedback. However, it is possible to consistently hand-construct mesoscale mechanical devices by systematic analysis and design of the mechanical assembly. This analysis is directly

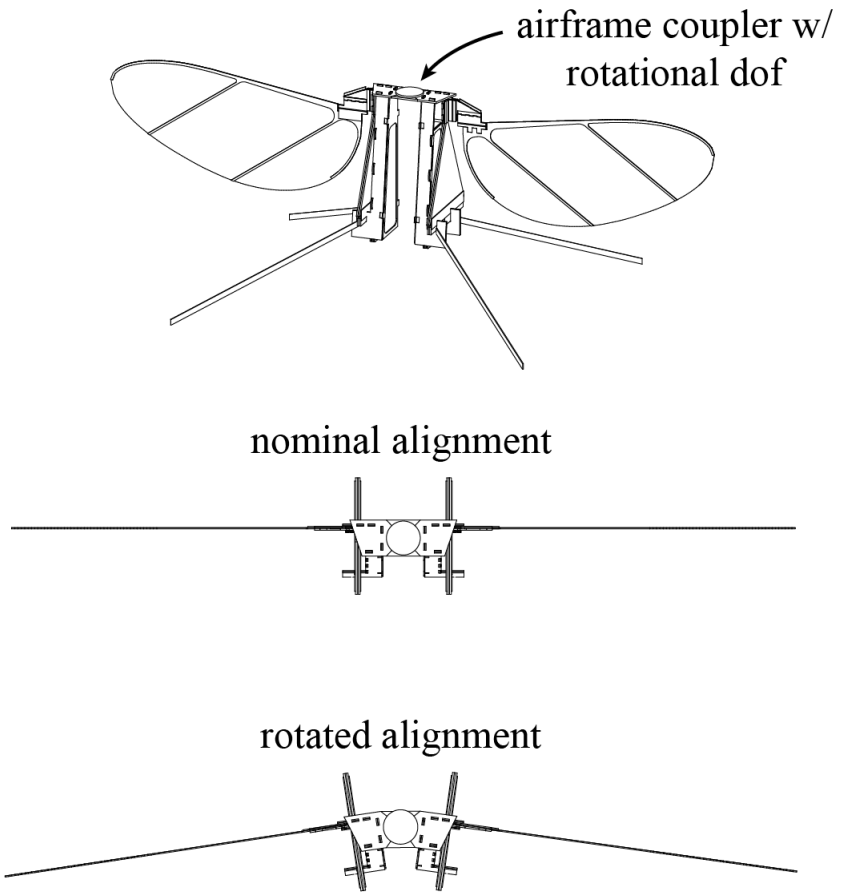

Figure 5.14: Two BigBee halves can be coupled with a rotational degree of freedom (dof) to allow for tuning of the resting wing angle. By rotating the relative resting angles forward, the wing's thrust vectors are placed fore-aft to the vehicle center of mass, creating a pitching moment on the vehicle. The coupler angle can be adjusted post-assembly via heat-softening the adhesive. Not shown are additional coupler beams to strengthen the coupled airframe structure.

adapted from the Design-for-Assembly analysis process for macroscale systems. A unique consideration for flexure hinge mechanisms is needed to fix the links of the kinematic chains during assembly by implementing fixtures.

The dual actuator design of the Robobee is especially susceptible to manual assembly errors because it is underactuated and cannot actively correct for mechanical inconsistencies. By careful consideration of the vehicle's functional needs, we have drastically improved the reliability of the manually assembled vehicles. It is difficult to quantify the improvement in construction ease and reliability without extensive data collected on construction times and resulting vehicle performance. Over the course of two years, over 20 dual actuator bee prototypes have been constructed by various researchers and approximately half have exhibited flight performance sufficient for supporting further experimentation. During this period, the manufacturing processes evolved into what is currently presented here. It remains to be seen if the current iteration of the vehicle assembly design is sufficiently assessible and reliable for the next generation of researchers.

Chapter 6

Conclusions and future work

The major contribution of this dissertation is in convincingly demonstrating the feasibility of insect-scale flying vehicles. The dual actuator bee vehicle design became the first flapping-wing, insect-scale air vehicle to demonstrate controlled flight. Its creation encompassed developments in mechanical design, manufacturing, and flight control. Basic characterizations have shown the vehicle to be capable of sufficient torque generation. The unequivocal evidence for its capabilities were shown in closed-loop control experiments where, in conjunction with developed closed-loop controllers, it was able to maintain stability and achieve aggressive flight maneuvers.

Sensors and electronics still need to be integrated on the vehicle to enable autonomous flight. Early research efforts on integrating these components have used the vehicle design as an experimental platform. However, as the initial vehicle design did not have the payload capacity to carry more than one experimental component at a time, a new vehicle design was required to sustain development toward an integrated, autonomous flying vehicle.

The method for accomplishing this design goal was two-fold: First, a rough approximation of the scaled vehicle was sized and constructed. This "BigBee" design proved to be capable of payload capacities exceeding what was required for control autonomy. The second step involved a system modeling and optimization procedure

that relies on empirical measurements from BigBee experiments to support modeling accuracy for various uncertainties in FWMAV system. The results of the vehicle sizing effort was a design prescription that approaches the needs of a power-autonomous vehicle.

Vehicle development at this miniature scale has been crucially supported by significant advances in manufacturing techniques. The work in this dissertation coincided with the development of PC-MEMS: a versatile fabrication paradigm relying on composite laminate construction techniques. PC-MEMS was developed as a direct response to the fabrication intricacies of constructing insect-scale FWMAVs. Fabrication intricacies specific to the dual actuator design spurred systematic analyses on assembly design for mesoscale machines. Borrowing heavily from DFA analyses of macroscale vehicles, the fabrication and assembly procedures for FWMAVs were refined to reliably produce prototypes. This understanding of manufacturing at the mesoscale will ensure that mesoscale machine designs can reliably achieve their desired functionality.

For future work, an immediate next step is to construct the prescribed design and verify its capabilities to generate the target thrust force. The sensors and electronic components necessary for control autonomy can then be packaged and integrated into the body of the robot. The BigBee vehicle was designed to facilitate this integration step and is built in two separate halves to ensure mass-symmetric placement of the payload.

In parallel, it is desirable to characterize the flight envelope of the vehicle. The vehicle sizing effort presented here only considers vehicle requirements for ensuring power autonomy. However, other performance metrics, relevant to particular "missions" (using the aerospace industry term), will likely influence the optimal vehicle design. For example, flight speed will likely constrain maximum wing size and aerial

maneuverability will dictate the required torque capabilities of the vehicle. Understanding the design features needed to achieve these vehicle requirements will require more flight testing in tandem with improved force measurements and modeling of whole-vehicle dynamics.

The system modeling awaits more refined modeling of the aerodynamics and its effect on the wing dynamics. The passive rotation hinge adds complexity to the analysis because its dynamics are closely tied to the aerodynamics of the wings. A more detailed model of the wing kinematics and its relation to the aerodynamics will be critical for establishing a robust vehicle optimization procedure. Recent experiments and analyses have made progress on identifying this model.

Finally, the vehicle design has performance limitations, most prominently in generating yaw torques. Based on the dual actuator design morphology, a new mechanical design has been proposed that can more effectively modulate yaw torques [52]; recent results have verified its improved controllability. Its mechanical complexity is significantly greater than the basic dual actuator bee design, and it remains to be determined if the increased vehicle performance will justify the increased construction complexity.

What is clear from the work presented in this dissertation is that insect-scale FWMAVs are feasible. The manufacturing techniques, previously a significant obstacle toward development, have been sufficiently refined and can reliably produce flight-worthy vehicles. The fabrication procedures defined here are sufficient for producing prototype quantities to support laboratory developments. Once a vehicle design optimized for particular flight tasks has been established, a very directed effort will be required to achieve mass production. PC-MEMS provides a very feasible avenue for accomplishing this. It will be an exciting and inevitable direction to take for the ongoing development of insect-scale FWMAVs.

Bibliography

[1] Daniel M Aukes, Benjamin Goldberg, Mark R Cutkosky, and Robert J Wood. An analytic framework for developing inherently-manufacturable pop-up laminate devices. *Smart Materials and Structures*, 23(9):094013, 2014.

[2] Daniel M Aukes and Robert J Wood. Algorithms for rapid development of inherently-manufacturable laminate devices. In *ASME 2014 Conference on Smart Materials, Adaptive Structures and Intelligent Systems*, pages V001T01A005–V001T01A005. American Society of Mechanical Engineers, 2014.

[3] Srinath Avadhanula, Robert J Wood, Erik Steltz, Joseph Yan, and Ronald S Fearing. Lift force improvements for the micromechanical flying insect. In *Intelligent Robots and Systems, 2003.(IROS 2003). Proceedings. 2003 IEEE/RSJ International Conference on*, volume 2, pages 1350–1356. IEEE, 2003.

[4] Attila J Bergou, Leif Ristroph, John Guckenheimer, Itai Cohen, and Z Jane Wang. Fruit flies modulate passive wing pitching to generate in-flight turns. *Physical review letters*, 104(14):148101, 2010.

[5] Pakpong Chirarattananon. Flight control of a millimeter-scale flapping-wing robot. 2014.

[6] Pakpong Chirarattananon, Kevin Y Ma, and Robert J Wood. Fly on the wall. In *Biomedical Robotics and Biomechatronics (2014 5th IEEE RAS & EMBS International Conference on*, pages 1001–1008. IEEE, 2014.

[7] Pakpong Chirarattananon, Kevin Y Ma, and Robert J Wood. Single-loop control and trajectory following of a flapping-wing microrobot. In *Robotics and Automation (ICRA), 2014 IEEE International Conference on*, pages 37–44. IEEE, 2014.

[8] CIA.gov. Insectothopter: The bug-carrying bug, 2013. [Online; accessed 22-May-2015].

[9] SA Combes and TL Daniel. Flexural stiffness in insect wings i. scaling and the influence of wing venation. *Journal of experimental biology*, 206(17):2979–2987, 2003.

[10] SA Combes and TL Daniel. Flexural stiffness in insect wings ii. spatial distribution and dynamic wing bending. *Journal of Experimental Biology*, 206(17):2989–2997, 2003.

[11] Thomas L Daniel and Stacey A Combes. Flexible wings and fins: bending by inertial or fluid-dynamic forces? *Integrative and Comparative Biology*, 42(5):1044–1049, 2002.

[12] GCHE De Croon, KME De Clercq, R Ruijsink, B Remes, and C De Wagter. Design, aerodynamics, and vision-based control of the delfly. *International Journal of Micro Air Vehicles*, 1(2):71–97, 2009.

[13] Guido CHE de Croon, MA Groen, Christophe De Wagter, Bart Remes, Rick Ruijsink, and Bas W van Oudheusden. Design, aerodynamics and autonomy of the delfly. *Bioinspiration & biomimetics*, 7(2):025003, 2012.

[14] Alexis Lussier Desbiens, Yufeng Chen, and Robert J Wood. A wing characterization method for flapping-wing robotic insects. In *Intelligent Robots and Systems (IROS), 2013 IEEE/RSJ International Conference on*, pages 1367–1373. IEEE, 2013.

[15] Michael H Dickinson, Fritz-Olaf Lehmann, and Sanjay P Sane. Wing rotation and the aerodynamic basis of insect flight. *Science*, 284(5422):1954–1960, 1999.

[16] William B Dickson, Peter Polidoro, Melissa M Tanner, and Michael H Dickinson. A linear systems analysis of the yaw dynamics of a dynamically scaled insect model. *The Journal of experimental biology*, 213(17):3047–3061, 2010.

[17] David B Doman, Michael W Oppenheimer, and David O Sigthorsson. Wingbeat shape modulation for flapping-wing micro-air-vehicle control during hover. *Journal of Guidance, Control, and Dynamics*, 33(3):724–739, 2010.

[18] Robert Dudley. *The biomechanics of insect flight: form, function, evolution*. Princeton University Press, 2002.

[19] P-EJ Duhamel, Nestor O Perez-Arancibia, Geoffrey L Barrows, and Robert J Wood. Biologically inspired optical-flow sensing for altitude control of flapping-wing microrobots. *Mechatronics, IEEE/ASME Transactions on*, 18(2):556–568, 2013.

[20] Charles P Ellington. The novel aerodynamics of insect flight: applications to micro-air vehicles. *Journal of Experimental Biology*, 202(23):3439–3448, 1999.

[21] CP Ellington. The aerodynamics of hovering insect flight. i. the quasi-steady analysis. *Philosophical Transactions of the Royal Society B: Biological Sciences*, 305(1122):1–15, 1984.

[22] CP Ellington. The aerodynamics of insect flight. ii. morphological parameters. *Phil. Trans. R. Soc. Lond. B*, 305:17–40, 1984.

[23] A Roland Ennos. The importance of torsion in the design of insect wings. *Journal of Experimental Biology*, 140(1):137–160, 1988.

[24] Anna Evans, Anja Bieberle-Hütter, Jennifer LM Rupp, and Ludwig J Gauckler. Review on microfabricated micro-solid oxide fuel cell membranes. *Journal of Power Sources*, 194(1):119–129, 2009.

[25] R Fearing, Srinath Avadhanula, Domenico Campolo, Metin Sitti, Joseph Yan, and Robert Wood. A micromechanical flying insect thorax. *Neurotechnology for Biomimetic Robots*, pages 469–480, 2002.

[26] Benjamin M Finio, Néstor Osvaldo Pérez-Arancibia, and Robert J Wood. System identification and linear time-invariant modeling of an insect-sized flapping-wing micro air vehicle. In *Intelligent Robots and Systems (IROS), 2011 IEEE/RSJ International Conference on*, pages 1107–1114. IEEE, 2011.

[27] Benjamin M Finio and Robert J Wood. Open-loop roll, pitch and yaw torques for a robotic bee. In *Intelligent Robots and Systems (IROS), 2012 IEEE/RSJ International Conference on*, pages 113–119. IEEE, 2012.

[28] Steven N Fry, Rosalyn Sayaman, and Michael H Dickinson. The aerodynamics of free-flight maneuvers in drosophila. *Science*, 300(5618):495–498, 2003.

[29] Steven N Fry, Rosalyn Sayaman, and Michael H Dickinson. The aerodynamics of hovering flight in drosophila. *Journal of Experimental Biology*, 208(12):2303–2318, 2005.

[30] Sawyer B Fuller, E Farrell Helbling, Pakpong Chirarattananon, and Robert J Wood. Using a MEMS gyroscope to stabilize the attitude of a fly-sized hovering robot. In *IMAV 2014: International Micro Air Vehicle Conference and Competition 2014, Delft, The Netherlands, August 12-15, 2014*. Delft University of Technology, 2014.

[31] Sawyer B Fuller, Michael Karpelson, Andrea Censi, Kevin Y Ma, and Robert J Wood. Controlling free flight of a robotic fly using an onboard vision sensor inspired by insect ocelli. *Journal of The Royal Society Interface*, 11(97):20140281, 2014.

[32] E Farrell Helbling, Sawyer B Fuller, and Robert J Wood. Pitch and yaw control of a robotic insect using an onboard magnetometer. In *Robotics and Automation (ICRA), 2014 IEEE International Conference on*, pages 5516–5522. IEEE, 2014.

[33] Lindsey L Hines, Veaceslav Arabagi, and Metin Sitti. Free flight simulations and pitch and roll control experiments of a sub-gram flapping-flight micro aerial vehicle. In *Robotics and Automation (ICRA), 2011 IEEE International Conference on*, pages 1–7. IEEE, 2011.

[34] Noah T Jafferis, Michael J Smith, and Robert J Wood. Design and manufacturing rules for maximizing the performance of polycrystalline piezoelectric bending actuators. *Smart Materials and Structures*, 2015.

[35] Michael Karpelson, Gu-Yeon Wei, and Robert J Wood. Milligram-scale high-voltage power electronics for piezoelectric microrobots. In *Robotics and Automation, 2009. ICRA'09. IEEE International Conference on*, pages 2217–2224. IEEE, 2009.

[36] Michael Karpelson, John Peter Whitney, Gu-Yeon Wei, and Robert J Wood. Energetics of flapping-wing robotic insects: towards autonomous hovering flight. In *Intelligent Robots and Systems (IROS), 2010 IEEE/RSJ International Conference on*, pages 1630–1637. IEEE, 2010.

[37] Matthew Keennon, Karl Klingebiel, Henry Won, and Alexander Andriukov. Development of the nano hummingbird: A tailless flapping wing micro air vehicle. In *AIAA Aerospace Sciences Meeting*, pages 1–24, 2012.

[38] David Lentink and Michael H Dickinson. Rotational accelerations stabilize leading edge vortices on revolving fly wings. *Journal of Experimental Biology*, 212(16):2705–2719, 2009.

[39] Mario Lok and Gu-Yeon Wei. A power electronics unit to drive piezoelectric actuators for flying microrobots. In *Custom Integrated Circuits Conference*. IEEE, 2015.

[40] Kevin Y Ma, Samuel M Felton, and Robert J Wood. Design, fabrication, and modeling of the split actuator microrobotic bee. In *Intelligent Robots and Systems (IROS), 2012 IEEE/RSJ International Conference on*, pages 1133–1140. IEEE, 2012.

[41] James H Marden. Maximum lift production during takeoff in flying animals. *Journal of Experimental Biology*, 130(1):235–258, 1987.

[42] Andrew M Mountcastle and Thomas L Daniel. Aerodynamic and functional consequences of wing compliance. In *Animal Locomotion*, pages 311–320. Springer, 2010.

[43] Florian T Muijres, Michael J Elzinga, Johan M Melis, and Michael H Dickinson. Flies evade looming targets by executing rapid visually directed banked turns. *Science*, 344(6180):172–177, 2014.

[44] Christopher T Orlowski and Anouck R Girard. Dynamics, stability, and control analyses of flapping wing micro-air vehicles. *Progress in Aerospace Sciences*, 51:18–30, 2012.

[45] Néstor O Pérez-Arancibia, Kevin Y Ma, Kevin C Galloway, Jack D Greenberg, and Robert J Wood. First controlled vertical flight of a biologically inspired microrobot. *Bioinspiration & Biomimetics*, 6(3):036009, 2011.

[46] Powerstream.com. *Ultra low weight lithium ion batteries*, 2015.

[47] Singiresu S Rao and Fook Fah Yap. *Mechanical vibrations*, volume 4. Addison-Wesley Reading, 1995.

[48] Daniel P Raymer. Aircraft design: A conceptual approach, american institute of aeronautics and astronautics. *Inc., Reston, VA*, 1999.

[49] Leif Ristroph, Attila J Bergou, Gunnar Ristroph, Katherine Coumes, Gordon J Berman, John Guckenheimer, Z Jane Wang, and Itai Cohen. Discovering the flight autostabilizer of fruit flies by inducing aerial stumbles. *Proceedings of the National Academy of Sciences*, 107(11):4820–4824, 2010.

[50] Pratheev S Sreetharan, John P Whitney, Mark D Strauss, and Robert J Wood. Monolithic fabrication of millimeter-scale machines. *Journal of Micromechanics and Microengineering*, 22(5):055027, 2012.

[51] Ke Sun, Teng-Sing Wei, Bok Yeop Ahn, Jung Yoon Seo, Shen J Dillon, and Jennifer A Lewis. 3D printing of interdigitated Li-Ion microbattery architectures. *Advanced Materials*, 25(33):4539–4543, 2013.

[52] Zhi Ern Teoh and Robert J Wood. A bioinspired approach to torque control in an insect-sized flapping-wing robot. In *Biomedical Robotics and Biomechatronics (2014 5th IEEE RAS & EMBS International Conference on*, pages 911–917. IEEE, 2014.

[53] William SN Trimmer. Microrobots and micromechanical systems. *Sensors and actuators*, 19(3):267–287, 1989.

[54] Daniel E Whitney. *Mechanical assemblies: their design, manufacture, and role in product development*, volume 22. Oxford university press New York, 2004.

[55] Daniel E Whitney, R Mantripragada, JD Adams, and SJ Rhee. Designing assemblies. *Research in Engineering Design*, 11(4):229–253, 1999.

[56] JP Whitney, PS Sreetharan, KY Ma, and RJ Wood. Pop-up book mems. *Journal of Micromechanics and Microengineering*, 21(11):115021, 2011.

[57] JP Whitney and RJ Wood. Aeromechanics of passive rotation in flapping flight. *Journal of Fluid Mechanics*, 660:197–220, 2010.

[58] JP Whitney and RJ Wood. Conceptual design of flapping-wing micro air vehicles. *Bioinspiration & biomimetics*, 7(3):036001, 2012.

[59] RJ Wood, S Avadhanula, R Sahai, E Steltz, and RS Fearing. Microrobot design using fiber reinforced composites. *Journal of Mechanical Design*, 130(5):052304, 2008.

[60] RJ Wood, E Steltz, and RS Fearing. Optimal energy density piezoelectric bending actuators. *Sensors and Actuators A: Physical*, 119(2):476–488, 2005.

[61] Robert J Wood. The first takeoff of a biologically inspired at-scale robotic insect. *Robotics, IEEE Transactions on*, 24(2):341–347, 2008.

[62] Xuan Zhang, Tao Tong, David Brooks, and G-Y Wei. Evaluating adaptive clocking for supply-noise resilience in battery-powered aerial microrobotic system-on-chip. 2014.